Towards Organic Materials Exhibiting Thermally Activated Delayed Fluorescence and Circularly Polarised Luminescence.

Author:
Beth Alexandra
LAIDLAW

Supervisor:
Dr. Thomas PENFOLD

Thesis submitted for the degree of
Doctor of Philosophy

December 2021

Declaration of Authorship

I, Beth Alexandra LAIDLAW, declare that this thesis titled, Towards Organic Materials Exhibiting Thermally Activated Delayed Fluorescence and Circularly Polarised Luminescence. and the work presented in it are my own. I confirm that:

- This work was done wholly or mainly while in candidature for a research degree at this University.
- Where any part of this thesis has previously been submitted for a degree or any other qualification at this University or any other institution, this has been clearly stated.
- Where I have consulted the published work of others, this is always clearly attributed.
- Where I have quoted from the work of others, the source is always given. With the exception of such quotations, this thesis is entirely my own work.
- I have acknowledged all main sources of help.
- Where the thesis is based on work done by myself jointly with others, I have made clear exactly what was done by others and what I have contributed myself.

Signed: Beth Alexandra Laidlaw

Date: November 21, 2022

Abstract

Doctor of Philosophy

Towards Organic Materials Exhibiting Thermally Activated Delayed Fluorescence and Circularly Polarised Luminescence.

by Beth Alexandra LAIDLAW

Organic light emitting diodes (OLEDs) have come to the fore as the state-of-the-art technology for displays and lighting. Indeed, they are now standard for most recent smartphone designs. However, despite their success, advancements are still required to improve energy efficiency and sustainability, especially with the onset of 5G which has increased power consumption.

This thesis studied two mechanisms to improve OLED efficiency. The first seeks to improve the internal quantum efficiency (IQE) of the emissive materials used within the OLED device by making non-emissive triplet states emit light. Statistically, only 25% of excitons formed by electrical excitation within the emissive material are singlets and can radiatively relax via fluorescence. The remaining 75% are triplet excitons which do not emit in conventional fluorescent materials and therefore, their energy is lost to heat. Recently, thermally activated delayed fluorescence (TADF) has emerged as a powerful approach to harvest these non-emissive triplet states. Importantly, previous work has demonstrated the importance of specific vibrational degrees of freedom to optimise the TADF process. This work examines how rotaxanes can be used to control vibrational modes of TADF molecules and therefore, fine-tune their properties and thus more efficiently re-engage the 'lost' triplet states.

In many of cases in organic electronics, due to the size of the molecules of interest, the excited state properties are described using time-dependent density functional theory (TDDFT) which provides the required balance between computational efficiency and accuracy. However, TADF materials display charge transfer (CT) characteristics, a property which is poorly described by standard approximations of the exchange correlation functional in TDDFT. Herein, we apply two tuning approaches to improve the description of excited states within TDDFT, with a particular focus upon the accuracy of excited state energies and chiroptical response. The latter being connected to the second way of improving the OLED efficiency.

Indeed, OLED display technologies require anti-glare filters to improve viewing contrast when routinely used under conditions of high ambient light. Anti-glare filters use a double layer of linear polarisers and quarter wave plates to ensure that any ambient light which enters the device is not reflected off the cathode, back towards the viewer. However, this also absorbs

$\sim$50% of the light generated by the OLED, meaning higher driving voltages are required to achieve the set brightness levels. This increases power consumption and decreases device operation lifetimes. Circularly polarised luminescence (CPL) is not absorbed by these filters, thus the integration of CPL could increase the energy efficiency of an OLED display. This work explores two mechanisms for generating CPL, firstly using small molecules and secondly with large polymer systems, which have been shown to exhibit large dissymmetry.

Acknowledgements

I would like to thank my supervisor, Dr. Thomas Penfold for his support, guidance and patience throughout this project. Without his mentorship and enthusiasm for research I would never have started this project. It was a privilege to work in the Penfold Group and see it grow throughout my time at the University. A special thanks must be given to Dr. Julien Eng and Dr. Tom Pope, their support and knowledge was unfaltering, it was a pleasure to work with you. I would also like to thank my collaborators, The Fuchter Group at Imperial College London, The Zysman-Colman Group at The University of St. Andrews, and the Goldup Group at The University of Southampton. Lastly, I would like to thank my friends and family for their continued support throughout my time at Newcastle University. There is no denying the support that my family has provided throughout this journey, without them I am sure that I would never have finished this project. Mum, Dad and Ross, thank you for your unwavering support, cheer-leading, and advice from the very beginning of my academic journey, even if *"this is just a paper filled with Wi-Fi passwords"*. Grandma and Papa, thank you for always wholeheartedly believing in me. Lauren, thank you for never doubting me and keeping me sane in the office. There is no way I could have stuck this out without your positivity. Finally, thank you to my partner Thomas, thank you for putting up with me for the last four years; I could not have done this without your support!

Contents

Declaration of Authorship iii

Abstract v

Acknowledgements vii

1 Introduction 1
- 1.1 Excited State Processes . . . 2
- 1.2 Impact of Chirality on Excited State Processes . . . 3
- 1.3 Organic Light Emitting Diodes (OLEDs) . . . 5
- 1.4 Thesis Outline . . . 9

2 Thermally Activated Delayed Fluorescence (TADF) 11
- 2.1 Background . . . 11
- 2.2 The Mechanism of TADF . . . 12
- 2.3 Kinetic Equations . . . 12
  - 2.3.1 Spin-vibronic mechanism . . . 14
- 2.4 Designing TADF molecules . . . 15

3 Circularly Polarised Light (CPL) 19
- 3.1 Background . . . 19
- 3.2 Theory . . . 20
- 3.3 Exciton Chirality Model . . . 22

4 Theory and Methodology 25
- 4.1 The Schrödinger Equation . . . 25
- 4.2 Methodology . . . 27
  - 4.2.1 Hartree-Fock Method . . . 27
  - 4.2.2 Density Functional Theory . . . 29
    - The First Hohenberg-Kohn Theorem . . . 30
    - The Second Hohenberg-Kohn Theorem . . . 30
    - Kohn-Sham DFT . . . 31
  - 4.2.3 Exchange and Correlation Functionals . . . 32
    - The Local Density Approximation . . . 32
    - Generalised-Gradient Approximation . . . 33
    - Hybrid Functionals . . . 33
    - Long-range corrected DFT . . . 34
  - 4.2.4 Basis Sets . . . 35

4.2.5 Time-Dependent Density Functional Theory 36
The Runge-Gross Theorem 36
Time-dependent Kohn-Sham equations 37
Linear-Response Time-Dependent Density Functional Theory 38
Molecular Dynamics 39
4.2.6 Polarizable Continuum Model 41

5 Refining the Performance of TADF using Rotaxanes **43**
5.1 Introduction 43
5.2 Computational Details 45
5.3 Results 45
5.3.1 Ground State Properties and Frontier Orbitals. 45
5.3.2 Photophysical Properties 46
5.3.3 Molecular Dynamics 49
5.3.4 Conclusions 52

6 Improving TDDFT for TADF using Tuned Range Separated Hybrid Functionals **53**
6.1 Introduction 53
6.2 Theory 56
6.2.1 Optimal Tuning Approach 56
6.2.2 Triplet Tuning Approach 57
6.3 Computational Details 58
6.4 Results 59
6.4.1 The Influence of Geometry on Tuned-Range Separated Functionals 59
PTZ-DBTO$_2$ 59
TAT-3DBTO$_2$ 63
6.4.2 Assessing Chiral Perturbation for achieving CP-TADF Emitters 67
Excited State Properties and CPL at Critical Points . . . 67
Assessing the Potential for Axially Chiral TADF Emitters 73
6.5 Conclusions 77

7 CPL beyond a Single Molecule **79**
7.1 Introduction 79
7.2 Computational Details 80
7.3 Theory 81
7.4 Results 83
7.4.1 Single Polymer Chains 83
7.4.2 Interchain Coupling of Dimers 88
7.5 Conclusions 92

8 Conclusion **95**
8.1 Conclusion and Future Work 95

List of Figures

1.1 A Jabalonski Diagram for photoexcitation (Exc). Featuring the ground state (GS), first singlet excited state (S_1), first triplet excited state (T_1), and second triplet excited state (T_2), each with vibrational states. The pathways of the excited state dynamics are denotes as, fluoresence (F), phosphorescence (P), non-radiative decay (NR), inter-system crossing (ISC), reverse inter-system crossing (rISC), internal conversion (IC) and reverse internal conversion (rIC). 3

1.2 A potential energy curve (PEC). The ground state (GS) is shown in blue, S_1 in purple and T_1 in pink. There is a PEC for each electronic state, with the energy of each state (E shown on the y-axis) changes with nuclear co-ordinate (R on the x-axis. The blue arrow, labelled Exc., represents the excitation from the GS to the S_1, and the purple arrow, labelled F, represents fluorescence. ISC or rISC is possible where the S_1 and T_1 states cross. The GS in this case has two minima, thus the molecule is likely to show two stable geometric configurations. 4

1.3 A simplified diagram of an OLED with a focus on the TADF mechanism. The cathode introduces electrons to the electron injection layer. The cathode introduces electron-holes to the hole injection layer. The electrons and holes meet in the emissive layer, where the luminescent molecules are. TADF can occur in the emitter. Figure adapted from [1]. 6

1.4 Jablonski Diagram for the photophysical processes of first generation OLEDs. The navy line between the S_1 and T_1 represents the electron-hole recombination that populates the S_1 and T_1, with a probability of 25% and 75% respectively. The GS is shown in black, S_1 in purple and T_1 in pink. The pathways of the excited state dynamics are shown as prompt fluorescence (PF), and non-radiative decay (NR), in purple and orange, respectively. 7

1.5 Jablonski diagram for the photophysical processes of TADF OLEDs. The navy line between the S_1 and T_1 represents the electron-hole recombination that populates the S_1 and T_1, with a probability of 25% and 75% respectively. The GS is shown in black, S_1 in purple and T_1 in pink. The pathways of the excited state dynamics are shown as prompt fluorescence (PF), delayed fluorescence (DF), and reverse inter-system crossing, in purple, navy and green, respectively. 8

2.1 The emission process of photo-generated excitons for fluorescence (1 - 2 - 5), phosphorescence (1 - 2 - 3 - 6) and thermally activated delayed fluorescence (1 - 2 - 3 - 4 - 5). Adapted from [2]. 13

2.2 The influence of position of substitution of electron donor (D) and electron acceptor (A) units on the TADF of the system.[3] From [4]. 16

2.3 The quasi-equatorial and quasi-axial conformers of 3, 7-PTZ-DBTO2, (a) and (d) respectively. (b) and (f) are the structures of the HOMO, (c) and (e) are the structures of the LUMO. Adapted from [5]. 17

3.1 A scheme to illustrate circularly polarised light. It is made up of two plane polarised waves with equal amplitudes (navy blue and purple) that are at right angles to each other, with a quadrature phase relationship. The helical trace is shown in pink, as the resultant electric field vector is of constant magnitude and continues to rotate at a constant rate. 20

4.1 Schematic representation of time-dependent density functional theory. 36

5.1 Structures of the molecules, dTlCzBP, [2]-rotaxane, and [3]-rotaxane, investigated in this work. The emitters will be known as **1**, **1**⊂**2** and **1**⊂$\mathbf{2}_2$ for the dTlCzBP system, [2]rotaxane, and [3]rotaxane, respectively. 44

5.2 The LUMO (top) and HOMO (bottom) orbitals for **1**, **1**⊂**2** and **1**⊂$\mathbf{2}_2$ at the ground state geometry, computed using DFT(PBE0)/Def2SVP.[6] 47

5.3 a) Absorption and b) PL spectra of **1**, **1**⊂**2** and **1**⊂$\mathbf{2}_2$ in PhMe (λ_{exc}=340 nm, 10^5M) as calculated by Rajamalli *et al.*[6] 48

5.4 Solid state structure of **1**⊂**2** with hydrogen contacts shown in yellow. Structure obtained by diffraction by Rajamalli *et al.* [6] 49

5.5 The distribution of the D-A bond distance, the dihedral angle between the D and A groups and carbozole triazine aryl-aryl bond for (a-c) **1**, (d-f) **1**⊂**2** and (g-i) **1**⊂$\mathbf{2}_2$ for the ground (red) and excited state (blue, purple) geometries. 50

5.6 Ground state potential energy scans for **1** (left), **1**⊂**2** (middle), and **1**⊂$\mathbf{2}_2$(*right*). 51

6.1 Schematic representation of the two systems studied. Left; PTZ-$DBTO_2$ and right: TAT-3$DBTO_2$.[7] 54
6.2 The CP-TADF emitters **A, B, C, D** and **E** investigated in this work. 55
6.3 The HOMO (left) and LUMO (right) for the three geometries of PTZ-DBTO2 studied.[7] 60
6.4 Evolution of J^2_{OT} (a) and J^2_{TT} (b) as a function of the range separation parameter ω for the equatorial (red), axial (blue) and S_1^{Min} (green) structures of PTZ-$DBTO_2$.[8] 60
6.5 Evolution of J^2_{OT} (a) and J^2_{TT} (b) as a function of the range separation parameter ω for the FC (red) and S_1^{Min} (blue) structures of TAT-3$DBTO_2$.[8] 63
6.6 The linear reaction pathway between the FC geometry and S_1^{MIN} (calculated at PBE0 level) of TAT-3$DBTO_2$ using the (a) ω=0.000 a_0^{-1} (b) ω=0.118 a_0^{-1} and (c) ω=0.131 a_0^{-1}. The solid blue lines are singlet states and the Dash lines are triplet states. All energies are plotted relative to the ground state energy at the FC geometry.[8] 64
6.7 Location of the frontier orbitals for Emitter **6** in the OT, S_0 geometry study. Top shows the orbitals involved in a $^3LE_{Deloc}$ transition. Bottom shows the orbitals involved in a ^3LE_C transition. 68
6.8 The HOMO (right) and LUMO (left) orbitals for Emitter **A**. Top B3LYP S_1 geometry, Bottom OT S_1 geometry. 73
6.9 The HOMO (right) and LUMO (left) orbitals for emitter **E**. For the B3LYP approach (top) and the OT approach (bottom). . . 74
6.10 Distribution of g-factors from MD sampling of emitter **E** for the B3LYP study (top) and OT study (bottom). The geometries in the S_0 is shown in blue and the geometries in the S_1 state are shown in red. 76

7.1 Structures of the simplified models of (a) F8BT and (b) PFO. R are C_8H_{17} side chains, however herein, R represents methyl groups. n represents the number of repeat units and the arrows indicate the twist angle (θ) between adjacent repeat units.[9] 81
7.2 Energy of the S_1 state (in eV) for PFO (red) and F8BT (black) as a function of the number of repeat units.[9] 83

7.3 (a) g-factor of the S_1 state as a function of the number of monomer units (n) for PFO (red) and F8BT (black) oligomers. A fixed twist angle (θ=40°) was used throughout. (b) g-factor as a function of θ for PFO (red) and F8BT (black) 2-mers (n=2). The dashed line between the points are a guide for the eye. (c) The ratio between the electric and magnetic transition dipole moments, μ^2/m^2 for PFO (red) and F8BT (black) as a function of the number of repeat units. [9] 86
7.4 (a) The ratio between the electric and magnetic transition dipole moments, μ^2/m^2 for PFO (red) and F8BT (black) as a function of the twist angle between the monomer units. (b) cos(τ), where τ is the angle between the electric and magnetic dipole moments, as a function of the twist angle between each monomer units for PFO (red) and F8BT (black).[9] 87
7.5 (a) Schematic of two polymer chains and the coordinates (d and ϕ) manipulated in Figure 7.6. (b) Density difference of the lowest exciton of a F8BT dimer model illustrating the electron density delocalised over the two chains. (c) Schematic of the effect of interacting polymer chains on the electric and magnetic transition dipole moments.[9] 88
7.6 a) g-factor as a function of the distance between the centre-of-mass of each chain in a dimer of PFO (red) and F8BT (black) 2-mers (n=2, θ=40°). The angle between the two polymer chains in the dimer (ϕ) was fixed at 2°. The dashed line is a fit using d^{-3} illustrating a decay in the dissymmetry consistent with a reduction in the exciton coupling. (b) g-factor as a function of the angle (ϕ) between the two polymer chains (n=2, θ=40°) in the dimer. The distance between the 2-mers was fixed at 6 Å.[9] 90
7.7 $\Delta\epsilon$ for the lowest exciton couplet of the F8BT model as a function of the (a) distance (d, n=2, θ=40° and ϕ=10°) and (b) angle (ϕ, d=6 Å, n=2, θ=40°) between the monomer chains. Spectra broadened using Gaussian function 0.25 eV FWHM.[9] 91
7.8 $\Delta\epsilon$ for the lowest exciton couplet of the PFO model as a function of the (a) distance (d, n=2, θ=40° and ϕ=10°) and (b) angle (ϕ, d=6 Å, n=2, θ=40°) between the monomer chains. Spectra broadened using Gaussian function 0.25 eV FWHM.[9] 91
7.9 g-factor of the S_1 state as a function of the number of monomer units (n) for a dimer of PFO (black). d=7 Å, θ=40° and ϕ=2°. Reproduced with permission from Royal Society of Chemistry.[9] 93

List of Tables

5.1 Electronic properties of axle **1**, **1**⊂**2** and **1**⊂**2**$_2$ at the ground state geometry, calculated using DFT(PBE0)/Def2-SVP. 46
5.2 Electronic properties of axle **1**, **1**⊂**2** and **1**⊂**2**$_2$ determined by Rajamalli *et al.*.[6] 46
5.3 Calculated electronic properties of axle **1**, **1**⊂**2** and **1**⊂**2**$_2$ at the excited state (S_1) geometry. 47

6.1 Electronic structure of PTZ-DBTO$_2$ at all three studied geometries and at the optimal values of $\omega = 0a_0^{-1}$, $\omega = \omega^*_{OT}$ and $\omega = \omega^*_{TT}$. 62
6.2 Electronic structure of TAT-3DBTO$_2$ at the minima of the ground state and ^{1}CT and at the $\omega = 0.0a_0^{-1}$. 65
6.3 Electronic structure of TAT-3DBTO$_2$ at the minima of the ground state and ^{1}CT and at the optimal value of $\omega = \omega^*_{OT}$. 66
6.4 Electronic structure of TAT-3DBTO$_2$ at the minima of the ground state and ^{1}CT and at the optimal value of $\omega = \omega^*_{TT}$. 66
6.5 Energies and g-factors of the two studies, DFT(B3LYP) (left) and OT(LC-BLYP) (right), on the emitter **A**, for the optimised S_0, S_1 and T_1 geometries. 69
6.6 Energies and g-factors of the two studies, DFT(B3LYP) (left) and OT(LC-BLYP) (right), on the emitter **B**, for the optimised S_0, S_1 and T_1 geometries. 70
6.7 Energies and g-factors of the two studies, DFT(B3LYP) (left) and OT(LC-BLYP) (right), on the emitter **C**, for the optimised S_0, S_1 and T_1 geometries. 71
6.8 Energies and g-factors of the two studies, DFT(B3LYP) (left) and OT(LC-BLYP) (right), on the emitter **D**, for the optimised S_0, S_1 and T_1 geometries. 72
6.9 Energies and g-factors from the two studies, B3LYP (left) and OT (right), for emitter **E**, for the optimised S_0, S_1 and T_1 geometries. 75

7.1 The electric and the magnetic transition dipole moments for PFO and F8BT as a function of the number of repeat units (n). Atomic units are used throughout. A fixed twist angle (θ=40°) was used throughout. 84

7.2 The electric and the magnetic transition dipole moments for PFO and F8BT 2-mers (n=2) as a function of the twist angle between the monomer units. 85
7.3 The coupling potential between the excitonic states (V) in eV for PFO and F8BT as a function of the angle (ϕ) between the monomer chains. 92
7.4 The coupling potential between the excitonic states (V) in eV for PFO and F8BT as a function of the distance (d) between the monomer chains. 92

List of Abbreviations

A	**A**cceptor
CD	**C**ircularly **D**ichromism
CP-OLED	**C**ircularly **P**olarised **O**rganic **L**ight **E**mitting **D**iode
CP	**C**ircularly **P**olarised
CT	**C**harge **T**ransfer
D	**D**onor
DF	**D**elayed **F**luorescence
DFT	**D**ensity **F**unctional **T**heory
ECD	**E**lectronic **C**ircular **D**ichromism
ECM	**E**xciton **C**hirality **M**odel
EQE	**E**xternal **Q**uantum **E**fficiency
$\mathbf{g}_{abs}$	Absorptive Dissymmetry Factor
$\mathbf{g}_{lum}$	Luminescence Dissymmetry Factor
GGA	**G**eneralised **G**radient **A**pproximation
HF	**H**artree-**F**ock
HOMO	**H**ighest **O**ccupied **M**olecular **O**rbital
IC	**I**nternal **C**onversion
IQE	**I**nternal **Q**uantum **E**fficiency
ISC	**I**nter-**S**ystem **C**rossing
IVR	**I**ntramolecular **V**ibrational **R**edistribution
LCD	**L**iquid **C**rystal **D**isplay
LDA	**L**ocal **D**ensity **A**pproximation
LE	**L**ocal **E**xcitation
LED	**L**ight **E**mitting **D**iode
LEP	**L**ight-**E**mitting **P**olymer
LH	**L**eft-**H**andedness
LR-TDDFT	**L**inear-**R**esponse **T**ime-**D**ependent **D**ensity **F**unctional **T**heory
LUMO	**L**owest **U**noccupied **M**olecular **O**rbital
MD	**M**olecular **D**ynamics
OLED	**O**rganic **L**ight **E**mitting **D**iode
ORD	**O**ptical **R**otatory **D**ispersion
OT	**O**ptimal **T**uning
PEC	**P**otential **E**nergy **C**urve
PF	**P**rompt **F**luorescence
QD	**Q**uantum **D**ynamics
RH	**R**ight-**H**andedness
rISC	**r**everse **I**nter-**S**ystem **C**rossing
ROA	**R**aman **O**ptical **A**ctivity

S$_N$	**N**th **S**inglet Excited State
SOC	**S**pin **O**rbit **C**oupling
T$_N$	**N**th **T**riplet Excited State
TADF	**T**hermally **A**ctivated **D**elayed **F**luorescence
TDA	**T**amm-**D**ancoff **A**pproximation
TDDFT	**T**ime-**D**ependent **D**ensity **F**unctional **T**heory
TDSE	**T**ime **D**ependent **S**chrödinger **E**quation
TISE	**T**ime **I**ndependent **S**chrödinger **E**quation
TTA	**T**riplet **T**riplet **A**nnihilation
uDFT	**u**nrestricted **D**ensity **F**unctional **T**heory
uDFT	**r**estricted **D**ensity **F**unctional **T**heory
VCD	**V**ibronic **C**ircular **D**ichromism
^{1}**CT**	Singlet **C**harge **T**ransfer Excited State
^{1}**LE**	Singlet **L**ocal **E**xcitation
^{3}**CT**	Triplet **C**harge **T**ransfer Excited State
^{3}**LE**	Triplet **L**ocal **E**xcitation

List of Publications

- Nobuyasu, R.S., Ward, J.S., Gibson, J., Laidlaw, B.A., Ren, Z., Data, P., Batsanov, A.S., Penfold, T.J., Bryce, M.R. and Dias, F.B., The influence of molecular geometry on the efficiency of thermally activated delayed fluorescence. *Journal of Materials Chemistry C*, 7(22):6672-6684, 2019.

- Wan, L., Wade, J., Salerno, F., Arteaga, O., Laidlaw, B., Wang, X., Penfold, T., Fuchter, M.J. and Campbell, A.J., Inverting the handedness of circularly polarized luminescence from light-emitting polymers using film thickness. *ACS nano*, 13(7):8099-8105, 2019.

- Eng, J., Laidlaw, B.A. and Penfold, T.J., On the geometry dependence of tuned-range separated hybrid functionals. *Journal of computational chemistry*, 40(25):2191-2199, 2019.

- Rajamalli, P., Rizzi, F., Li, W., Jinks, M.A., Gupta, A.K., Laidlaw, B.A., Samuel, I.D., Penfold, T.J., Goldup, S.M. and Zysman-Colman, E., Using the mechanical bond to tune the performance of a thermally activated delayed fluorescence emitter. *Angewandte Chemie International Edition*, 60(21):12066-12073, 2021.

- Laidlaw, B., Eng, J., Wade, J., Shi, X., Salerno, F., Fuchter, M.J. and Penfold, T.J., On the factors influencing the chiroptical response of conjugated polymer thin films. *Chemical Communications*, 57(77):9914-9917, 2021.

For Papa

Chapter 1

Introduction

Organic molecules, made up primarily of carbon and hydrogen, are fundamental to all life. They are abundantly available, with the number of potential organic drug-like molecules estimated to be between 10^{23}-10^{60}. [10] They are crucial to nearly every area of research and more recently have become a focus in the organic electronics technology sector as they offer the opportunity to develop cheap and efficient electronic displays. When developing organic molecules for displays, it is essential to understand how light interacts with the molecules. Indeed, in many technologies molecules function primarily in their electronic ground state, however for display technologies, molecules must exist in their electronically excited state and therefore display desirable properties in these states. It is the application of these properties to display technologies that is the focus of this thesis.

Display and lighting technology has become a mainstay of everyday life, with the introduction of smartphones, almost every adult in the western world has access to a screen 24 hours a day. Due to the Covid-19 pandemic a large percentage of the global population were forced to work from home, with their only interaction being through a screen on their smartphone, laptops, desktops or televisions. Thus, the technology industry is continually motivated to improve the viewing quality and efficiency of devices to remain competitive in a saturated market. Recently, organic light emitting diodes (OLEDs) have been integrated into devices to provide better brighter colours, flexible screens, and lower power consumption compared to standard liquid crystal displays (LCD).[11] As the name suggests, OLEDs are built primarily using organic molecules that are electronically excited and in turn, emit light.

OLED integration into display technologies has been a proven success, with the introduction of OLED televisions and OLED smartphone screens.[11] However, as with any emerging technology the focus of research now is to improve the efficiency. In this area, understanding and controlling the inherent abilities of the molecular components can be exploited to develop new and desirable characteristics within OLEDs. The main limitations of current OLED technology is the internal quantum efficiency (IQE), the need for polarisers to be integrated into devices and the outcoupling of the devices. Thermally activated delayed fluorescence (TADF) has been reported to produce internal quantum efficiencies (IQE) of nearly 100%,[12, 13, 14] therefore showing that TADF provides an important mechanism to improve display

and lighting technology.[15] However, even in these cases the external quantum efficiencies (EQE) of OLED devices remain relatively low, between 20-25%.[16] Thus, improving this EQE is a focus of much research. Within the architecture of OLEDs there is an anti-glare filter that not only increases the bulk of the device but also reduces the device's efficiency as much of the light emitted from the active layer of the device is absorbed. One way to remove the need for these anti-glare filters is to design an emitter that outputs chiral light. Chirality is a fundamental property of some molecules. It plays an important role in many areas of research, such as drug discovery[17], catalysis[18] and magnetic-based technologies[19]. More recently, its application to optoelectronics, such as OLED technology and photodetectors, has been of significant interest. Within OLED technology circularly polarised light is generated from chiral emitters,[20] this improves the efficiency of devices by reducing the light absorbed by the anti-glare filters that are used to improve viewing contrast. All of these aspects highlight the importance of understanding the excited state.

1.1 Excited State Processes

Photoexcitation is a crucial process when considering the excited state properties of a molecule. After an excited state is generated, the molecule exists in a highly non-equilibrium state and consequently there are a number of different processes that can occur. It can undergo radiative decay processes, fluorescence and phosphorescence, or non-radiative processes, such as internal conversion (IC), inter-system crossing (ISC) and intramolecular vibrational redistribution (IVR). All of these processes are in constant competition with each other, and some of the processes are more favourable than others when it comes to applications in electronic devices. Jabalonski diagrams (Figure 1.1) are often used to pictorially describe these transitions. The Y axis denotes the energy of the excited states, however, the X axis has no physical meaning, it is used to separate the different states. The excited states are shown as thick horizontal lines, with thinner lines above representing the different vibrational states. The radiative mechanisms can be seen as wavy vertical arrows and the non-radiative systems are dotted horizontal arrows. The Jabalonski diagram however, only shows a static picture of a molecule at fixed nuclear geometry, and does not fully describe the dynamic processes that occur in reality.

Another way to represent the excited states of a molecule is with a potential energy curve (PEC), Figure 1.2, contrary to the Jabalonski diagrams, the X-axis on the PEC represents nuclear displacements. These displacements could be the change of a normal mode, dihedral angle or the main reaction path. The increased detail of the PEC provides a good description of how the energy levels depend on the molecular geometry, shedding insight into likely excited state processes. However, it still fails to provide a multidimensional description that is vital for a good understanding of the excited state

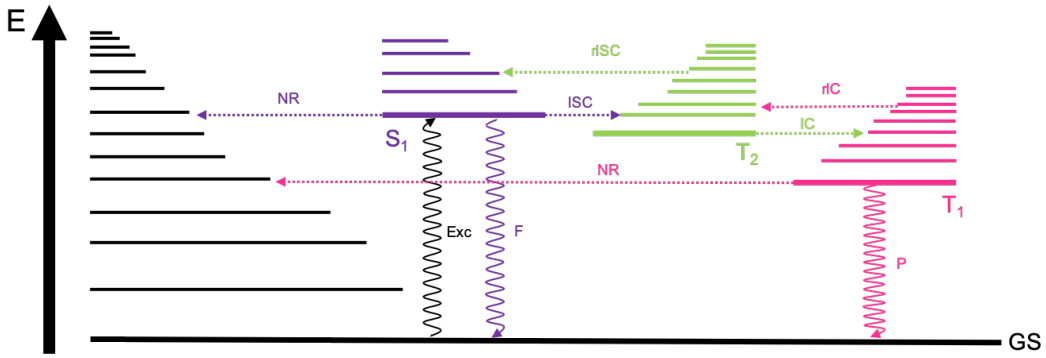

FIGURE 1.1: A Jabalonski Diagram for photoexcitation (Exc). Featuring the ground state (GS), first singlet excited state (S_1), first triplet excited state (T_1), and second triplet excited state (T_2), each with vibrational states. The pathways of the excited state dynamics are denotes as, fluoresence (F), phosphorescence (P), non-radiative decay (NR), inter-system crossing (ISC), reverse inter-system crossing (rISC), internal conversion (IC) and reverse internal conversion (rIC).

processes of a system. The PEC also fails to accurately describe the degrees of freedom and coupling between the degrees of freedom and the excited states.

The molecular nuclei evolves within a multidimensional (3N-6) potential energy surface (PES). The PES can be generated by calculating the electronic energy at considered fixed nuclei position. The PES does not depend on the absolute location of atoms within the molecule, just their relative location compared to one another. This (3N-6) PES is inherently difficult to pictorially describe, and so it is common to use the reaction coordinate as a description. This simplification commonly works, however becomes less appropriate when there is more than one variable. Ultimately, a complete description of excited state processes in a molecule requires the time-dependent Schrödinger equation (TDSE). This approach, known as quantum dynamics (QD), models a system using first principles and is a powerful way of describing the dynamics of a system. The TDSE was used by Gibson *et al.* to describe how the vibronic coupling of locally excited states facilitates efficient rISC within the TADF mechanism.[2] However, throughout this work, the systems investigated are beyond the scope of QD due to their size.

1.2 Impact of Chirality on Excited State Processes

Chirality exists in nature on many scales. Any object or system that can exist in two forms that are non-superimposable mirror image can be considered chiral, a well-known example is the right and left human hands. On the molecular scale the same description is used, and the two objects, that are non-superimposable mirror images of each other, are called enantiomers.

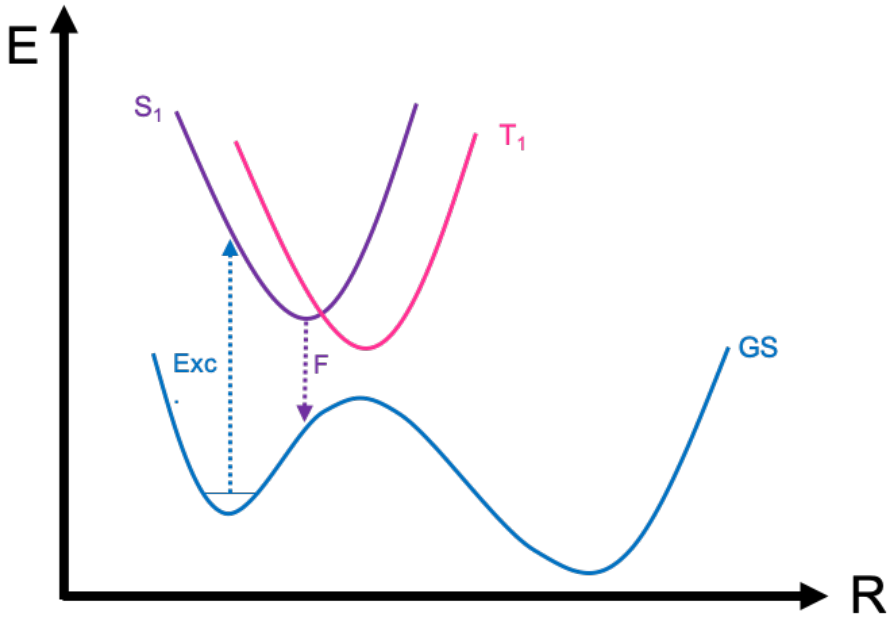

FIGURE 1.2: A potential energy curve (PEC). The ground state (GS) is shown in blue, S_1 in purple and T_1 in pink. There is a PEC for each electronic state, with the energy of each state (E shown on the y-axis) changes with nuclear co-ordinate (R on the x-axis. The blue arrow, labelled Exc., represents the excitation from the GS to the S_1, and the purple arrow, labelled F, represents fluorescence. ISC or rISC is possible where the S_1 and T_1 states cross. The GS in this case has two minima, thus the molecule is likely to show two stable geometric configurations.

Light can also be chiral, circularly polarised (CP) light can be described as two plane polarised waves of equal amplitude at right angles to one another, with a quadrature phase relationship. Resulting in an electric field vector of constant magnitude and fixed rotation, the resultant wave traces a helix through space. This helix can trace in one of two directions: it can either trace in the right-handed (RH) or left-handed (LH) direction.

Harnessing the properties of CP light in research is not a novel area of research, J. H. Van't Hoff suggested that CP light could be used in asymmetric synthesis to selectively produce an enantioenriched substance in the 19^{th} century.[21] However, CP photochemistry has not become a mainstream technique in asymmetric synthesis, notwithstanding some elegant studies that vary the photon energy and wavelength approaches.[22, 23] This is because the enantioselectivity is mostly decided by the ECD of a substance.[24] The g-factor, or dissymmetry, is used to describe this selectivity. The g-factor can be described as follows:

$$g = 2\frac{I_L - I_R}{I_L + I_R} \tag{1.1}$$

Where R and L refer to the handedness of the light and I can be the intensity of photoluminescence or electroluminescence. If there is total selectivity of CP light then $|g|$=2, however, it is commonplace for the g-factor to be very low for electronic transitions important for organic photochemistry, usually in the $<10^{-2}$ regime.[25] Futhermore, it is expected that this low selectivity in the absorption of CP light results in low stereoselectivity in the resultant photochemistry.[24]

When a chiral system is excited the two enantiomers are excited. The excitation process within both enantiomers is the same, however, each enantiomer will emit either RH or LH polarised light. Thus, understanding the difference in the emission from each enantiomer is paramount to appropriate modelling of chiral systems. The exciton chirality model uses the electronic transition dipole moments to describe the behaviour after photoexcitation, however, when chiral molecules are being considered the rotatory strength becomes non-zero. When this is the case, it is important to include the magnetic transition dipole moments in the description of the resultant emission.

1.3 Organic Light Emitting Diodes (OLEDs)

OLEDs have undergone rapid development since the work of Tang and Van Slyke in 1987, to become cemented into mainstream display and lighting technology.[26] OLEDs have many promising features for display technology such as their lower power consumption and improved image quality, not to mention their potential for ultra-thin, flexible or transparent screens, previously properties only associated with science-fiction.[1] OLEDs are comprised of flexible thin films or small organic molecules, in comparison to traditional light-emitting diodes (LEDs) which are made up of rigid silicon crystals doped with inorganic semiconducting materials. Those inorganic dopants can have more valence electrons than silicon, such as phosphorous, thus creating an n-type semiconductor or fewer valence electrons than silicon, like boron, creating a p-type semiconductor. An interface is created at the junction of these two semiconductors known as a p-n junction, at which point LEDs produce light. Within the LED there is a conduction band containing the n-type material which transfers electrons, upon electronic current being passed through the LED, to the p-type material where they recombine with holes in the valence band. When the electron and hole recombines a photon is generated, and thus the device will emit light. In this case, the conduction band and the valence band can be considered the solid state equivalences of the highest occupied molecular orbital (HOMO) and lowest unoccupied molecular orbital (LUMO), respectively. Comparatively, OLEDs operate through similar principles, with the solid crystals being replaced by flexible organic materials. Within an OLED the organic materials are integrated into an ultrathin film, of thicknesses 100nm, that undergo luminescence and electroexcitation, as described previously. The basic set up of an OLED can be seen in Figure 1.3.

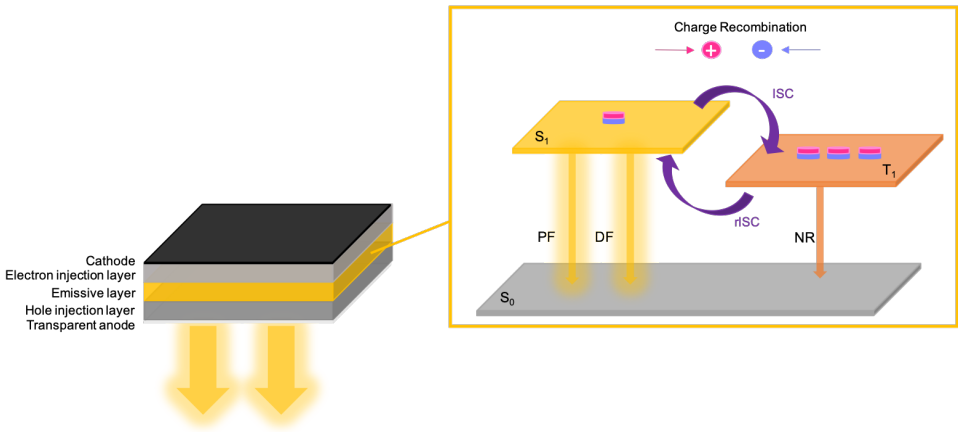

FIGURE 1.3: A simplified diagram of an OLED with a focus on the TADF mechanism. The cathode introduces electrons to the electron injection layer. The cathode introduces electron-holes to the hole injection layer. The electrons and holes meet in the emissive layer, where the luminescent molecules are. TADF can occur in the emitter. Figure adapted from [1].

When considering OLED devices, there are two metrics that are commonly used to describe the performance of the devices: internal quantum efficiency (IQE) and external quantum efficiency (EQE). IQE is a measure of how many photons the emissive molecule radiates. This is influenced by internal processes, such as intersystem crossing and can be reduced by non-radiative decay. EQE is the efficiency of the molecules environment, thus accounts for the influence of the emissive molecules embedded environment. After the photons have been emitted, the environment of the device can effect how much light is produced. Environmental factors include the orientation of the embedded emitter and photon absorption from other materials in the device. Therefore, devices may possess 100% IQE (η_{IQE}) but typically have a EQE (η_{EQE}) of around 0.2.

$$\eta_{EQE} = \eta_{out}\eta_{IQE}, \quad \eta_{IQE} = \gamma\Phi_{PL/EL} \tag{1.2}$$

Equation 1.2 shows γ which is the charge recombination factor. It is equal to one with perfect recombination and zero with no recombination, whilst ϕ is the quantum yield of luminescence.[27] When generating the photons within an OLED, there is an intrinsic limit on the electrical excitation process due to spin statistics; 25% of the molecules are generated in the singlet state and 75% in the triplet (dark) state. Therefore, the quantum yield depends on the ability to produce light from both excited states.

$$\Phi = 0.25\Phi_S + 0.75\Phi_T \tag{1.3}$$

The triplet state emits via non-radiative pathways in typical organic molecules, this is due to weak dipole coupling between the triplet states and the ground

state. Thus, typical organic molecules will only emit radiatively from the single states and therefore will have an inherent IQE limit of 25%. First generation OLEDs, such as those in Figure 1.4, used purely fluorescent materials, and thus had a limited efficiency.

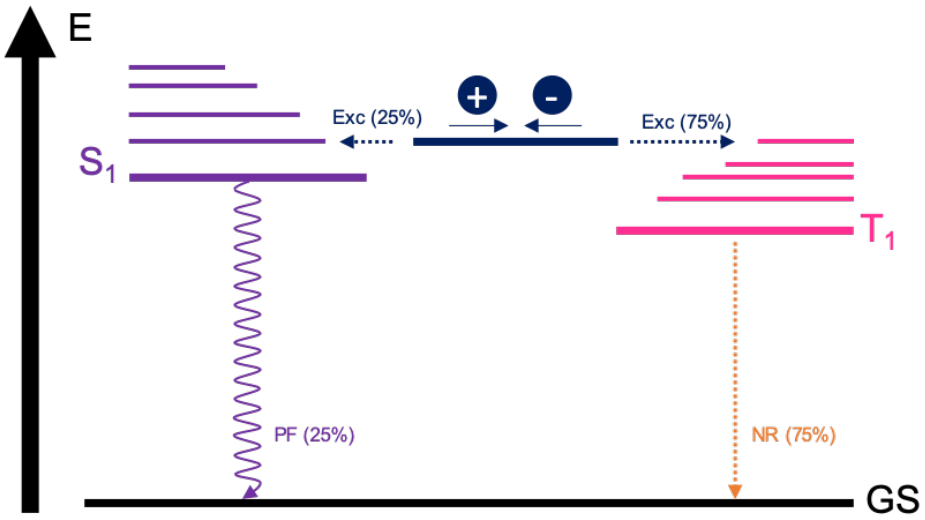

FIGURE 1.4: Jablonski Diagram for the photophysical processes of first generation OLEDs. The navy line between the S_1 and T_1 represents the electron-hole recombination that populates the S_1 and T_1, with a probability of 25% and 75% respectively. The GS is shown in black, S_1 in purple and T_1 in pink. The pathways of the excited state dynamics are shown as prompt fluorescence (PF), and non-radiative decay (NR), in purple and orange, respectively.

To improve this limitation, second generation OLEDs use heavy metals, such as iridium and platinum. The addition of these heavy metals, albeit rare and expensive ones, increases the spin-orbit coupling (SOC) which in turn mades the dark T_1 state radiative.[28] These additional pathways open the possibility for an OLED to have 100% radiative quantum efficiency by harnessing both fluorescence and phosphorescence transitions. However, the introduction of these heavy metals has a considerable impact on the cost of the devices, due to the rarity of the elements integrated. Indium is one of the rare heavy metals that is used in OLED devices, in fact displays on smartphones and tablets account for 80% of indium consumption, with the vast majority ending up in landfill due to poor recycling.[29, 30]

An alternative approach to overcoming the inherent limit of IQE, but retain purely fluorescent materials is by using P-type delayed fluorescence. The mechanism of P-type delayed fluorescence is now known as triplet-triplet annihilation (TTA), but was initially named after the emission displayed, in the first instance, by Pyrene.[31, 32]. Here, two triplet states can fuse together

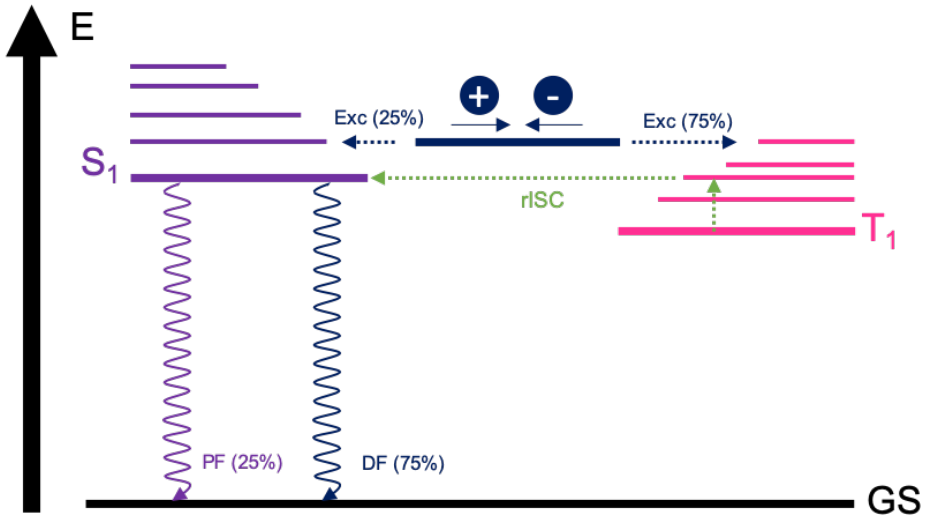

FIGURE 1.5: Jablonski diagram for the photophysical processes of TADF OLEDs. The navy line between the S_1 and T_1 represents the electron-hole recombination that populates the S_1 and T_1, with a probability of 25% and 75% respectively. The GS is shown in black, S_1 in purple and T_1 in pink. The pathways of the excited state dynamics are shown as prompt fluorescence (PF), delayed fluorescence (DF), and reverse inter-system crossing, in purple, navy and green, respectively.

to generate a single emissive singlet state. P-type OLED devices have a theoretical limit of IQE of 63.5%; due to the strict ordering of excited states by their energies and the fact that two triplet excitons per one singlet.[32] Two more mechanisms that can be exploited to optimise OLEDs and which are the focus of the present thesis are is Thermally Activated Delayed Fluorescence (TADF), that has the potential to reach 100% IQE.[33] and CP luminescence to optimise light output. These are discussed in detail in the following.

Similarly to TTA, TADF was initially named after the molecule Eosin, and was termed E-type fluorescence by Parker *et al.*.[34] The mechanism allows rapid conversion between states, it uses iso-energetic triplet and singlet states to allow triplet excitons to undergo rISC to become singlet excitons. The singlet exciton can then relax via fluorescence, known as delayed fluorescence, therefore this mechanism, as shown in Figure 1.5, can achieve 100% quantum efficiency.[5] To create iso-energetic states, the molecule must have a small singlet-triplet gap. Donor-acceptor (D-A) type molecules are commonly used to minimise this energy gap as they localise of the HOMO and LUMO on different parts of the molecule.

An emerging design for OLEDs aims to increase the EQE and reduce the size and expense of devices by integrating a 'molecular polariser'. Typically, OLED designs include an anti-glare filter to improve the viewing contrast, so

devices can be seen on a sunny day for example. However, these filters reduce the brightness output of the devices and thus requires increased power input which reduces battery life. Integrating circular polarisation into the TADF material itself is one way to remove the need for such anti-glare filters. Not only do anti-glare filters increase the bulk of the devices, they also absorb up to 50% of the light output of the device. Improving the IQE of OLEDs by enhancing the TADF properties of systems is one of the focuses of this work. The second focus is improving the EQE of OLEDs by integrating circular polarisation into the design of the emitting system. First the two individual phenomena will be investigated independently, finally the work will attempt to combine both properties.

1.4 Thesis Outline

This thesis investigates mechanisms, namely TADF and CPL, that could improve the efficiency of organic electronics such as OLEDs. Following this introduction, the first three chapters provide a description of the mechanisms of TADF, Chapter 2, CPL, Chapter 3, and the theory and methodology, Chapter 4, used to reach conclusions in the forthcoming results chapters. The following three chapters report the results of this project. Chapter 5 uses molecular architecture in rotaxane structures to fine-tune TADF properties. The mechanical bond can be utilised to gain fine control of the vibrational freedom of the bond that is critical to controlling the TADF emission. Chapter 6 establishes an efficient method to more accurately describe the excited states of TADF and CPL materials using existing TDDFT methods. TDDFT is known to give a poor description of the CT state. Such character is common in TADF emitters with a D-A architecture, thus to providing a better description of this character is crucial when designing efficient future emitters. The Chapter explores two methods, namely Koopmans Optimal Tuning and Triplet Tuning, to understand the effects of the implementation of non-local character into the calculation. This is achieved through applying the methods to known TADF emitters and CP-TADF emitters and making comparison to standard hybrid functionals. Finally, Chapter 7 presents a computational study to to establish the origin of CP luminescence from larger systems. The systems studied are chiral polymers that form a helical shape which display an exciton that can be delocalised across the system. The work studies the extent of this delocalisation and its effect on the chiroptical response. The work is extended to gain an understanding as to the effect of the excitonic coupling between neighbouring polymer chains and thus, an indication of the impact of aggregation of polymers that are formed in thin-films.

Chapter 2

Thermally Activated Delayed Fluorescence (TADF)

2.1 Background

Improving the efficiency, device structure and lifetime of OLEDs involves the exploitation of many mechanisms, one of which is thermally activated delayed fluorescence (TADF). TADF was first applied to OLEDs by Adachi in 2012. [12] By designing novel, metal-free electroluminescent molecules, Adachi *et al.* were able to improve the inherent 25% internal quantum efficiency (IQE) of purely fluorescent molecules associated with charge recombination. The inherent IQE of OLEDs is characteristic of the 1:3 singlet:triplet ratio of charge recombination, as defined by spin statistics. Therefore, reengaging the dark triplet states is imperative to improving the efficiency of OLEDs to make them viable for the mass market. Previously, heavy metals have been introduced into OLED devices to exploit spin orbit coupling (SOC), making the said dark triplet states bright by phosphorescence. Commonly metals such as iridium are used, however, these heavy metals bring with them expense and toxicity. Therefore, designing efficient metal-free OLEDs is at the forefront of the current field.

Typically fluorescent molecules emit light from the S_1 state to the S_0 state, in the nanosecond regime. However, some fluorescent materials can emit additional light in the microsecond regime; this is known as delayed fluorescence.[35] Delayed fluorescence usually arises from two mechanisms, TTA and TADF. In both cases low lying triplet states are formed. In the former, these combine to generate a higher lying singlet state which then relaxes and emitters. In the latter, TADF, thermal energy promotes the low lying triplet back to the singlet state. These two mechanisms occur on similar timescales, but can be discriminated by their dependence on temperature and laser excitation power.

The TADF phenomenon in purely organic molecules was first observed in the 1960's by Parker and Hatchard[34], they termed it "E-type" delayed fluorescence, as the first molecule that displayed this phenomenon was Eosin. The work of Berberan-Santos *et al*. in 1996 proposed the rate equations used

to describe the TADF mechanism based on their observations of the emission of fullerene.[36] This early work did not outline any design rules for the molecular structure of TADF emitters, and thus the development of such materials was slow. This development, however, was fast-tracked by Adachi *et al*. after their work on harvesting the singlet and triplet excitons for applications in OLEDs.[37] Following this, Deaton *et al*. reported an EQE of 16.1% for an OLED doped with a copper(I) complex.[38] The result of these works proved that the dark excitons created in devices, that make up 75% of the excited states, could be re-engaged into useful emission. However, the real breakthrough with this work was in 2011 Adachi *et al*. reported a purely organic TADF emitter for applications in OLEDs.[39] They observed efficient TADF from molecules with an electron donor-acceptor (D-A) type structure. Adachi *et al.* found that this design reduced the overlap of the HOMO and LUMO orbitals resulting in a smaller exchange energy and a smaller ΔE_{ST}.

2.2 The Mechanism of TADF

When an electronically excited state is generated it can decay through a number of competing pathways, Figure 2.1. The simplest pathway is the prompt fluorescence (PF), the energy decays directly from the excited state to the ground state generating light. Engagement of the triplet manifold competes with PF but is a much more complicated process. This process employs the triplet states through intersystem crossing (ISC) from which phosphorescent decay can occur. This phosphorescent decay is unfavourable in OLEDs. However, the reverse of this process, termed reverse intersystem crossing (rISC), is possible when the singlet and triplet energy gap is small and phosphorescence is slow. The process of rISC leads to delayed fluorescence (DF). The design of TADF molecules has therefore focused on the minimisation of the S_1 and T_1 energy gap (ΔE_{ST}). Commonly, this is achieved by using D-A systems that create charge transfer (CT) states within the molecule.

2.3 Kinetic Equations

Early studies into the mechanism of TADF by Parker and later Kirchhoff [34, 40] proposed an equilibrium model that assumed $k_F \ll k_{rISC}$, implying the excited state is populated for long enough to allow an equilibrium to form between the S_1 and T_1 states involved. Using the equilibrium constant K, the relative populations of each excited state can be expressed as shown

$$K = \frac{[S_1]}{[T_1]} = \frac{k_{rISC}}{k_{ISC}} = \frac{1}{3} exp\left\{-\frac{\Delta E_{ST}}{k_B T}\right\} \tag{2.1}$$

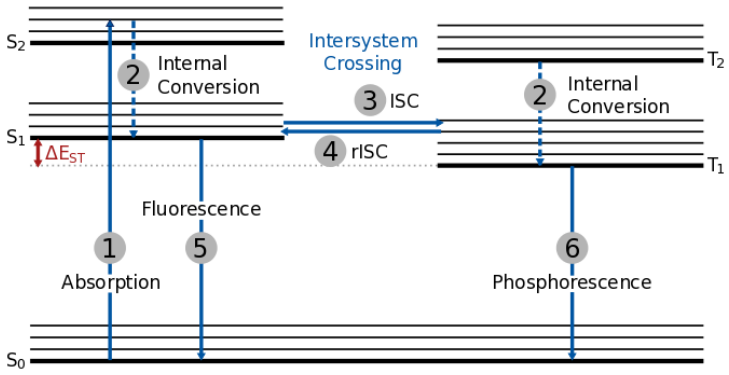

FIGURE 2.1: The emission process of photo-generated excitons for fluorescence (1 - 2 - 5), phosphorescence (1 - 2 - 3 - 6) and thermally activated delayed fluorescence (1 - 2 - 3 - 4 - 5). Adapted from [2].

Furthermore, with the inclusion of the rate limiting step, *i.e* the rate of fluorescence (k_F), it is possible to express the rate of TADF;

$$k_{TADF} = \frac{1}{3} k_F exp\left\{-\frac{\Delta E_{ST}}{k_B T}\right\} \tag{2.2}$$

This work influenced design of TADF molecules that focused on the minimisation of ΔE_{ST}, therefore many TADF molecules were designed with rigid structures. However, Adachi *et al.* reported TADF molecules with IQE reaching close to 100% and upon investigation of these molecules the ΔE_{ST} measured was much larger than expected.[41, 42] The group proposed that the mechanism of TADF must break this key assumption, $k_F \ll k_{rISC}$, to allow for high quantum efficiencies. This amendment to the mechanism changes both the description in terms of theory as well as the design of efficient molecules. [3] With this considered, the mechanism of TADF can be described as a kinetic process[43] if non-radiative pathways are ignored the mechanism can be written as:

$$\frac{dS}{dt} = -(k_F + k_{ISC})[S] + k_{rISC}[T] \tag{2.3}$$

$$\frac{dT}{dt} = k_{rISC}[S] - (k_P + k_{ISC})[T] \tag{2.4}$$

$$\frac{dG}{dt} = k_F[S] + k_P[T] \tag{2.5}$$

where G, S and T represent the electronic ground state, singlet state and triplet state, respectively. k_P and k_F are the rates of fluorescence and phosphorescence, while k_{ISC} and k_{rISC} are the rates of intersystem crossing and reverse intersystem crossing respectively.[5]
To apply this understanding to experimental data, it is useful to write the

kinetic equations as a set of linear differential equations, Equation 2.6.

$$\begin{pmatrix} \frac{dS}{dt} \\ \frac{dT}{dt} \\ \frac{dG}{dt} \end{pmatrix} = \begin{pmatrix} -(k_F + k_{ISC}) & k_{rISC} & 0 \\ k_{rISC} & -(k_P + k_{ISC}) & 0 \\ k_F & k_P & 0 \end{pmatrix} \begin{pmatrix} S(t) \\ T(t) \\ G(t) \end{pmatrix} \tag{2.6}$$

Upon integration, the time dependent population of the electronic states, $P(t)$, can be calculated, Equation 2.7.

$$P(t) = e^{M_t} P(0) \tag{2.7}$$

Where the M is the matrix operating on the populations of the excited states, Equation 2.6, whilst the initial population of each state is $P(0)$.[5]
This understanding can be applied to experimental work to calculate the k_{ISC} and k_{rISC}, however to fully comprehend these two rates, it is important to fundamentally understand the mechanism at work. Furthermore, the spin-vibronic mechanism will be discussed to shed light on the mechanisms at play.

2.3.1 Spin-vibronic mechanism

When first proposed, the TADF mechanism only considered the transition between the ^{1}CT and ^{3}CT states. Furthermore, the k_{rISC} was described using Fermi's golden rule within the Condon approximation, Equation 2.8; this approximation considers the coupling between the electronic and vibrational motion separately.

$$k = \frac{2\pi}{3\hbar Z}(\sum |\langle \psi_T | \hat{H}_{SOC} | \psi_S \rangle|^2 \sum_{k,j} exp^{-\beta E_k} |\langle v_{Tk} | v_{Sj} \rangle|^2 \delta(E_S - E_T) \tag{2.8}$$

Where v describes the vibrational energy levels and $\hat{H}_{SOC}$ describes the spin-orbit Hamiltonian. The molecular energy for the non-radiative transition is conserved by the addition of the δ term. [5] In depth studies of the mechanism of TADF have concluded that the mechanism is more complex than the initial assumption, that only the ^{1}CT and ^{3}CT states are involved. Indeed, this initial assumption presents a problem as ISC between two states of the same character is forbidden. This is as a consequence of the change in spin having no corresponding change in angular momentum so that total angular momentum cannot be conserved.[44] Studies by Monkman *et al.*[3, 45] showed that ΔE_{ST} can be tuned by the environment. This, in turn, concludes that the states involved in TADF must be of different character. Other work in the field by Ward and Group[46] provided further evidence to support this, reporting that TADF could be switched to phosphorescence by choice of the D and A units which form the emitting molecules. Furthermore, Ward *et al.* showed that sterically hindering the D and A units could induce this

switching between TADF and phosphorescence, proposing that the mechanism must involve molecular vibrations. Therefore, this requires a more sophisticated description than that of the Condon approximation.

Indeed, the character of the states involved in this mechanism has moved to the forefront of the field. Chen and Group[42] theoretically calculated the value of k_{rISC} occurring via SOC by the application of Fermi's golden rule. The group included the transition between the ^{1}CT state to the ^{3}LE state. Despite this, when comparing this work to the experimentally measured values, the rates were not concurrent. It was proposed that this was due to the lack of non-adiabatic effects between the low-lying excited states that are involved in the upconversion.[2] In addition, Marian[47] studied the photophysics of the dopant ACRXTN used in a green OLED. The dopant experimentally exhibited a very efficient triplet to singlet transtition that could not be comprehensively described by its small ΔE_{ST}. Upon invesigation it became evident that five electronically excited states were involved in the mechanism. These states were characterised as the expected ^{1}CT and ^{3}CT, as well as a local triplet ($\pi\pi^*$) and a pair of singlet and triplet $n\pi^*$ states. The work postulated that the mechanism of TADF involves mixing with the close lying ^{3}LE states. Despite these works identifying that multiple states are involved neither provide a comprehensive mechanism of the process. Later, Gibson *et al*.[2] reported a study of 3,7-PTZ-DBTO2 that investigated and characterised the exact mechanism of k_{rISC} using model quantum dynamics simulations. The Group identified that the ^{1}CT, ^{3}CT and $\pi\pi^*$ were crutial for TADF, with this considered, they proposed a model Hamiltonian to describe the mechanism of rISC. Furthermore, Gibson *et al.* proposed that TADF could be described by three spin-vibronic coupling mechanisms.[2]

- Vibrational spin-orbit. The size of the spin orbit coupling matrix elements (SOCME) is dependent on the movement along a nuclear degree of freedom.
- Singlet manifold spin-vibronic. SOC with non-adiabatic coupling between the many singlet states.
- Triplet manifold spin-vibronic. SOC with non-adiabatic coupling between the many triplet states.

With knowledge of the properties that are involved in the mechanism of TADF, it is possible to begin to predict effective molecular design.

2.4 Designing TADF molecules

Understanding rISC and TADF influences the design of the molecules for applications in OLEDs. Firstly, when considering the mechanism of rISC as

kinetic, the dynamical nature, in the sense that it depends on molecular vibrations, must be understood and the theory must go beyond the Condon approximation. Here, making the molecules too rigid to prevent non-radiative decay can be problematic and presents the dynamics rISC mechanism.

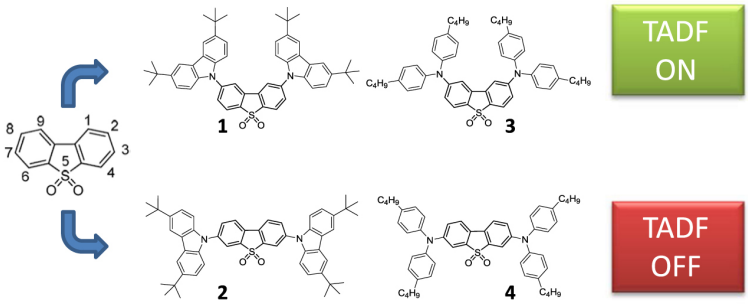

FIGURE 2.2: The influence of position of substitution of electron donor (D) and electron acceptor (A) units on the TADF of the system.[3] From [4].

It is also important to understand the influence of geometry and conformation of the system and how it can be tuned to further improve TADF contributions. It is well known that the conformation a molecule can influence its properties. However, the role of such isomerisation in photophysics remains relatively underdeveloped.[5] Using 3,7-PTZ-DBTO2 [5] the effect of different conformations on the TADF were demonstrated. Indeed, as shown in Figure 2.3, the phenothiazine D unit exhibits two key conformations, a quasi-equatorial and a quasi-axial, with respect to the N-S axis and the plane of the phenyl rings. Notably, the distribution of the HOMO is delocalised across the whole molecule when in the quasi-axial conformer, as opposed to being localised on the D in the quasi-equatorial form. This delocalisation will reduce the efficiency of the TADF, because the CT state will be weaker. Importantly, these conformers are locked in the ground state due to the large >1 eV energy barrier between them. However, when investigating the molecules in the excited state the energy barrier was significantly smaller. In fact, the quasi-axial form has an energy that is only 0.24 eV lower than the barrier. Therefore the quasi-axial conformer could switch to the equatorial form if any excess energy was present in the system and this has a large effect on the TADF performance of the molecules [5, 48].

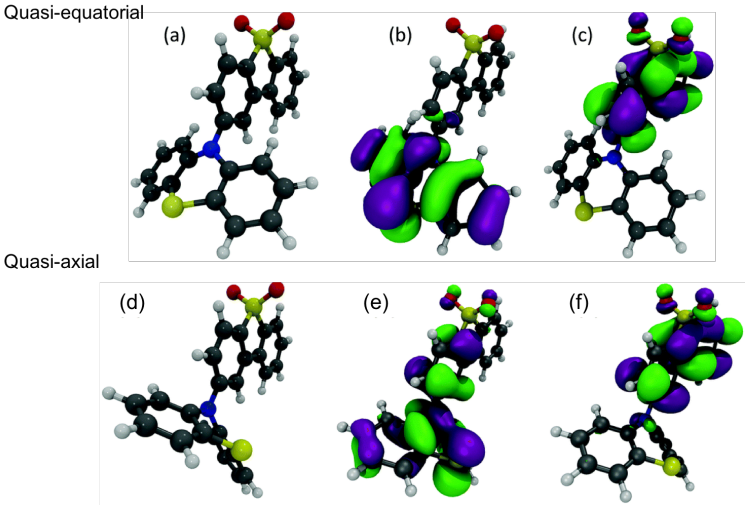

FIGURE 2.3: The quasi-equatorial and quasi-axial conformers of 3, 7-PTZ-DBTO2, (a) and (d) respectively. (b) and (f) are the structures of the HOMO, (c) and (e) are the structures of the LUMO. Adapted from [5].

Chapter 3

Circularly Polarised Light (CPL)

3.1 Background

Chirality is a property of symmetry and shape that has been central to many discussions in many different areas of research. Within the pharmaceutical industry, molecular chirality is utilised to tune the interaction of the drug with the biological receptor.[20] Tuning the chirality when synthesising the drug consistently proves a challenge but, if successful, can result in many valuable products reaching market, particularly in the pharmaceutical sector. However, the application at the centre of this work, chiral light, is very different but also based on chirality. Given the growth of display technology and the integration of OLED screens into many smart phones, chiral light emission can be harnessed to improve this technology.[49] Chiral light emission can also be used to encode information, in spectroscopy and in optics and filters. Therefore, it is of great interest in quantum computing,[50] three-dimensional displays[51] and bioresponsive imaging[52]. However, with the chirality of light being the focus of this work, it thus requires a description. CP light, as seen in Figure 3.1, consists of two plane polarised waves with equal amplitudes that are at right angles to each other, with a quadrature phase relationship. The effect of this is a helical trace as the resultant electric field vector is of constant magnitude and continues to rotate at a constant rate. Now forming a helical object, similar to the structure of DNA, the light is thus chiral and can either display RH or LH emission. Spectroscopic methods such as, electronic and vibrational circular dichromism (ECD, VCD), optical rotation dispersion (ORD) and Raman optical activity (ROA) can show the interaction of CP light and chiral molecules.[53, 54, 55, 56] The research landscape surrounding display technology is an ever changing field. The commercialisation of OLEDs in devices, such as televisions, has increased industrial interest into the research area. For display technology, controlling the dissymmetry of CP light in devices could generate superior efficiencies and brightness, whilst simplifying the device architecture as polarisers could no longer be required.[57] CP light is usually assumed to require the use of chiral molecules. However, an emerging approach is to blend achiral polymers and chiral small molecule additives, which has been shown to induce CP electroluminescence.[57]

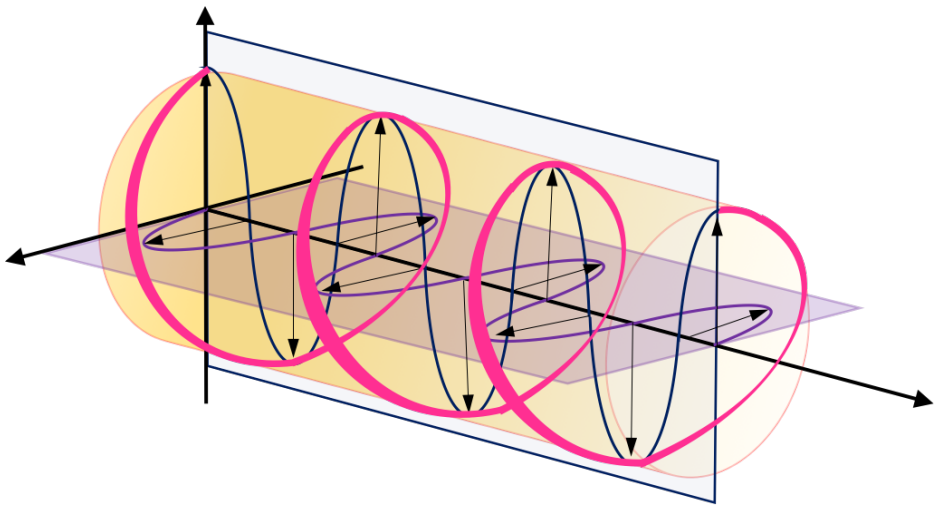

FIGURE 3.1: A scheme to illustrate circularly polarised light. It is made up of two plane polarised waves with equal amplitudes (navy blue and purple) that are at right angles to each other, with a quadrature phase relationship. The helical trace is shown in pink, as the resultant electric field vector is of constant magnitude and continues to rotate at a constant rate.

Recent discussions have proposed two mechanisms responsible for the emission of CP light in CP-OLEDs.[57] The first is the intrinsic emission from the CP chromophore.[58, 59] These chiral organic materials can be grouped into two classes; small molecule emitters[60, 61, 62] and polymer-based emitters[63, 64]. The second is the extrinsic CP emission, arising from the interaction between domains of chromophores within the active layer of a device.[65]

3.2 Theory

For an intrinsically chiral chromophore, or chromophore in a chiral environment, the electronic circular dichromism (CD) originates from the difference in the left and right circularly polarized light. The molar circular dichromism ($\Delta\epsilon$) is defined as a function of wavelength in CD spectroscopy:

$$\Delta\epsilon(\lambda) = \epsilon_L(\lambda) - \epsilon_R(\lambda) \tag{3.1}$$

Where ϵ_L and ϵ_R are the molar extinction coefficients for left and right polarised light, respectively. Furthermore, the absorptive dissymmetry factor (g_{abs}) can be used to quantify the magnitude of CD. CP light is commonly described by its dissymmetry factor, g, experimentally it is calculated as seen in Equation 3.2.[58, 59]

$$g = 2\frac{I_L - I_R}{I_L + I_R} \tag{3.2}$$

Where, R and L refer to the handedness of the light and I can be the intensity of photoluminescence or electroluminescence. The capability to control this, and furthermore force the handedness to be exclusively one way or the other, will greatly improve the efficiency of the CP light emitting system in a device. Therefore, the sign of dissymmetry calculated from theoretical studies is important to compare with experiment.
The g-factor for small molecule emitters is determined using electronic and magnetic transition dipole moments, $\boldsymbol{\mu}$ and $\mathbf{m}$ respectively, which is expressed as:

$$g = \frac{4R_{0n}}{D} \tag{3.3}$$

R is the rotary strength[66] defined as:

$$R_{0n} = Im\{\boldsymbol{\mu}_{0n} \cdot \mathbf{m}_{0n}\} \tag{3.4}$$

Where 0 and n refer to the ground state and the nth excited state, respectively, involved in the electronic transition. Whilst the electronic, $\boldsymbol{\mu}$, and magnetic, $\mathbf{m}$, transition dipole moments can be defined as:

$$\boldsymbol{\mu}_{0n} = -\langle \Psi_n | \mathbf{r} | \Psi_0 \rangle \tag{3.5}$$

$$\boldsymbol{m}_{0n} = -\frac{1}{2c} \langle \Psi_n | \mathbf{L} | \Psi_0 \rangle \tag{3.6}$$

where $\mathbf{r}$ and $\mathbf{L}$ are the position and angular momentum operators. The intensities of the absorption and emission are proportional to the relevant dipole strength (D) defined:

$$D = |\boldsymbol{\mu}_{0n}|^2 + |\mathbf{m}_{0n}|^2 \tag{3.7}$$

Equation 3.7 is applicable to the g-factor for both the absorption and emission. The only difference is that the absorption measures the g-factor for the thermally equilibrated electronic ground state, whereas the emission reflects the structure of the emissive excited state.[67] With the interplay between the $\boldsymbol{\mu}$ and $\mathbf{m}$ being so crucial to this work, it is important to consider that in the optical regime wavelengths of electromagnetic waves are much larger than the size of a typical molecule. One way to describe the behaviour of electromagnetic waves is by using the vector potential of a set of plane waves:

$$A(\mathbf{r}, t) = A_0 e^{i(\mathbf{k}\cdot\mathbf{r} - \omega t)} + A_0^* e^{-i(\mathbf{k}\cdot\mathbf{r} - \omega t)}. \tag{3.8}$$

were ω is the angular frequency of the wave oscillating in time and propagating in the direction along the wavevector $\mathbf{k}$, with a spatial period $\lambda = 2\pi/|\mathbf{k}|$. A_0 describes the amplitude of the wave. Furthermore, from the vector potential, we can obtain E for the electronic part of the wave:

$$E = -\frac{\partial \hat{A}}{\partial t} = i\omega A_0 (e^{i(\mathbf{k}\cdot\mathbf{r} - \omega t)} - e^{-i(\mathbf{k}\cdot\mathbf{r} - \omega t)}). \tag{3.9}$$

describing the electric field of light. The vector potential oscillates as $cos(\omega t)$ whilst the field oscillates as $sin(\omega t)$. Furthermore, if we define

$$\frac{1}{2}E_0 = i\omega A_0 \tag{3.10}$$

then

$$E(\mathbf{r}, t) = |E_0| sin(\mathbf{k} \cdot \mathbf{r} - \omega t). \tag{3.11}$$

Therefore, the exponential operator responsible for the spatial term of the radiation field, $exp(i\mathbf{k} \cdot \mathbf{r}_i)$, when expanded as a Taylor series:

$$exp(i\mathbf{k} \cdot \mathbf{r}_i) = 1 + i(\mathbf{k} \cdot \mathbf{r}_i) - \frac{1}{2}(\mathbf{k} \cdot \mathbf{r}_i)^2 + ... \tag{3.12}$$

may be truncated at zeroth order, *i.e.* the spatial dependence is neglected, and this corresponds to the electric dipole approximation. First-order terms include the electric quadrupole and magnetic dipole terms only become significant for electric dipole forbidden transitions or when **kr** exceeds unity. This is achieved either at high photon energies or if the excited state extends in size, *i.e.* approaches the wavelength of the light emitted.[68, 69]

3.3 Exciton Chirality Model

The method described above is used to explain the inherent chiral emission from individual molecules. Expanding from a one molecule system to a larger system, for example a dimer, requires a description of the interplay between the systems. A single molecule that does not possess any inherent chirality, can display chiral properties when a dimer of two of these same single molecules is formed. To describe this phenomena, the exciton chirality model (ECM) is commonly applied. The ECM was first coined by Harada *et al.* in 1972.[70] The work outlined how the ECM could be applied to natural products to deduce their absolute configurations. The model can be applied to molecules that are inherently achiral that form dimers with an angle between the orbitals, so they do not overlap exactly. This interaction can be described using the electronic dipole moments as the individual molecules do not have an initial magnetic dipole moment as they are not inherently chiral.
For a dimer with coupled excited states, the rotatory strength (R) is:

$$R = \pm\frac{1}{2}\pi\sigma d_{kl} \cdot (\boldsymbol{\mu}_k \times \boldsymbol{\mu}_l) + \frac{1}{2}Im\{(\boldsymbol{\mu}_k \pm \boldsymbol{\mu}_l) \cdot (\mathbf{m}_k \pm \mathbf{m}_l)\} \tag{3.13}$$

where d_{kl} is the distance between the two individual molecules, k, l and σ is the transition energy. It is assumed that the electronic transition dipole moment will be much larger than the magnetic transition dipole moment,

and thus the rotatory strength can be described just using the electronic part, $\boldsymbol{\mu}$, the first term in Equation 3.13. Put simply, for large systems, where it is very difficult to calculate the properties, the chirality can be estimated to arise from the two electric transition dipole moments. Similar to how atomic orbitals form molecular orbitals, in which there is a bonding and antibonding interaction. This approximation therefore makes the exciton chirality model a more simplistic calculation and reasonable approximation when applied to an appropriate system. However, as with any approximation, there are systems that require a description beyond the limits of this representation. This work will investigate beyond just the first term of Equation 3.13 and include the magnetic transition dipole moments when calculating the rotary strength for large systems. Such cases are discussed in more detail in Chapter 7.

Chapter 4

Theory and Methodology

This chapter outlines the theory and methodology that underpins the research carried out throughout this thesis. Beginning with the Schrödinger equations, followed by the methodology of the computational methods used in this work.

4.1 The Schrödinger Equation

Newtonian mechanics are used to predict and describe the behaviour of classical systems. However, particle-like and wave-like properties must be considered on when describing systems on the molecular scale, these are described using quantum mechanics. The equation that is central to quantum mechanics, within the non-relativistic limit, is the Schrödinger equation. When describing the evolution of a quantum system, the time-dependent Schrödinger equation (TDSE) is used. This is expressed:

$$i\hbar\frac{\partial}{\partial t}\Psi(\boldsymbol{R},\boldsymbol{r},t) = H\Psi(\boldsymbol{R},\boldsymbol{r},t) \tag{4.1}$$

It is used to solve the wavefunction and properties of a quantum mechanical system. Here, H is the Hamiltonian operator of the chemical system, Ψ is the many particle wavefunction which depends on the nuclear coordinates $\boldsymbol{R}$ and the electronic coordinates $\boldsymbol{r}$ and time, t. i is the $\sqrt{-1}$ and $\hbar$ is the reduced Plank's constant.

One method for solving the TDSE is to express the wavefunction as a product of the spatial $(\Phi(\boldsymbol{R},\boldsymbol{r}))$ and temporal $(T(t))$ components:

$$\Psi(\boldsymbol{R},\boldsymbol{r},t) = \Phi(\boldsymbol{R},\boldsymbol{r})T(t) \tag{4.2}$$

Substituting this into the TDSE and dividing through by the overall wavefunction yields two equations, one is focused purely on the time-evolution and the other is the time-independent Schrödinger equation written:

$$H\Phi(\boldsymbol{R},\boldsymbol{r}) = E\Phi(\boldsymbol{R},\boldsymbol{r}) \tag{4.3}$$

The time-independent Schrödinger equation (TISE) is commonly used as the fundamental equation used to solve the structure of the electrons within quantum chemistry methods that results in the energy of the system, E. This is the focus of the present thesis, but approximations to solve this are described in detail below.

The Hamiltonian described above is composed of kinetic and potential energy parts and can be written as:

$$\begin{aligned} H &= -\sum_{I=1}^{Nn} \frac{\nabla^2_{\boldsymbol{R}_I}}{2M_I} + \sum_{I=1}^{Nn}\sum_{J>I}^{Nn} \frac{Z_I Z_J}{|\boldsymbol{R}_I - \boldsymbol{R}_J|} - \sum_{i=1}^{N_e} \frac{\nabla^2_{\boldsymbol{r}_i}}{2} + \sum_{i=1}^{N_e}\sum_{j>i}^{N_e} \frac{1}{|\boldsymbol{r}_i - \boldsymbol{r}_j|} + \sum_{i=1}^{N_e}\sum_{J=1}^{N_n} \frac{-Z_J}{|\boldsymbol{r}_i - \boldsymbol{R}_J|} \\ &= T^n + V^{nn} + T^e + V^{ee} + V^{ne} \end{aligned} \tag{4.4}$$

where M is nuclear mass, $\mathbf{R}$ is nuclear coordinate and N_n is the number of nuclei. Z is the nuclear charge, $\mathbf{r}$ is the electronic coordinate, and N_e is the number of electrons. The T and V terms are the kinetic and interaction energies. T^n and T^e are the kinetic energy expressions for the nuclei and electrons, respectively. Both kinetic energy terms are expressed as second derivative operators with respect to their specific coordinate, either nuclear, R or electronic r. The three potential energies correspond to the nucleus-nucleus, V^{nn}, electron-electron, V^{ee}, and nucleus-electron, V^{ne} terms.

Equation 4.4 shows that even in the simplest cases, it is very difficult to solve the Schrödinger equation analytically due to the large number of terms. Consequently, to solve it several approximations must be made. The first, which is the cornerstone of quantum mechanics, is the Born-Oppenheimer approximation.[71] This utilises the huge difference in mass between the electrons and nuclei. The mass difference means that the electrons can be considered much faster than the nuclei. Consequently, for any change in nuclear positions, the electrons adapt instantaneously. Therefore we may consider the nuclei fixed and solve the equation for nucleus. The Born-Oppenheimer approximation is derived by expressing the wavefunction as:

$$\Phi(\boldsymbol{R}, \boldsymbol{r}) = \psi(\boldsymbol{r}; \boldsymbol{R})\phi(\boldsymbol{R}) \tag{4.5}$$

This is so-called Born–Huang (BH) representation, where ψ is the electronic component of the wavefunction which depends on the electronic coordinates and parametrically on the nuclear coordinates, ϕ is nuclear component which depends on the nuclear coordinates. By inserting this *ansatz* into to TISE, multiplying everything through by ψ^* and integrating over all the electronic coordinates, $\boldsymbol{r}$, leads to a series of coupled equations of motion for the nuclear wavefunction. Importantly, all of these address the electronic and nuclear degrees of freedom separately, except the last which expresses the second derivative of the electronic wavefunction with respect to the nuclear coordinates. When the system is close to a minimum on the potential energy

surface, such as the ground state, this term is very small and can be approximately ignored. This approximation decouples the electronic and nuclear motions. This gives the electronic Hamiltonian:

$$H^e\psi^e = [T^e + V^{ee} + V^{ne}]\psi^e. \tag{4.6}$$

The kinetic energy of the nuclear is neglected, they are considered fixed in space. The potential energy arising from the Coulombic nuclei-nuclei repulsion gives rise to a constant shift and is often neglected from the calculations. In some cases, especially in the case of electronically excited states which are highly non-equilibrium and which is the focus of the present thesis, this final term that separates the electronic and nuclear coordinates, is not small and cannot be neglected. This gives rise to non-adiabatic effects.

Even within the Born-Oppenheimer approximation, it is generally not possible to numerically solve the electronic Schrödinger equation apart from in a small number of cases. For example, the electronic Schrödinger equation can be solved numerically for a hydrogen atom, this is due to the small number of electrons in the hydrogen atom. Problems begin as the number of electrons in the system increase, $\psi^e = \psi(\boldsymbol{r}_1, \boldsymbol{r}_2 \ldots \boldsymbol{r}_{Ne})$ increases to become a high dimensional object. There is a $3N_e$ scaling factor of the co-ordinates. Furthermore, it quickly becomes necessary to find suitable approximations to solve the electronic Schrödinger equation.

4.2 Methodology

Throughout this work, computational methods have been used to describe both the ground and excited states of molecular systems. Density functional theory (DFT) is used to solve the ground state properties. Whereas, time-dependent density functional theory (TDDFT) is used to solve the excited state properties of a system using time and an external field to excite the system. Molecular dynamics (MD) is used to describe the dynamical properties of a many-bodied system. As it provides a useful starting point, the foundations of Hartree-Fock theory are first described.

4.2.1 Hartree-Fock Method

The Hartree-Fock theory starts on the premise that we know how to solve the electronic Schrödinger equation for the hydrogen atom. The first approximation from the Schrödinger equation is that T^e + V^{ne} is treated as an external

field, so all atoms feel the same effect of V^{ne}.

$$\begin{aligned} H &= -\sum_{i=1}^{N_e} \frac{\nabla_{\boldsymbol{r}_i}^2}{2} + \sum_{i=1}^{N_e}\sum_{j>i}^{N_e} \frac{1}{|\boldsymbol{r}_i - \boldsymbol{r}_j|} + \sum_{i=1}^{N_e}\sum_{J=1}^{N_n} \frac{-Z_J}{|\boldsymbol{r}_i - \boldsymbol{R}_J|} \\ &= \sum_{i}^{n} h(\boldsymbol{r}_i) + \sum_{i=1}^{N_e}\sum_{j>i}^{N_e} \frac{1}{|\boldsymbol{r}_i - \boldsymbol{r}_j|} \end{aligned} \tag{4.7}$$

The second equation separates the Hamiltonian into terms which depend on one and two electrons, respectively.

Furthermore, the method relies on the Hartree approximation, which allows for the simplification of the wavefunction, ψ, by assuming that the single particle wavefunctions can be separated, expressing the wavefunction as a product of the single particle wavefunctions.

$$\psi_{HP}(\boldsymbol{r}_1, \boldsymbol{r}_2, \ldots, \boldsymbol{r}_N) = \psi_1(\boldsymbol{r}_1)\psi_2(\boldsymbol{r}_2)\ldots\psi_N(\boldsymbol{r}_N). \tag{4.8}$$

However, this ignores electron-electron interactions, which is a poor approximation. To rectify this, the Hartree product is substituted into the full electronic Hamiltonian, including the electron-electron interaction via a mean field approximation. The mean field approximation applies an averaged interaction to any one electron, thus reducing a many-body system to a simpler picture where only one average interaction is applied. Importantly, the Hartree product is not satisfactory for fermions such as electrons, because the resulting wave function is not antisymmetric, stating that when the positions of two electrons are exchanged the sign of the wavefunction is swapped. This known as the exchange interaction. If the Hartree product is used, one accounts for the Pauli principle "by hand", by allowing only two electrons to occupy the same spatial orbital. By starting with a Hartree product, enforcing the Pauli principle and applying the variational principle one obtains the Hartree equations, which are similar to the Hartree-Fock ones but, as stated previously these miss the exchange term. While this term is, however, smaller than the electrostatic term in the Hartree calculations it remains very important to include them. To overcome these problems, Slater determinants can be used:

$$\psi(\boldsymbol{r}_1, \boldsymbol{r}_2) = \frac{1}{\sqrt{2}}[\chi_1(\boldsymbol{r}_1)\chi_2(\boldsymbol{r}_2) - \chi_1(\boldsymbol{r}_2)\chi_2(\boldsymbol{r}_1)] \tag{4.9}$$

Determinants can be used to to generalise the solution, but first we consider how determinants look for the two electron system.

$$\psi(\boldsymbol{r}_1, \boldsymbol{r}_2) = \frac{1}{\sqrt{2}} \begin{vmatrix} \chi_1(\boldsymbol{r}_1) & \chi_2(\boldsymbol{r}_1) \\ \chi_1(\boldsymbol{r}_2) & \chi_2(\boldsymbol{r}_2) \end{vmatrix} \tag{4.10}$$

As a consequence of the antisymmetry principle, if we attempt to put two electrons in one orbital at the same time $\psi(\boldsymbol{r}_1, \boldsymbol{r}_2) = 0$, an accurate description

of a chemical system. Furthermore, to generalise for N electrons:

$$\psi(\boldsymbol{r}_1, \boldsymbol{r}_N) = \frac{1}{\sqrt{N!}} \begin{vmatrix} \chi_1(\boldsymbol{r}_1) & \chi_2(\boldsymbol{r}_1) & \cdots & \chi_N(\boldsymbol{r}_1) \\ \chi_1(\boldsymbol{r}_2) & \chi_2(\boldsymbol{r}_2) & \cdots & \chi_N(\boldsymbol{r}_2) \\ \vdots & \vdots & \ddots & \vdots \\ \chi_1(\boldsymbol{r}_N) & \chi_2(\boldsymbol{r}_N) & \cdots & \chi_N(\boldsymbol{r}_N) \end{vmatrix}. \tag{4.11}$$

The important consequence of this is that the electrons are all indistinguishable, as they should be in quantum mechanics. Each electron is associated with every orbital. This point is very easily forgotten, especially because it is cumbersome to write out the whole determinant which would remind us of this indistinguishability.

The assumption that the electrons can be described by an antisymmetrized product is equivalent to the assumption that each electron moves independently of all the others except that it feels the Coulomb repulsion due to the average positions of all electrons. The inclusion of the Slater determinant also causes the introduction of a new term, the exchange contribution also known as the Fock-term. This term takes into account the effect of the configurations where two electrons, that are indistinguishable, are exchanged. This correlation is due to the Pauli exclusion principle and thus, effects only the electrons with the same spin state, the electrons with opposite spin are completely uncorrelated. Hence, Hatree-Fock theory is also referred to as an independent particle model or a mean field theory. Many of these descriptions also apply to Kohn-Sham density functional theory, which bears a striking resemblance to Hartree-Fock theory; one difference, however, is that the role of the Hamiltonian different in DFT, as described below.

4.2.2 Density Functional Theory

Solving the electronic Schrödinger equation was traditionally performed using methods such as Hartree-Fock (HF) theory and associated post Hartree-Fock theory. However, these become computationally expensive for large systems. The groundwork for DFT was completed in the 1960's by Kohn and Sham. Since then, DFT became a focus of many publications in chemistry in the 1990's, and it has continued to be a mainstay in research since.[72] DFT provides many routes to the electronic structure properties of a many-body system. Previously, in section 4.1, the electronic Schrödinger equations were described using the many-body wavefunction approach. However, the wavefunction approach does come with intrinsic limitations, such as, the 3N-many coordinate scaling problem. A simple description of the 3N-many coordinate scaling problem, states that each electron in a system has three degrees of freedom, and can move in the x, y or z direction. The additional degrees of freedom for each electron that is added to a system, needs to be considered with each degree of freedom of the initial system and thus, the system scales with $(3N)^3$. The way that DFT approaches this problem is to

use the electronic density, which describes all of the electrons in the ground state system, written:

$$n(\boldsymbol{r}) = N \int \dots \int |\Phi(\{x_i\})|^2 d\sigma dx_2 \dots dx_N$$
$$\int n(\boldsymbol{r}) d\boldsymbol{r} = N \tag{4.12}$$

However, how can we be sure that using the electronic density rather than the wavefunction provides a rigorous and correct description of the system? Hohenberg and Kohn provided this answer with their first theorem in 1964.[73]

The First Hohenberg-Kohn Theorem

The first Hohenberg-Kohn Theorem shows that the ground state density, $n(\boldsymbol{r})$, determines the external potential, V^{ne}, and is proven by contradiction. Consider that the ground state density, $n(\boldsymbol{r})$, is the same for two external potentials, V_1 and V_2, therefore each potential has its own distinct Hamiltonian, H_1 and H_2 respectively, and its own distinct wavefunction, Φ_1 and Φ_2 respectively. By application of the of the variational principle,

$$E_1 = \langle \Phi_1 | H_1 | \Phi_1 \rangle < \langle \Phi_2 | H_1 | \Phi_2 \rangle \tag{4.13}$$

and

$$\langle \Phi_2 | H_1 | \Phi_2 \rangle = \langle \Phi_1 | H_2 | \Phi_1 \rangle + \langle \Phi_1 | H_1 - H_2 | \Phi_1 \rangle = E_2 + \int n(\boldsymbol{r}) [V_1(\boldsymbol{r} - V_2(\boldsymbol{r})] \, d(\boldsymbol{r}). \tag{4.14}$$

So,

$$E_1 < E_2 + \int n(\boldsymbol{r}) [V_1(\boldsymbol{r}) - V_2(\boldsymbol{r})] \, d(\boldsymbol{r}) \tag{4.15}$$

Swapping the indexes in equations 4.13 and 4.14 gives

$$E_2 < E_1 + \int n(\boldsymbol{r}) [V_2(\boldsymbol{r}) - V_1(\boldsymbol{r})] \, d(\boldsymbol{r}) \tag{4.16}$$

Furthermore, if these two inequalities are added

$$E_1 + E_2 < E_1 + E_2 \tag{4.17}$$

is produced, which is contradictory. This contradiction proves that there will never be two different external potentials which both describe the ground state density, and therefore the theorem is true.

The Second Hohenberg-Kohn Theorem

The second Hohenberg and Kohn theorem is employed to prove that the energy described by the ground state electronic density is in fact the lowest energy of the system. Using the knowledge obtained from the first theorem,

we know that a specific external potential describes the ground state electronic density, $n(\boldsymbol{r})$, of the system. Therefore, any other external potential must correspond to a density that is of higher energy, $\tilde{n}(\boldsymbol{r})$, this is what the second Hohenberg-Kohn theorem describes.

$$E[n] \leq E[\tilde{n}] \tag{4.18}$$

Overall, from these two theorems we know that we can describe all properties of a system using a discrete functional of the density, but how can we describe this functional? Here we employ the Kohn-Sham equations.

Kohn-Sham DFT

The Hohenberg-Kohn Theorems provide the framework for DFT, but do not provide a practical method. This latter aspect was achieved by the work of Kohn and Sham. The Kohn-Sham equations describe the real ground state electronic density by building an auxiliary system of non-interacting electrons. This system is then acted on by a fictitious external potential, known as the Kohn-Sham potential, $V = V_{aux}(r) = V_{eff}(r)$.[74]

$$H \rightarrow \sum_{i=1}^{N} h_{aux}(r_i) = H_{aux}(\{r_i\}) \tag{4.19}$$

The many-body Hamiltonian can be rewritten as a sum of single particle Hamiltonians:

$$h_{aux}(r_i)\varphi_i(r_i) = \epsilon_i \varphi_i(r_i) \tag{4.20}$$

therefore, the many-body wavefunction is a single Slater determinant. Furthermore, the electronic density can be described by:

$$n(\boldsymbol{r}) = \sum_{i=1}^{N} \int |\varphi_i(\boldsymbol{r}, \sigma)|^2 \, d\sigma \tag{4.21}$$

from this it is possible to describe the kinetic energy in the following way,

$$T[n] = \sum_{i=1} \langle \varphi_i | \frac{\nabla^2}{2} | \varphi_i \rangle \tag{4.22}$$

but, this cannot be considered the true kinetic energy of the system because it is describing a fictitious system. Therefore, the Kohn-Sham energy is:

$$E_{KS}[n] = T[n] + E_H[n] - \int n(\boldsymbol{r}) V(\boldsymbol{r}) + E_{xc}[n] \tag{4.23}$$

here $E_{xc}[n]$ is made up of many constituent parts. Firstly, it includes the difference between the electron-electron interaction energy and the Coulomb

interaction energy, as well as the energy difference between the kinetic interaction of the real system and the non-interacting system. Therefore, it is possible to solve, for the Kohn-Sham energy, self-consistently:

$$[-\frac{\nabla^2}{2} + \frac{1}{2}\int \frac{n(\boldsymbol{r'})}{|\boldsymbol{r}-\boldsymbol{r'}|}d\boldsymbol{r'} + V(\boldsymbol{r}) + V_{xc}(\boldsymbol{r})]\varphi_i(\boldsymbol{r}) = \epsilon_i\varphi_i(\boldsymbol{r}) \tag{4.24}$$

where V_{xc} is a functional derivative of the exchange correlation potential. However, this exchange correlation functional is not known exactly and many methods have been developed to approximate it.

The nature and form of the exchange correlation functional is where the majority of the research focus of density functional theory is. Indeed, at this point it is important to stress, as mentioned above, that it is often assumed that expressing the system as a density, whose size is independent on the number of electrons, is where the real strength of DFT lies. However, expressing the DFT equations within the Kohn-Sham framework and single particle Kohn-Sham orbitals reintroduces a scaling comparable to Hartree-Fock theory. Consequently, the real power of DFT lies in the fact that it starts from a non-interacting system, which is relatively simple to calculate. Although this is a terrible approximation, it transpires that relative simple approximations to the exchange correlation functional provide accurate properties. Provided the function is simpe to calculate, DFT becomes an incredibly powerful technique able to address the quantum properties of large systems. The approximations to this are explored in the following sections.

4.2.3 Exchange and Correlation Functionals

In principle DFT is an exact theory however, for this to be fulfilled the exact exchange and correlation energy, E_{xc}, must be known. To calculate the exact E_{xc} requires great computational cost and in reality is impossible, therefore, many approximations for the exchange and correlation term have been made in the form of functionals. Each functional reaches different levels of accuracy depending on the level of approximation made. As the functionals become more exact, they are said to be higher on Jacobs ladder.[75] However, in general, new functionals are not getting more accurate, they are specialising and therefore losing generality in the process.[76, 77] It is unlikely that a general and precise functional will ever be found.

The Local Density Approximation

The first approximation is the local density approximation (LDA) which is exact only for the homogeneous electron gas and therefore, can be considered a reasonable approximation for systems with a slow perturbation of the density. Such a system can be considered to have a constant external potential because it will locally appear to have a constant density. From the

homogeneous electron gas equation, the exchange correlation energy for the LDA can be written as:

$$E_{xc}[n] = \int n(\boldsymbol{r})\epsilon_{xc}(n(\boldsymbol{r}))\ d(\boldsymbol{r}) \tag{4.25}$$

where $\epsilon_{xc}(n(\boldsymbol{r}))$ is the energy per electron at the point $\boldsymbol{r}$ in space that only depends on the density at that point. Splitting the exchange correlation energy into its constituent energy densities gives:

$$\epsilon_{xc}(n(\boldsymbol{r})) = \underbrace{\epsilon_x(n(\boldsymbol{r}))}_{\text{exchange energy density}} + \underbrace{\epsilon_c(n(\boldsymbol{r}))}_{\text{correlation energy density}} \tag{4.26}$$

and applying HF theory to calculate the exchange energy density gives,

$$\epsilon_x(n(\boldsymbol{r})) = \frac{3}{4}(\frac{3}{\pi})^{1/3} \int n(\boldsymbol{r})^{4/3}\ d\boldsymbol{r}. \tag{4.27}$$

The exchange potential for the LDA is simply,

$$V_x(\boldsymbol{r}) = (\frac{3}{\pi})^{1/3}\ n^{1/3}(\boldsymbol{r}). \tag{4.28}$$

Therefore, the LDA provides a reasonable solution to the exchange correlation term that scales linearly with system size. However, it does underestimate the Kohn-Sham energy eigenvalues due to self-interaction errors, making it unsuitable for many chemical systems.

Generalised-Gradient Approximation

To improve the LDA, which operates under the assumption that the density changes very slowly, the gradients of the electron density are added to the exchange correlation. This is known as the generalised-gradient approximation (GGA),

$$E_{xc}^{GGA} = \int f(n(\boldsymbol{r})\nabla n(\boldsymbol{r})\ d(\boldsymbol{r}). \tag{4.29}$$

The GGA provides a computationally inexpensive route to more accurate DFT calculations, specifically accurate descriptions of structures. Some popular GGA functionals include PBE[78] and BLYP[79, 80].

Hybrid Functionals

GGA functionals, however, often fail to accurately describe non-local properties, such as CT states and van der Waals bonding. Such failings can be attributed to the GGA functionals poor description of long range electron-electron interactions, as well as the poor description of the rapid decay of the exchange and correlation potentials.[81] These inaccuracies are in part due to the self-interaction error in DFT. Unlike in DFT, Hartree-Fock theory exactly

cancels the interaction of an electron with itself by the exchange term. However, in DFT, this exchange term is approximated and so does not exactly cancel the self-interaction, resulting in surplus self-interaction. Therefore, hybrid functionals were developed, built using a portion of exact exchange from HF mixed with a portion of exchange from DFT. This produces functionals of the form:

$$E_{xc}^{hybrid} = aE_x^{HF} + (1-a)E_x^{DFT} + (1-a)E_c^{DFT}. \tag{4.30}$$

The implication of a hybrid functional can improve the accuracy of many properties, such as, bond lengths, vibration frequencies and the description of excited states. Examples of commonly used hybrid functionals are B3LYP[80, 82, 83] and PBE0[84].

Long-range corrected DFT

Long-range corrected, or range-separated functionals, are another class of hybrid functionals. Koopmans optimal tuning (OT) approach is a popular approach in the long-range corrected method.[85] This approach takes the vertical ionisation potential (IP) and the negative eigenvalue of the HOMO, and sets the range separation parameter, ω, to be in agreement.[8] Koopmans OT method was developed for single particles and must be further investigated before it can be confidently applied to the excited state. One method that has been tested on a range of TADF molecules, and has shown favourable results when compared to the Koopmans tuning approach, is the triplet tuning approach proposed by Lin and Van Voorhis.[86] This approach is based on the expectation that if the exchange correlation functional is exact, then DFT and TDDFT calculations should produce the same lowest triplet excitation energies. However, this is not the case for many commonly used exchange functionals. Therefore, this method constructs a bespoke exchange functional by minimising the energy difference between DFT and TDDFT calculations for each system.[86]

Long range corrected DFT can be split into short range and long range domains of the two electron interaction operator, $\frac{1}{r_{12}}$:

$$\frac{1}{\boldsymbol{r_{12}}} = \underbrace{\frac{erfc(\omega \boldsymbol{r_{12}})}{\boldsymbol{r_{12}}}}_{\text{short-range domain}} + \underbrace{\frac{erf(\omega \boldsymbol{r_{12}})}{\boldsymbol{r_{12}}}}_{\text{long-range domain}}. \tag{4.31}$$

where $\boldsymbol{r_{12}} = |\boldsymbol{r_1} - \boldsymbol{r_2}|$ is the inter-electronic distance, $erfc$ is the complementary error function, such that $erfc = 1 - erf$, and erf is the error function. The standard error function is $erf = \frac{2}{\sqrt{x}} \int_0^x exp(-t^2)dt$. Therefore the exchange-correlation functional can broken up as follows:

$$E_{xc} = E_{c,DFT} + E_{x,DFT}^{SR} + E_{x,HF}^{LR} \tag{4.32}$$

where $E_{c,DFT}$ is the DFT correlation functional, $E^{SR}_{x,DFT}$ is the short-range part of the exchange functional and $E^{LR}_{x,HF}$ is the HF exchange at long-range. The LRC-ωPBEh functional that is used in this work has 20% HF exchange in the short-range domain and so the functional becomes,

$$E^{LRC-\omega PBEh}_{xc} = E_{c,PBE} + (0.2E^{SR}_{x,HF} + 0.8E^{SR}_{x,PBE}) + E^{LR}_{x,HF} \tag{4.33}$$

with a default range-separation parameter of $\omega = 0.2a_0^{-1}$. Where $E_{c,PBE}$ is the correlation part and $E_{x,PBE}$ is the exchange part of the PBE functional.[78, 8]

4.2.4 Basis Sets

When describing molecular systems, we are trying to provide a solution to the Schrödinger equation, and these solutions are approximations. Wavefunctions are constructed for the electronic states from molecular orbitals. A linear combination of functions, known as basis functions, are used to represent this wavefunction. Within computational chemistry, these basis functions are combined into a finite set, known as a basis set. There is a choice when determining which basis sets to use within a calculation. Generally, this forces a choice between computational accuracy and computational cost. There are four types of basis set to choose from:

- Plane-wave basis sets: these are very accurate but also very expensive. They are normally only used for crystals.
- Numerical basis sets: less expensive but also less accurate.
- Gaussian basis sets: good general basis sets, reasonably accurate whilst also being reasonably inexpensive. These are used throughout this work.

Within this thesis, Gaussian basis sets are used. One natural suggestion for forming these basis functions is with the Molecular Orbitals as Linear Combination of Atomic Orbitals (LCAO) concept. This creates atomic orbitals centred on each nuclei. Slater-type orbitals use exact hydrogen atomic orbitals to describe the radial component of the functions. However, with Gaussian basis sets, Gaussian functions are used, simplifying the Slater-type approach. Gaussian basis functions are formed as follows:

$$G_{nlm}(r,\theta,\Phi) = N_n \underbrace{r^{n-1}e^{-\alpha r^2}}_{\text{radial part}} \underbrace{Y^m_l(\theta,\Phi)}_{\text{angular part}} \tag{4.34}$$

where N is a normalising constant, n is a natural number that acts as the principle quantum number, $n = 1, 2, ...$, and r is the distance between the electron and the nucleus. It is also important to note that in all basis sets only the radial part of the orbital changes. The angular part of the orbital is

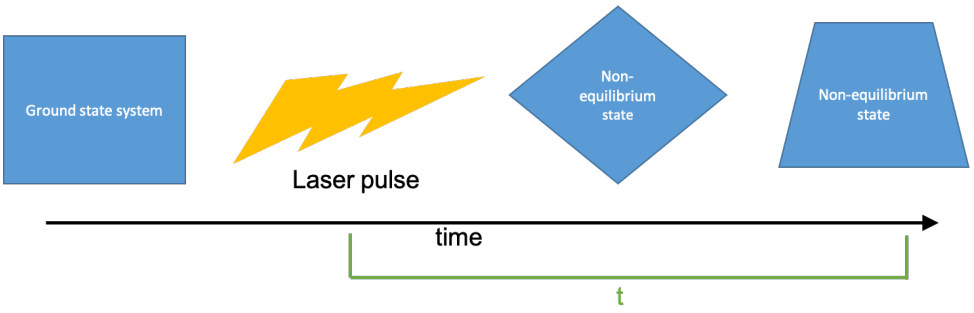

FIGURE 4.1: Schematic representation of time-dependent density functional theory.

described by the spherical harmonic functions in all basis sets.
STO-3G[87] is a simple basis set that centres three Gaussian functions (g_1, g_2 and g_3) on an atom. The shape of these Gaussian functions depends on the atom and are optimised against higher methods and experiment. Then, the electron is allowed to have some population in all three functions, this is described by three coefficients (c_1, c_2, and c_3). Throughout the calculation all three Gaussians and all three coefficients are acted on by the functionals in Equation 4.23. The Gaussians are kept constant throughout the calculation, whilst the coefficients are allowed to change. Therefore, the density on one atom is described by the three coefficients. More complex basis sets use more Gaussians to describe the systems, but, the principle remains the same.

4.2.5 Time-Dependent Density Functional Theory

DFT is a formally exact theory, but is only strictly valid for the electronic ground state of any specific spin multiplicity. To address properties beyond their ground or equilibrium state, we can use TDDFT. The framework of TDDFT is based upon describing the dynamical response of a system, as depicted in Figure 4.1. Here, the system starts in its ground state and is then acted on by an external force, in this case a laser pulse. The system is then observed to see how it behaves over time. To calculate these phenomena we must consider the TDSE. Whilst we have seen that DFT is based upon the Hohenberg-Kohn Theories, TDDFT is built from the Runge-Gross Theorem, which applies a time-dependent perturbation from an external potential.[88]

The Runge-Gross Theorem

The interaction between the electrons and the nuclei is contained within the external potential in DFT. However, in TDDFT this interaction is described by an additional time-dependent potential. The Theorem begins by considering a system that is acted on by an external time-dependent potential, this creates

a TDSE of the form:

$$i\hbar\frac{\partial}{\partial t}\psi_i(\boldsymbol{r},t) = H\Psi(\boldsymbol{r},t) = [T + V(t) + W]\psi_i(\boldsymbol{r},t) \tag{4.35}$$

where T is the kinetic energy operator, W is the electron-electron interaction and $V(t)$ is the time-dependent external potential. The Runge-Gross Theorem uses the above TDSE to show that if two n-electron systems start in the same initial state, and are acted on by two different time-dependent potentials, they will have time-dependent densities that differ by more than a time-dependent constant.[88] In short, the density uniquely determines the external potential at any time.

Time-dependent Kohn-Sham equations

Time-dependent Kohn-Sham equations calculate the density in a similar way by applying a non-interacting system to represent the true system. The time-dependent Kohn-Sham equations can be shown as a continuation of the Runge-Gross equations:

$$i\hbar\frac{\partial}{\partial t}\phi_i(\boldsymbol{r},t) = H\Phi(\boldsymbol{r},t) = [T + V_{ks}(\boldsymbol{r},t) + W]\phi_i(\boldsymbol{r},t). \tag{4.36}$$

Furthermore, the Kohn-Sham potential, $V_{ks}(\boldsymbol{r},t)$ is:

$$V_{ks}(\boldsymbol{r},t) = V_{ext}(\boldsymbol{r},t) + V_H(\boldsymbol{r},t) + f_{xc}(\boldsymbol{r},t) \tag{4.37}$$

where, $V_H(\boldsymbol{r},t)$ is the Coulomb interactions and $f_{xc}(\boldsymbol{r},t)$ is the exchange and correlation functional which, unlike in DFT, is time-dependent. Similarly to DFT the exchange-correlation potential is unknown, it is also crucial for the accuracy of TDDFT. As well as this, due to the addition of the time-dependence in this potential, it appears that new exchange-correlation functionals must be developed in order to complete TDDFT. To rectify this, many applications of TDDFT apply the adiabatic approximation, which approximates the exchange-correlation functional to be local in time. This is valid when the time-dependent potential changes slowly (adiabatically). The approximation assumes that the system at time t_n has no memory of the system at time t_{n-1}, allowing the time-dependent factors to cancel and the exchange-correlation from DFT can be applied.

If this formalism is applied, it corresponds to real-time TDDFT. Here the time-dependent electronic Kohn-Sham system is explicitly propagated [89]. In this case, the time-dependent response makes it possible to visual the motion of the electrons explicitly. This response is then converted into usual frequency dependent spectra using a Fourier transform. While explicitly propagating the Kohn-Sham system has its advantages, it tends to be more computationally expensive. Therefore the preferred option is to work in the frequency domain as discussed below.

Linear-Response Time-Dependent Density Functional Theory

The Kohn-Sham equations provide a way to calculate the time-dependent properties of a system, however, the method is computationally expensive even for small molecules. Often it is not necessary to calculate the full solution for a system as the time-dependent perturbation only causes a small deviation in the system from its initial state, this is valid for most fields in chemistry, and can be approximated to a linear-response. Considering this system, the response to the perturbation can be shown as a Taylor expansion:

$$n(\boldsymbol{r},t) - n_0(\boldsymbol{r},t) = n_1(\boldsymbol{r},t) + n_2(\boldsymbol{r},t) + \ldots, \tag{4.38}$$

where $n_0(\boldsymbol{r},t)$ is the initial density and the subscripts describe the order of the external perturbation. Furthermore, the first-order response can be expressed as:

$$n_1(\boldsymbol{r},t) = \int\int \chi(\boldsymbol{r},t,\boldsymbol{r'},t)V_1(\boldsymbol{r'},t)d^3rdt \tag{4.39}$$

where χ is the density response of the interacting system. Using the density response as shown for the Kohn-Sham system which is for a non-interacting system, and relating to this new density response, χ, it is apparent that the fictitious system can be related to the physically relevant interacting system. Therefore, the effective potential can be derived to map the Kohn-Sham system onto the real system. It is common to perform a Fourier transform to apply the same theory to the frequency domain, this often makes it easier to implement into quantum chemistry codes. When Linear-Response TDDFT (LR-TDDFT) is implemented into codes, it is common to use a set of electron orbital transitions to describe the density response. The Casida formalism uses Kohn-Sham orbitals to describe the external perturbations in terms of excitation and de-excitation processes. The Casida equation is as follows:

$$\begin{pmatrix} \mathbf{A} & \mathbf{B} \\ \mathbf{B}^\dagger & \mathbf{A}^\dagger \end{pmatrix} \begin{pmatrix} X \\ Y \end{pmatrix} = \omega \begin{pmatrix} \mathbf{1} & \mathbf{0} \\ \mathbf{0} & \mathbf{-1} \end{pmatrix} \begin{pmatrix} X \\ Y \end{pmatrix} \tag{4.40}$$

where X describes excitations and Y describes de-excitations, ω is the energy of the excited states, and A and B are defined as follows:

$$A_{ia,jb}(\omega) = \delta_{ij}\delta_{ab}(\epsilon_a - \epsilon_i) + (ia|f_H + f_{xc}|jb) \tag{4.41}$$

$$B_{ia,jb}(\omega) = (ia|f_H + f_{xc}|jb). \tag{4.42}$$

In this case i,j refers to Kohn-Sham orbitals which are occupied in the ground state and a,b refers to the Kohn-Sham orbitals which are populated by excitation. ϵ is the energies of the Kohn-Sham orbitals.[90]

To solve Equation 4.40, the Tamm-Dancoff approximation (TDA)[91] is applied wherein the de-excitation components of the excited state energies

are neglected. Therefore, the B matrix is neglected resulting in:

$$\mathbf{A}X = \omega X. \tag{4.43}$$

This approximation has often been shown to improve the stability of LR-TDDFT but, it also stabilises the excited triplet states, which is important in the context of this work.

Molecular Dynamics

When modelling a molecular system, it is crucial to realise that a static *'snapshot'* of the system, in its equilibrium geometry may not provide a realistic description of a system. It goes without saying that the static description does provide useful information about the system, however, when studying large complex systems its behaviour over time is an important consideration. Each system has a potential energy surface upon which the energy of the system can be described. To build this picture, molecular dynamics (MD) can be used. MD allows the system to interact over a predetermined length of time and the evolution of the system is then shown. As with all computational methods there are limitations. It is to be expected that very large systems cannot be accurately described by MD due to the computational cost involved. A full description of a system propagating through space would require a full quantum description using the Schrödinger equation, as described in Section 4.1. However, due to the $3N$-many scaling problem this is unachievable for large systems. Molecular dynamics was developed to offer a solution to this scaling problem, whereby all the nuclei movement is described classically and evolves under Newtons equations of motions. This often retains sufficient accuracy while also providing a reasonable solution. Classical MD also treats the electrons classically, but replacing them with force-fields whereas *ab initio* MD, which is the focus of the present work, applies a quantum description to the electrons. A DFT calculation is completed at each time-step to calculate the energy and gradient to allow the system to be propagated. Classical MD computes the potentials for the inter-atomic interactions in advance, *ab intio* MD then computes these potentials "on-the-fly", thus reducing the computational expense. The classical MD approach is utilised extensively in research that involves large, complex protein systems.

MD uses step-by-step calculations of the classical equations of motion. They can be described as:

$$m_i \ddot{\mathbf{r}}_i = f_i \tag{4.44}$$

$$f_i = -\frac{\delta}{\delta r_i} U. \tag{4.45}$$

Where m_i is the mass of the particle and r_i is the position. The forces f_i acting on the atoms can be derived from the potential energy $U(r^N)$. Where $r^N = (r_1, r_2, \cdots r_N)$ represents the complete set of $3N$ atomic coordinates.

These $3N$ equations are solved for each particle at each time step. Different algorithms to solve these equations of motion can be applied in MD simulations. However, each algorithm is expected to maintain two properties; firstly, that the equations of motion are reversible in time. Once the trajectory of a system is solved, it should be possible to trace back its dynamics by reversing the sign of the position and momentum. Secondly, the spacial derivative of the potential determines the motion of the particles, that is to say, if the same system is acted on by two different potentials it will produce two different trajectories.

The potential energy that is used to describe the molecule/system is crucial to the accuracy of the calculations. In the case of the MD used in this work, the energy and the gradient is calculated using DFT for each timestep. Within MD thermostats or barostats can be used to control temperature or pressure, respectively. Thermostats control the temperature through the kinetic energy of the nuclei, whilst barostats control pressure by adjusting the volume of the calculated system. Throughout this work, single molecules are used and so only thermostats are needed.

One final consideration of the MD framework is the ergodicity principle. Simply put, this principle states that a dynamical system will eventually visit all parts, or potential, of the system. Quantum mechanics (QM) describes it as the time average being equal to the ensemble average. Whereby any observable, O, can be described by $\langle O \rangle = \langle \psi | \hat{O} | \psi \rangle$. The microcanonical ensemble is employed to describe all of the possible states of a mechanical system with a specified energy. This can also be known as the NVE ensemble, as the constraints for the ensemble are the number of particles, N, the volume, V, and the energy of the system, E, must all be kept constant. The average O over all space can be therefore expressed as:

$$\langle O \rangle = \frac{\int O(q,p) e^{-E/k_B T} dq^N dp^N}{\int e^{-E/k_B T} dq^N dp^N} \tag{4.46}$$

where, q and p are the coordinates of the momentum and the N-particle system, respectively. However, practically the average described here cannot be calculated as not all microstates are known. The ergodicity principle can be employed here to describe the average observable as

$$\langle O \rangle = \lim_{t \to \infty} \frac{1}{t} \int_0^t O dt. \tag{4.47}$$

Knowing the ergodicity principle, we can now calculate this average observable by either time averaging a system, or averaging the ensemble. Furthermore, this has a practical application, within the limit of sufficiently long dynamics, the integral can be replaced by a sum. Thus, the observable average can be computed by the summation of its value at each time point and then dividing this value by the length of the simulation. When applying this reasoning to the work of this thesis, it is important to consider if the MD run were sufficiently long enough to ensure all parts of the system, or potential,

are visited.

4.2.6 Polarizable Continuum Model

The polarizable continuum model (PCM) is commonly used to describe the effect of a solvent environment, implicitly, i.e. without the need to explicitly include many molecules increasing the computational expense of the simulations. In this case, the solvent is modelled as a continuum, which can be polarized by the solvent rather than individual molecules. There are two main types of PCMs have been popularly used: the dielectric PCM (D-PCM) in which the continuum is polarizable and the conductor-like PCM (C-PCM) in which the continuum is conductor-like similar to COSMO solvation model.[92]

The molecular free of solvation is computed as the sum of three terms:

$$G_{sol} = G_{es} + G_{dr} + G_{cav} \tag{4.48}$$

G_{es} = electrostatic
G_{dr} = dispersion-repulsion
G_{cav} = cavitation

These are add accounted for in an approximate manner using a PCM. Further details can be found in ref.[93].

Chapter 5

Refining the Performance of TADF using Rotaxanes

The work presented in this chapter has been published in Angewandte Chemie in 2021.[6]

5.1 Introduction

An extensive research effort, both experimental[94, 4, 95] and theoretical,[2, 96] has led to a detailed understanding of the mechanism of triplet harvesting for TADF. In D-A systems, we require a near 90° angle between D-A units but also conformational freedom around this bond to activate the spin-vibronic coupling mechanism.[96] The importance of the vibrational freedom of the D-A bond means that enforcing rigidity upon a system will be counterproductive, indeed, it tends to yield room temperature phosphorescence instead, *i.e.* the rISC rate is quenched.[46] However, too much flexibility in conformation can cause broadening of the emission of these molecules and compromise the colour purity of these emitters. Molecular flexibility will also increase non-radiative decay. In addition, in D-A TADF emitters, surprisingly subtle excited state conformational dynamics plays a key role in controlling the excited state dynamics and, therefore, TADF properties.[8] It is clear that controlling these dynamics is important. Designing a molecule with some vibrational flexibility whilst maintaining a high colour purity is the focus of this work. Previous publications have focused on enhancing steric hindrance[97, 98] or non-covalent interactions[99, 100] to alter the D-A bond preferences.[6]

Architectural control of emitters is undoubtedly valuable when attempting to achieve efficient TADF. This control has been exploited to achieve high photoluminescent quantum yields, Φ_{PL}, and, minimise the energy gap between the first singlet excited state and the first triplet excited state has been the focus of significant research.[99, 100, 101, 102, 103, 97, 98] Using molecular structure for fine control of TADF emitters has been a research focus for many groups but previous work has used covalent modifications or non-covalent interactions.[6] Li *et al.*[97] and Park *et al.*[98] use substitution on the emitter to increase steric hindrance and therefore fine-tune the TADF properties.

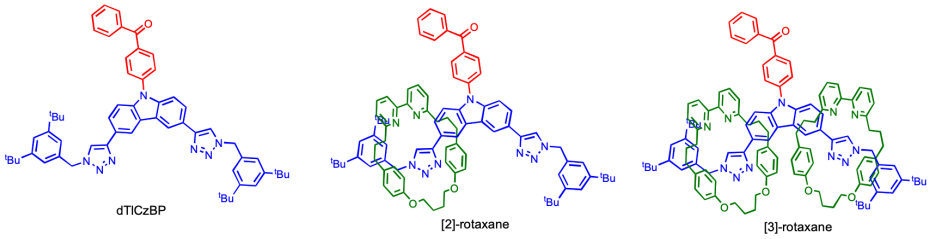

FIGURE 5.1: Structures of the molecules, dTlCzBP, [2]-rotaxane, and [3]-rotaxane, investigated in this work. The emitters will be known as **1**, **1**⊂**2** and **1**⊂$\mathbf{2}_2$ for the dTlCzBP system, [2]rotaxane, and [3]rotaxane, respectively.

Dos Santos *et al.*[100] use a non-covalent approach, whereby, the emitters are stabilised by intramolecular hydrogen bonding. In this work, performed in collaboration with the Goldup and Zysman-Colman groups, we used mechanically interlocked molecules (MIMs), and the crowded, flexible environment created by the mechanical bond to fine-tune the emission properties. A mechanical bond is a bond that is formed as a consequence of topology. In this work rotaxanes are used, in their most simple form a rotaxane is a dumbbell structure with a ring threaded on; the ring cannot come off due to the shape of the ends of the dumbbell structure. Rotaxanes are described as $[n]$rotaxane, whereby $[n]$ is the number of components of the system. Due to the increase in effective methodologies for synthesising MIM's, they have also become the focus of research in areas beyond TADF applications, such as, sensors[104, 105, 106] and catalysis[107, 108, 109].[6]

This work reports a series of carbazole-benzophenone based emitters; two of which are MIMs, as shown in Figure 5.1. The design of the interlocked [2]rotaxane, and [3]rotaxane, was based on the system by Zysman-Colman *et al.*, who previously demonstrated the TADF properties of the carbazole-benzophenone system.[110, 111] The emitters will be known as **1**, **1**⊂**2** and **1**⊂$\mathbf{2}_2$ for the dTlCzBP system, [2]rotaxane, and [3]rotaxane, respectively. These systems have previously been reported by Rajamalli *et al.* to synthesise a gel-based TADF emitter.[112]

Furthermore, this work demonstrates that the macrocycles that are threaded on the emitting core can be used to fine-tune the photophysical properties of a TADF-active axle in both solution and thin films.[6] All three structures in Figure 5.1 are TADF emitters, exhibiting a small ΔE_{ST} and observed delayed fluorescence. The structures show a high Φ_{PL}, up to 60%, and crucially, the Φ_{PL} increases whilst ΔE_{ST} decreases as more macrocycles are added to the dumbbell structure. [6] All of the theoretical studies were completed by the Author. However, this study was undertaken in collaboration with The Goldup Group at the University of Southampton who completed the synthesis and The Zysman-Colman Group at St. Andrews University, who undertook all of the photophysical measurements.[6]

5.2 Computational Details

The crystal structures were used to build the models of **1**, **1**⊂**2**, and **1**⊂**2**$_2$ and were subsequently optimised. For **1**⊂**2** and **1**⊂**2**$_2$ the macrocycles were positioned and rotated at multiple different points on the axle to ensure that the lowest energy conformer was obtained. Ground state optimisations were calculated using DFT within the Q-Chem quantum chemistry package,[113] within the approximation of the PBE0 functional[78, 114] with the Def2-SVP[115] basis set. The excited state calculations were performed using LR-TDDFT within the TDA [91] using the same functional and basis set.

The *ab initio* MD were performed using the TeraChem[116, 117, 118] software using DFT in the electronic ground state, and LR-TDDFT in the excited S_1 state. The PBE0 functional[78, 114] and Def2-SVP [115] basis set was used throughout. The trajectory was propagated using the velocity Verlet algorithm and a finite temperature of 300 K. After an initial equilibration period of 5 ps starting from the ground state or S_1 state optimised geometry, the MD were run for a further 10 ps from which all properties were calculated. All calculations included the solvent environment which was described using a conductor-like polarisable continuum model using the dielectric constant of toluene. In the case of this work, it is unlikely that every part of the system was modelled as the MD was run for 10 ps for each system. However, the frequency of torsional modes are about 10-50 cm^{-1}, this corresponds to 3 ps - 500 fs. Thus, even the lowest frequency modes have undergone 3 oscillations in the simulation. This is an appropriate approximation for this study.

5.3 Results

5.3.1 Ground State Properties and Frontier Orbitals.

The first step in understanding the properties of the three systems, **1**, **1**⊂**2** and **1**⊂**2**$_2$, was to establish their ground state properties. DFT was performed to calculate electrochemical data. The lowest energy conformers of the ground state (S_0) each structure were calculated using DFT(PBE0). The DFT calculated energy levels for the HOMO and LUMO can be seen in Table 5.1, whilst the experimentally observed energy levels can be seen in Table 5.2. It is obvious that the energy levels reported by the theoretical studies reproduce not only the trend of the results of the electrochemical study by Rajamalli *et al.*,[6] but also provide reasonable values for each system. In both studies, the biggest change can be seen by the addition of one macrocycle, when moving from **1** to **1**⊂**2** the energy of both the HOMO and the LUMO decreases. When the second macrocycle is added, forming **1**⊂**2**$_2$, there is a smaller change in the HOMO energies, however, the LUMO energy can be observed as staying the same in both the theoretical and experimental study. Thus, the frontier orbitals show a more notable change in energy level when one ring is added. However an additional ring after this makes little difference to the HOMO

and no difference to the LUMO energy level.

	1	**1⊂2**	**1⊂2_2**
HOMO/eV	-5.41	-5.14	-5.09
LUMO/eV	-1.71	-1.65	-1.65
S_1 (f)/eV	3.17 (0.316)	3.00 (0.272)	2.91 (0.271)
T_1/eV	2.83	2.70	2.63
T_2/eV	3.11	3.10	3.10

TABLE 5.1: Electronic properties of axle **1**, **1⊂2** and **1⊂2_2** at the ground state geometry, calculated using DFT(PBE0)/Def2-SVP.

	1	**1⊂2**	**1⊂2_2**
HOMO/eV	-5.62	-5.47	-5.41
LUMO/eV	-2.53	-2.52	-2.52

TABLE 5.2: Electronic properties of axle **1**, **1⊂2** and **1⊂2_2** determined by Rajamalli *et al.*.[6]

Furthermore, when considering the frontier orbitals it is helpful to illustrate the shape and localisation of the orbitals. The HOMO and LUMO for each system are shown are Figure 5.2. It is clear that the two orbitals are consistently localised to separate parts of the molecules. The HOMO is centred on the carbazole (Cz) donor part of the molecule. There is also a contribution to the HOMO from both of the triazole (Tz) units in all three structures. Conversely, the LUMO can be seen to be localised on the benzophenone (BP) acceptor unit. The addition of one or two rings, on **1⊂2** and **1⊂2_2**, respectively, causes little to no change to the shape of the frontier orbitals.

5.3.2 Photophysical Properties

TDDFT was used to investigate the electronic structure of all three emitters, in both the ground and excited states. TDDFT at the ground state corresponds to absorption spectrum and TDDFT at excited state structures correspond to emission spectrum. In the ground state geometry of **1**, two triplet states were found to be lower in energy than the S_1, both triplet states exhibit a mixed ^{3}CT and acceptor based ^{3}LE character, Table 5.1. Whereas, for **1⊂2** and **1⊂2_2** the acceptor based ^{3}LE appears above the S_1 state. These results are consistent with the structured phosphorescence emission spectra as recorded experimentally by Rajamalli *et al.*[6] It has been reported that high performance TADF emitters display this ^{3}LE state as it can allow a pathway for efficient coupling between the singlet and triplet charge transfer states.[5]

Upon investigation of the excited state geometries, the TDDFT calculations show that the lowest excited singlet and triplet states are of pure CT

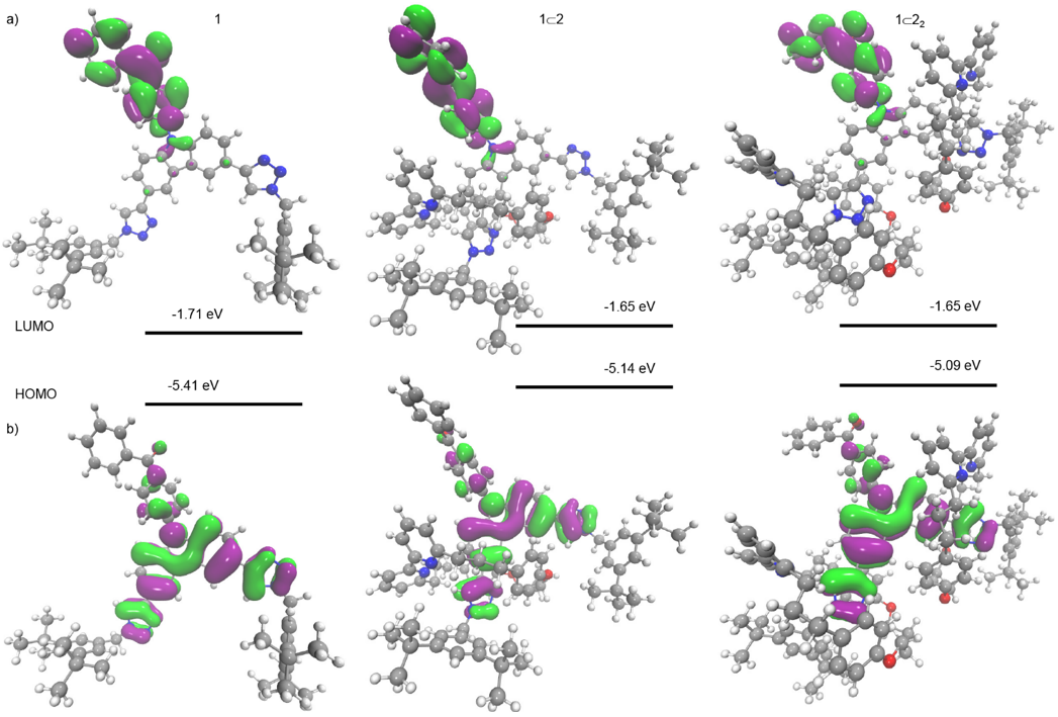

FIGURE 5.2: The LUMO (top) and HOMO (bottom) orbitals for **1**, **1**⊂**2** and **1**⊂**2**$_2$ at the ground state geometry, computed using DFT(PBE0)/ Def2SVP.[6]

	1	**1**⊂**2**	**1**⊂**2**$_2$
S_1 (f)/eV	2.33 (0.000)	2.06 (0.000)	1.99 (0.000)
T_1/eV	2.32	2.06	1.99
T_2/eV	2.74	2.78	2.79

TABLE 5.3: Calculated electronic properties of axle **1**, **1**⊂**2** and **1**⊂**2**$_2$ at the excited state (S_1) geometry.

character whereas, the ^{3}LE state lies ~0.3 eV higher in energy. It should be noted that there is an inherent challenge with TDDFT to calculate the absolute energies of CT states; therefore, this energy gap is likely to be an overestimated and this challenge is explained in more detail in Chapter 6.[8] Furthermore, the oscillator strengths, (f), of the S_1-S_0 transitions for the ground state geometry of **1**, **1**⊂**2** and **1**⊂**2**$_2$ were 0.316, 0.272 and 0.271, respectively. However, this value fell to 0.000 for all three emitters in the excited state geometry. In the ground state, the D and A are not exactly perpendicular to one another, therefore, there is some HOMO-LUMO mixing that gives rise to an oscillator strength. However, in the excited state, the D and A parts of the system have a more perpendicular arrangement. Furthermore, this completely separates the HOMO and LUMO and consequently the oscillator strength goes to zero.

Finally, as expected, this indicates that the photophysical properties of

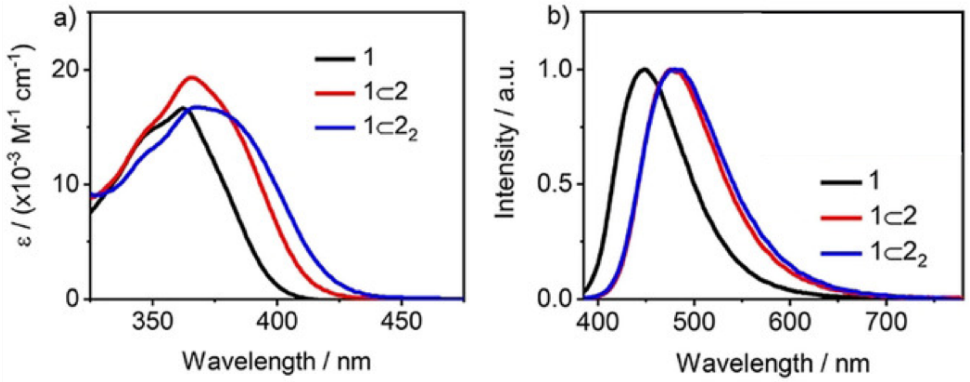

FIGURE 5.3: a) Absorption and b) PL spectra of **1**, **1**⊂**2** and **1**⊂**2**$_2$ in PhMe (λ_{exc}=340 nm, 10^5M) as calculated by Rajamalli *et al.*[6]

each emitter are influenced by the molecular flexibility. This is consistent with a number of TADF emitters with the D-A framework whereby, distortion away from a perfectly perpendicular arrangement gives rise to some HOMO-LUMO overlap, and thus some oscillator strength.

The three structures can be seen to be increasingly red-shifted in the CT absorption maximum, with the trend λ_{abs} **1** > **1**⊂**2** > **1**⊂**2**$_2$. The experimental results reproduce this trend as shown in Figure 5.3a and b, the absorption and photoluminescence (PL) spectra respectively. A more noticable shift can be seen in the emission maxima, λ_{PL}, on the PL spectra, from 449 nm to 477 nm and 484 nm for**1**, **1**⊂**2** and **1**⊂**2**$_2$, respectively.[6] The theoretical calculations can be further scrutinised to understand the origin of the red-shifting. The addition of the ring induces a H-bond between the encircled triazole C-H and the N donors of the bipyridine in the ring; this in turn destabilises the HOMO. Conversely, the LUMO energy levels feel no influence of the ring, therefore, the energy level of the LUMO does not change. The addition of the ring in **1**⊂**2** accounts for the added donation of electron density from the triazole units into the Cz core. There is a remarkable difference in the HOMO energy levels in **1** and **1**⊂**2** (0.27 eV), this is due to a complete lack of interaction in structure **1**; due to there being no macrocycle present. Whereas, there is a less pronounced difference between **1**⊂**2** and **1**⊂**2**$_2$. Therefore the addition of one ring has a remarkable effect (0.27 eV), whereas the addition of the second ring has a lesser effect (0.06 eV).

An experimental study of **1**, **1**⊂**2** and **1**⊂**2**$_2$ by Rajamalli *et al.*[6] showed that the encircled triazole protons formed CN$\cdots$H hydrogen bonds to the bipyridine N atoms. They performed a solid-state study that revealed a network of weak C-H$\cdots$ π, C-H$\cdots$N and C-H$\cdots$O contacts between the macrocycle and the TADF-active axel, as shown in Figure 5.4. This was obtained from diffraction by Rajamalli *et al.* and shows the hydrogen contacts in yellow.[6]

Up until this point, all of the theoretical studies have described a static picture of the structures. In reality, all structures move in nature, therefore, to

develop an understanding of the dynamical picture MD was utilised.

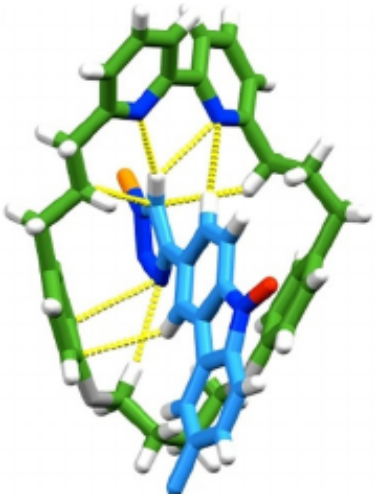

FIGURE 5.4: Solid state structure of **1**⊂**2** with hydrogen contacts shown in yellow. Structure obtained by diffraction by Rajamalli *et al.* [6]

5.3.3 Molecular Dynamics

The dynamics of a chemical system play a pivotal role in its emission spectra. An *ab initio* MD study can be used to model this dynamic behaviour. In this case, a 10 ps study was conducted for the electronic ground (S_0) and emissive excited (S_1) states. DFT(PBE0) analysis was performed at the lowest energy (optimised) conformer of each structure. Firstly, we will focus on the results of the electronic ground state study, bond lengths and angles in this S_0 state were remarkably similar for all three emitters. The behaviour of the D-A bond length, the dihedral angle between the Cz donor and, the phenylene of the BP acceptor and both $C_{Cz} - C_{Tz}$ bond distances (where Cz is carbazole and Tz is triazole) as shown in Figure 5.5. The Cz-BP (D-A) bond was found to range between 1.403 Å and 1.406 Å with minima at ~40° and ~140° as shown in Figure 5.5 a, d and g. These two minima can be seen on the potential energy scan, Figure 5.6, of the Cz-BP dihedral with a relatively low barrier to conformational exchange (~0.1 eV). However, it is clear that the addition of the macrocyclic ring increases this barrier to rotation, thus, makes it more difficult for the structure to swap between the two conformers. Furthermore, when considering probability distribution of each conformer over the PES, as shown in Figure 5.5 b, e and h it is clear that the shape of the red plot matches the shape of the PES, shown in Figure 5.6. The PES shows the lowest energy conformer for emitter **1** has a D-A dihedral around 40°, whereas, for both rotaxanes that have one (or two) encircling macrocycles, the lowest energy conformer flips to be the conformation with a D-A dihedral angle of ~140°.

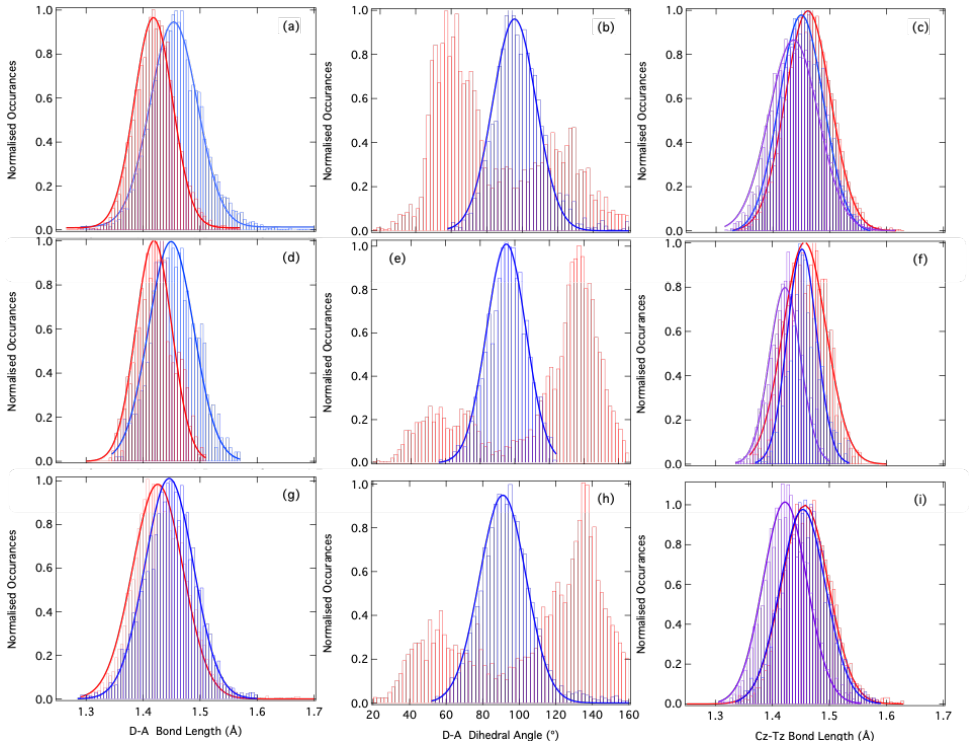

FIGURE 5.5: The distribution of the D-A bond distance, the dihedral angle between the D and A groups and carbozole triazine aryl-aryl bond for (a-c) **1**, (d-f) **1**⊂**2** and (g-i) **1**⊂$\mathbf{2}_2$ for the ground (red) and excited state (blue, purple) geometries.

When comparing the two rotaxane structures, **1**⊂**2** and **1**⊂$\mathbf{2}_2$, an interesting arrangement preference can be seen. The Tz units of the **1**⊂**2** adopt a syn-anti arrangement, whilst those of the **1**⊂$\mathbf{2}_2$ adopt a syn-syn orientation, where the syn oriented unit is that which is encircled by the macrocycle. This is due to the syn conformation of Tz units minimising the steric repulsion between an encircling macrocycle and the Cz unit. The syn-anti preference was also seen for **1**, this conformation reduced the repulsion between the dipoles that are associated with the Tz rings. Similarly to the D-A bond length, the average $C_{Cz} - C_{Tl}$ bond length, of 1.46 Å, and distribution of said bond length remains unaffected by the addition of the macrocycle rings.

Upon investigation of the excited S_1 state, a number of changes became apparent. As is commonly observed in D-A TADF emitters, the D-A bond (Cz-BP) was weakened upon excitation and consequently lengthened to 1.44 Å. The Cz-BP dihedral angle was found to be ~90° at its lowest energy excited state conformation.[119] Conversely, in the excited state structures of both **1** and **1**⊂**2** only one of the Cz-Tz bonds contracted (Δ = 0.022 Å and 0.029 Å respectively), whilst the other remained mostly unchanged, therefore, an asymmetry in the electron density was created on the donor. In the case of **1**⊂$\mathbf{2}_2$ both of the Cz-Tz bonds were seen to contract but remained similar (1.442 Å and 1.447 Å). In the excited state, the Tz moieties donate

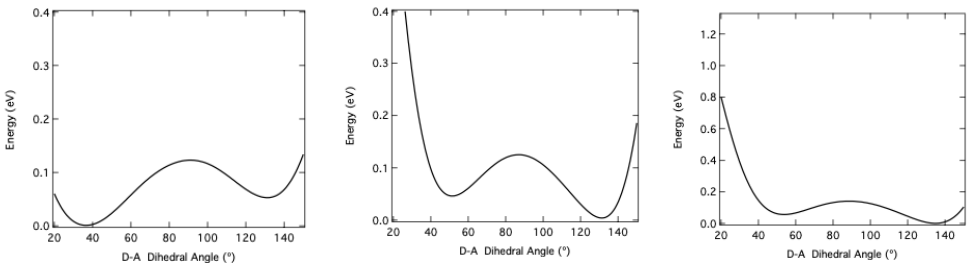

FIGURE 5.6: Ground state potential energy scans for **1** (left), **1**⊂**2** (middle), and **1**⊂$\mathbf{2}_2$(*right*).

an increased electron density to the Cz core; physically this can be seen as a contraction in the Cz-Tz dihedral angle in the S_1 state compared to the S_0 state.

However, in the excited state, the interlocked macrocycles can be seen to cause a subtle change in the Cz-BP dihedral angle. This is indicated by a mean and standard deviation of 89 ± 17°, 90 ± 14° and 90 ± 11° for **1**, **1**⊂**2** and **1**⊂$\mathbf{2}_2$, respectively. Despite the reduction in the standard deviation between each system being subtle, it can be said that as the macrocycles are added the standard deviation is seen to decrease. This is evidence of the encircling macrocycles exerting fine conformational control on the excited state dynamics, thus, causing a slight rigidification of this conformational mode. Furthermore, this effect can also be seen in the Cz-Tz dihedral angles with values of 3 ± 16° for **1**, 2 ± 11° (encircled) and 5 ± 17° (free) for **1**⊂**2** and 2 ± 6° for **1**⊂$\mathbf{2}_2$. Here, there are two dihedral angles reported for **1**⊂**2** and only the one encircled by the macrocycle is altered relative to the axle alone.[6]

The ΔE_{ST} and the average oscillator strength, $S_1(f)$, for the $S_1 \rightarrow S_0$ transition can be used to effectively describe the TADF performance of a system. Therefore, it follows that measuring these values for the excited state *ab initio* MD of each emitter will provide a good representation of the influence of the dynamic differences enforced by the mechanical bond on the TADF efficiency of each system. The trend in the value of ΔE_{ST} is **1** > **1**⊂**2** > **1**⊂$\mathbf{2}_2$ this can be correlated to the trend in the mean Cz-BP dihedral angles, as seen previously. As the dihedral angle becomes closer to 90°, it is expected that the ΔE_{ST} will reduce, thus explaining the trend seen here. The narrowing of the distribution of the dihedral angles around 90°, as seen in Figure 5.5 (b), (e) and (h), for the Cz-BP bond is expected to decrease the overall oscillator strength for the $S_1 \rightarrow S_0$ transition. Furthermore, the results of the *ab initio* MD study reproduces this trend with average values of $S_1(f)$ of 0.0260, 0.0095 and 0.0088 for **1**, **1**⊂**2** and **1**⊂$\mathbf{2}_2$, respectively. Moreover, these $S_1(f)$ values are in excellent agreement with the experimentally calculated τ_p values from the photophysical measurements by Rajamalli *et al.*[6] As can be seen in Figure 5.5, the distribution of the Cz-BP (D-A) and the Cz-Tz dihedral angles show a narrower distribution for the structures with the encircling macrocycles. As the macrocycles are added, they rigidify the molecular framework thus

decreasing the rate of non-radiative decay, concequently leading to a higher quantum yield. Furthermore, remaining consistent with the **1** > **1**⊂**2** > **1**⊂**2**$_2$ trend observed.

5.3.4 Conclusions

This work has shown the potential of MIMs, namely rotaxanes, to control the electrochemical and photophysical properties via the mechanical bond. The DFT and *ab initio* MD studies have shown that the weak interactions between the bipyridine N donors and the C-H of the triazole provide the fine molecular control that is desired to improve TADF emitters. Thus, controlling the rigidity of the structure, therefore, influencing the HOMO energy. This can facilitate the shifting of the emission energy, creating a pathway to improve the emission colour. The work shows that the conformation of the TADF-active axle is altered by the mechanical bond in both the ground and excited states. In this work, the mechanical bond decreases the energy gap between the two CT states and decreases the oscillator strength of the S_1 state. These are two crucial properties to consider when building TADF emitters, hence, showing the potential of this mechanism to be exploited to create TADF emitters with desirable properties. Ultimately, this provides an opportunity to improve the efficiency of OLED devices. Overall, we see that the mechanical bond causes a large increase in the photoluminescence quantum yields, an advantageous quality for light emitting structures. The theoretical methods used throughout this study have provided an accurate reproduction of results which are concurrent with those seen experimentally. Furthermore, the *ab initio* MD study has provided effective insight into the dynamic nature of these complex structures. Thus, highlighting the usefulness of theoretical studies to aid the engineering of future TADF emitting MIMs, particularly when the steric control is the focus of the work. Considering the recent explosion of interest into TADF emitters, and the proven ability to engineer the molecules that have fine-tuned properties due to the mechanical bond, this work provides a realistic and exciting approach to improve device efficiency. Despite the rotaxanes displaying a clear control of the TADF properties within this work, it was seen that the ring did not sit over the D-A bond, the control of which is thought to be the ideal for engineering efficient TADF emitters. Future work should consider the placement of this ring. Another way to expand this study is to investigate other similar systems that use this mechanical bond to control the TADF properties of the emitter. Due to the recent advances in computational chemistry, building large systems and predicting their behaviour has become a reality, consequently making it an exceptional tool to predict future targets.

Chapter 6

Improving TDDFT for TADF using Tuned Range Separated Hybrid Functionals

6.1 Introduction

The ability to accurately model excited state properties of systems is undeniably useful when developing new technology. If a computational study can provide a realistic description of the properties of prospective emitters, it can be used as a tool to not only shed light on the fundamental properties of new systems, but it can also be utilised to provide predictions for future targets. Thus, the description of the excited states of molecules that display favourable emission characteristics is at the forefront of current attempts to understand and improve functional organic materials.

A large number of computational methods exist and have been applied to study functional organic molecules including coupled cluster [120, 121] and configuration interaction [122, 123] based approaches. However, owing to unfavourable computational scaling, it is challenging to widely apply these methods to achieve broad understanding and design of new molecules. Consequently, to simulate the properties of these complexes, DFT and TDDFT[124] play a central role due to their efficiency for simulating ground- and excited-state properties of larger molecules.

However, in many cases for organic electronics especially TADF, CT states play a crucial role. Consequently, simulating these within the framework of TDDFT is at odds with the widely document limitation of this method, *i.e.* simulating CT excitations [81]. In the context of TADF, Huang *et al.* [125] addressed these limitations by choosing different exchange-correlation functionals to different molecules depending on the strength of CT and the percentage of exact exchange required. This percentage was determined using a CT index that the authors defined following an analysis of the HOMO and LUMO orbitals. However, the main drawback is the number of different functionals used, 10 in total. As each functional does not only vary by the fraction of exact exchange, this approach does not necessarily yield a consistent description of the excited state properties.

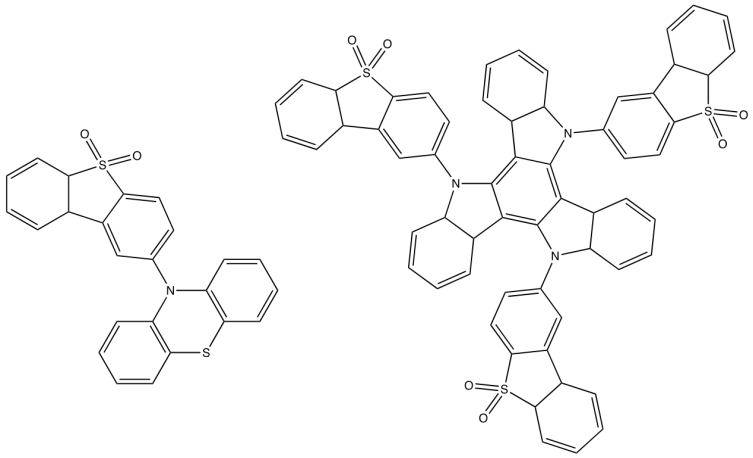

FIGURE 6.1: Schematic representation of the two systems studied. Left; PTZ-DBTO$_2$ and right: TAT-3DBTO$_2$.[7]

The physical reason for TDDFT being unable to accurately describe CT states is due to the (semi)-local nature of many standard exchange-correlation functionals [81, 126]. Consequently, for describing CT states, hybrid functional incorporating a large fraction of non-local HF exchange [127] or range-separated functionals, which attempt to reproduce the 1/r decay of the exchange and correlation potential by incorporating a fraction of HF exchange which depends upon the inter-electron distance [128], are increasingly popular choices. For the latter, there is a sub-class of so-called non-empirically tuned approaches in which the range-separated functional is altered for each molecule so that it fulfils certain conditions of an exact *xc* functional. The most popular of these is the Koopman's OT approach (OT) [85], described below. Recently, Lin and Van Voorhis [129] have proposed an alternative methodology focused upon incorporating electron-hole interactions present in excited states, which they named triplet tuning (TT). The authors reported good performance for the TT functional for a set of 100 molecules, including key observables such as singlet and triplet energies and the ionisation potentials.

In this work we initially examine the performance of the OT and TT methods using two TADF molecules. The first TADF molecule is PTZ-DBTO2, it comprises of a phenothiazine donor and a dibenzothiophene-S,S-dioxide acceptor; a D-A molecule. The second is a D-A$_3$ molecule, TAT-3DBTO$_2$, developed by Dos Santos *et al.*,[130] is composed of three DBTO$_2$ acceptors are joined to a rigid triazatruxene central donor. Previous work has studied the ability of the OT method to predict the energetics of TADF emitters [131], but the demonstrated role of nuclear dynamics on TADF properties [2] means that here we focus on the role of geometry dependence of each method especially relevant in the context of developing size-consistent potential energy surfaces. From this we establish that the OT method is the most reliable, and

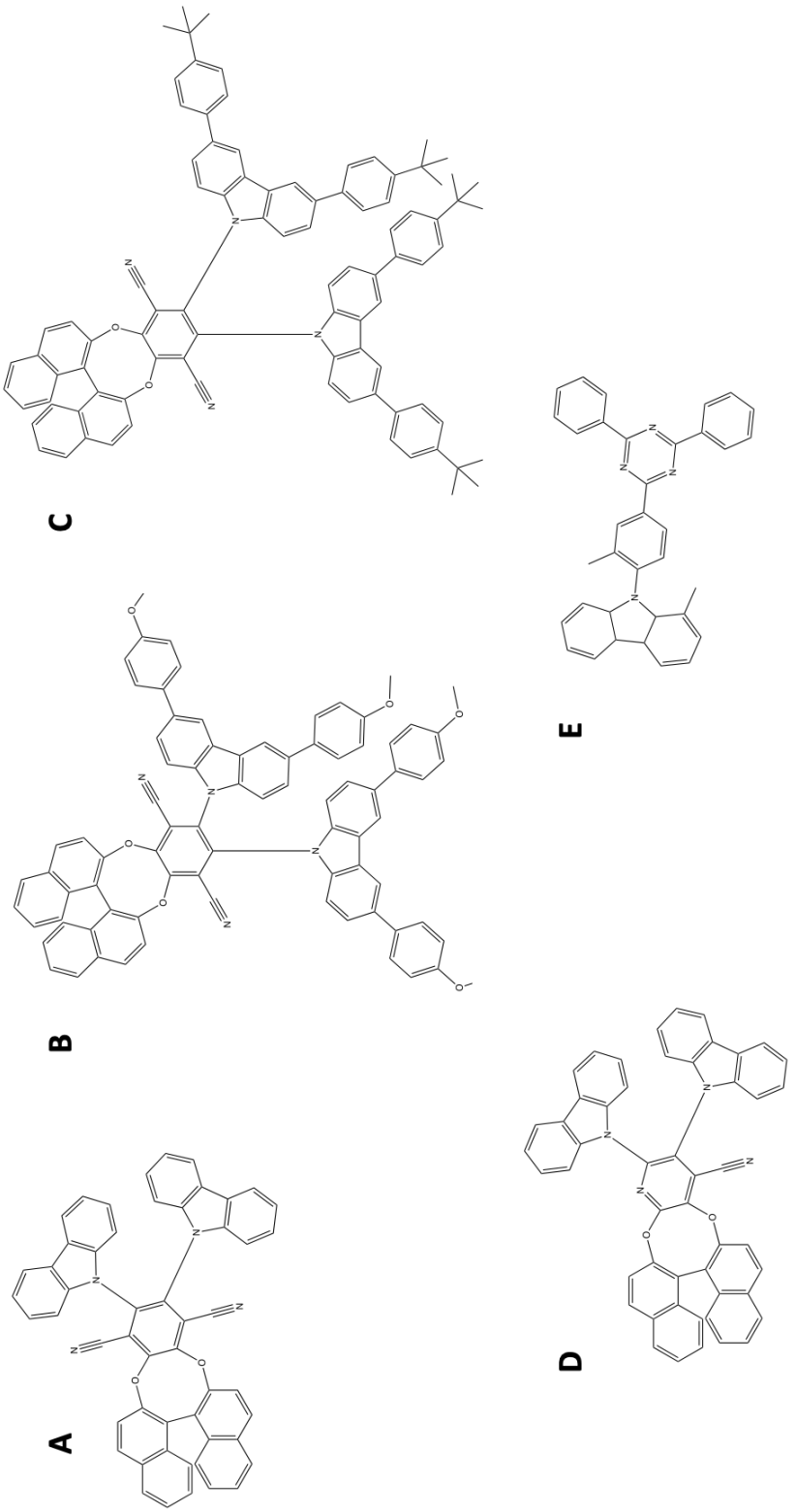

FIGURE 6.2: The CP-TADF emitters **A, B, C, D** and **E** investigated in this work.

therefore apply this OT method to a variety of CP-TADF emitters, with a particular focus of establishing how the OT affects properties other than excited state energies, such as predicted light dissymetry. This was applied to four CP-TADF emitters, Figure 6.2a, b, c and d, the emitters are based upon the work by Feuillastre *et al.*,[132] who reported the CP-TADF emitter, built from a traditional TADF D-A emitter with a chiral pertubation. Finally, an axially chiral CP-TADF emitter that was synthesised by the Futcher group was analysed. In chemistry, axial chirality is a special case of chirality in which a molecule contains two pairs of chemical groups in a non-planar arrangement about an axis of chirality so that the molecule is not superimposable on its mirror image. In contrast to the chiral perturbation approach, this emitter has the chiral appendage built closer to the TADF centre.

6.2 Theory

It is widely accepted that standard approximations to exchange-correlation functionals do not provide a good description of excited states such as CT states.[81, 133] This is due to the semi-local nature of TDDFT. A hybrid functional such as B3LYP[134, 135] has 20% HF exchange, whilst the other 80% is DFT. However, DFT is a short range theory, whereby the local interactions are well described. Whereas, the HF exchange more accurately describes the non-local effects. Another method that has been developed to improve the description of these electronic states is long-range corrected DFT, these provide a bespoke range-separated functional chosen for each molecule resulting in an exact exchange functional.

6.2.1 Optimal Tuning Approach

Koopmans theorem was published in 1934, the work showed that in HF theory the first ionisation energy is equal to the negative of the HOMO energy.[136] OT requires that DFT obeys Koopmans theorem within the limit of the exchange correlation functional:

$$IP^{(0)} + \epsilon^{(0)}_{HOMO} = 0. \tag{6.1}$$

The same approach can be applied to the anionic system, thus,

$$IP^{(-)} + \epsilon^{(-)}_{HOMO} = 0. \tag{6.2}$$

Where, $\epsilon^{(-)}_{HOMO}$ and $IP^{(-)}$ are the HOMO energy and the IP of the anion, respectively. This can be written as

$$IP^{(-)} = E^{(0)} - E^{(-)} = -EA^{(0)} \tag{6.3}$$

where $EA^{(0)}$ is the electron affinity of the neutral form. Consequently, Equation 6.2 can be rewritten as

$$-EA^{(0)} + \epsilon^{(-)}_{HOMO} = 0. \tag{6.4}$$

With that said it is clear that the OT approach can apply an optimisation of the energy difference between the IP and the HOMO energy and the EA and the HOMO energy of the anion to mimic the exact exchange correlation functional. Therefore the optimal range-separation parameter, ω ($\omega^*_{J^2_{OT}}$), is the value that minimises the OT function $J^2_{OT}(\omega)$.[7]

$$J^2_{OT}(\omega) = J^2_{IP}(\omega) + J^2_{EA}(\omega) \tag{6.5}$$

where

$$J^2_{IP}(\omega) = [IP^{(0)} + \epsilon^{(0)}_{HOMO}]^2 \tag{6.6}$$

and

$$J^2_{EA}(\omega) = [-EA^{(0)} + \epsilon^{(-)}_{HOMO}]^2. \tag{6.7}$$

6.2.2 Triplet Tuning Approach

The final long-range corrected DFT functional that will be discussed in this thesis is the TT approach, first proposed by Lin and Van Voorhis in 2019.[137] As the name suggests, the method uses the energy first excited triplet state T_1, in fact, there are multiple ways that this T_1 state can be calculated. In this case the approach calculates the T_1 energy using unrestricted DFT (uDFT) and TDDFT.

Firstly, calculating the triplet excitation energy using DFT uses a generalisation of the Kohn-Sham functional, as described above. Within Kohn-Sham DFT the ground state energy is calculated from the ground state density, therefore, it is possible to use the KS functional to calculate the GS energy of any given symmetry provided that the density has been constrained to the the same symmetry.[138] Practically, when considering a closed-shell molecule, as most organic molecules are, the true ground state is a spin restricted singlet, S_0, in which case $M_S = 0$. When evaluating the T_1 energy in this case it must be the lowest state with $M_S = \pm 1$. In order for the T_1 state to be accessed in a closed shell system an electron must be promoted from the HOMO to the LUMO and flipping the spin. Therefore, the S_0 can be best evaluated using restricted DFT (rDFT), as it is a closed shell system, and setting $M_S = 0$. To calculate the open shell T_1 system uDFT can be used with $M_S = \pm 1$.[139] Finally, the triplet excitation energy, E_T, can be evaluated exactly, Equation 6.8, as the difference between these two calculated energy levels, provided that the exact functional is used.

$$E_T^{\Delta SCF} = E_{T_1}^{uDFT} - E_{S_0}^{rDFT}. \tag{6.8}$$

Another way to calculate the T_1 energy is to use linear-response TDDFT, ensuring again that the exact exchange functional is used. Therefore, E_T can be found using:[139]

$$E_T^{TDDFT} = E_{T_1}^{TDDFT} - E_{S_0}^{rDFT}. \tag{6.9}$$

Furthermore, using the exact approaches as described above

$$E_T^{\Delta SCF} \equiv E_T^{TDDFT} \tag{6.10}$$

is expected. However, if approximate exchange functionals are used this will not be true. Therefore, the TT approach minimises the difference between $E_T^{\Delta SCF}$ and E_T^{TDDFT}

$$J_{TT}^2 = (E_T^{\Delta SCF} - E_T^{TDDFT})^2 \tag{6.11}$$

to acquire the optimal, ω, parameter for each system.[139]

6.3 Computational Details

For the calculations on PTZ-DBTO$_2$ and TAT-3DBTO$_2$ the Q-chem 5.0 quantum chemistry package[113] was used. Geometries of PTZ-DBTO$_2$[2]and TAT-3DBTO$_2$[130] were optimized DFT or LR-TDDFT within the TDA.[91] In both cases, the PBE0 exchange and correlation functional,[114] were used. All simulations were performed in vacuo. Excited-state energies were computed in the framework of LR-TDDFT using the TDA[91] and the long-range corrected (LRC)-ωPBEh functional.[140] A 6-31G* basis set[141, 87, 142] was used for both PTZ-DBTO$_2$ and TAT-3DBTO$_2$. Both (un)restricted DFT and LR-TDDFT methods were used for the OT and the TT processes.

Following this, for the small molecules displaying both CP and TADF properties the ORCA[143] quantum chemistry package was used. The geometries were optimised using DFT, within the approximation of the B3LYP[134, 135] functional and a Def2-SVP [115] basis set. Excited-state energies were computed in the framework of the long-range corrected LC-BLYP functional, as well as with DFT using B3LYP[134, 135]/Def2-SVP[115].

The *ab initio* MD was performed using the TeraChem[116, 117, 118] software using DFT in the electronic ground state, and LR-TDDFT in the excited S_1 state. The B3LYP functional[134, 135] and Def2-SVP [115] basis set was used throughout. The trajectory was propagated using the velocity Verlet algorithm and a finite temperature of 300 K. After an initial equilibration period of 5 ps starting from the ground state or S_1 state optimized geometry, the MD were run for a further 10 ps from which all properties were calculated. All calculations were conducted in vacuo.

In all cases, the dissymmetry of the emitted light (g-factor) was determined by the coupling between the electric ($\boldsymbol{\mu}$) and magnetic ($\boldsymbol{m}$) transition dipole moments [67], and can be expressed as:

$$g = \frac{4R}{D} = \frac{4|\boldsymbol{\mu}_{ij}||\boldsymbol{m}_{ij}|\cos(\tau)}{|\boldsymbol{\mu}_{ij}|^2 + |\boldsymbol{m}_{ij}|^2} \tag{6.12}$$

where R is the rotatory strength and D is the overall transition strength composed of the sum of $|\boldsymbol{\mu}_{ij}|^2$ and $|\boldsymbol{m}_{ij}|^2$. i and j refer to the initial and final states involved in the electronic transition. τ is the angle between $\boldsymbol{\mu}$ and $\boldsymbol{m}$. All of these properties were calculated using TDDFT and the methods described above. This is valid for the g-factors associated with both absorption (g_{abs}) and emission (g_{lum})[67]. The fundamental difference between the two is that g_{abs} describes the dissymmetry of thermally equilibrated ground state, while g_{lum} reflects the structure of the emissive state. Therefore very similar g_{abs} and g_{lum} values can be expected when there is little configurational reorganisation between the ground and excited states [67].

6.4 Results

6.4.1 The Influence of Geometry on Tuned-Range Separated Functionals

PTZ-DBTO$_2$

To begin with this study focuses on the D-A molecule PTZ-DBTO$_2$. Gibson *et al.* have used this molecule to model the dynamic spin-vibronic mechanism of TADF, as described in section 2.[144] PTZ-DBTO$_2$ is commonly found in one of two conformations in the ground state, equatorial (*eq*) or axial (*ax*), as seen in Figure 6.3. The molecule also displays a strong preference for an *eq* conformation at the minimum S_1 geometry, S_1^{Min}.

Figure 6.4 shows $J^2_{OT}(\omega)$ (a) and $J^2_{TT}(\omega)$ (b) for the three geometries of PTZ-DBTO$_2$ studied in this work, i.e. the ground state of the *eq* and *ax* conformers and the minimum of the S_1 geometry. This demonstrates that the TT approach is much more sensitive to the geometry of the molecule; bringing about much larger differences in the calculated optimal ω values for the TT approach, ω^*_{TT}, when compared to the ω values calculated for the OT approach, ω^*_{OT}. The optimal ω values for the TT approach range between 0 and $0.161 a_0^{-1}$ depending on the geometry used. Unsurprisingly, this apparent geometry dependence of the TT approach brings into question the generality of using this approach for particular molecules, but would also create problems when building potential energy surfaces. Large fluctuations in the ω will bring about challenges and ambiguities along the potential energy surface and thus in the descriptions of the ground and excited states. The optimal

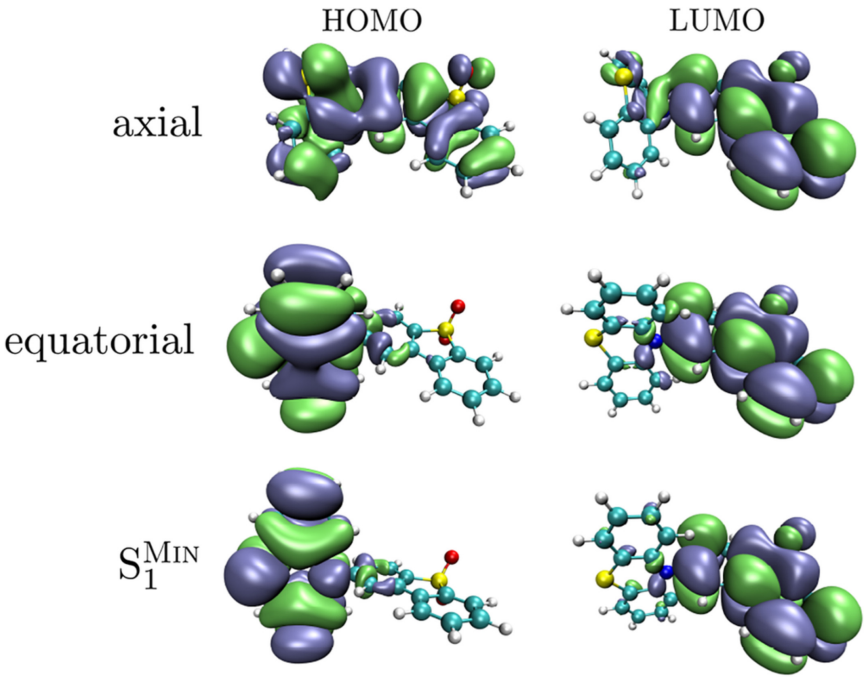

FIGURE 6.3: The HOMO (left) and LUMO (right) for the three geometries of PTZ-DBTO2 studied.[7]

ω values are $\omega^*_{OT} = 0.151 a_0^{-1}$ for the axial conformer and $\omega^*_{OT} = 0.161 a_0^{-1}$ for both the equatorial and S_1^{MIN} structures. The difference between the conformers derives from the character of the frontier orbitals. Indeed, for the equatorial and S_1^{MIN} structures the HOMO and LUMO orbitals are strongly localised on the donor and acceptor units, respectively. In contrast for the axial conformer both the HOMO and LUMO orbitals are delocalised over the whole molecule (See Figure 6.3) leading to a reduced ω^*_{OT}, as less exact exchange is required to describe the frontier orbitals which are less CT in character.

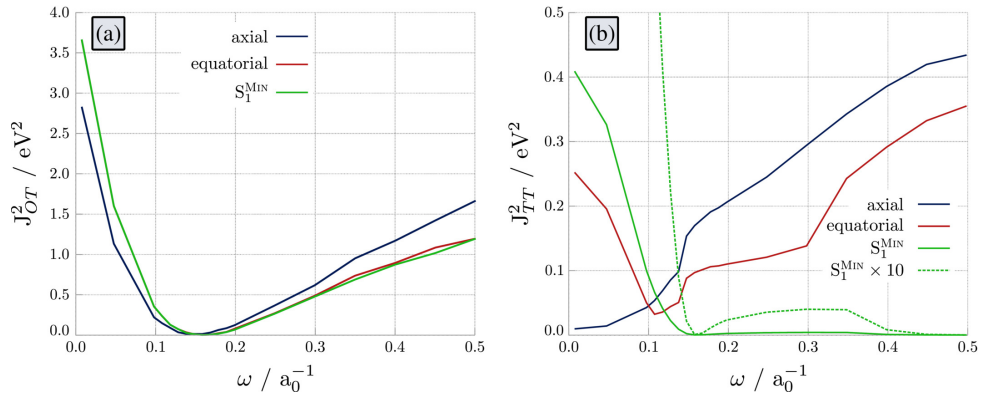

FIGURE 6.4: Evolution of J^2_{OT} (a) and J^2_{TT} (b) as a function of the range separation parameter ω for the equatorial (red), axial (blue) and S_1^{Min} (green) structures of PTZ-DBTO$_2$.[8]

The more strongly geometry dependent nature of the TT method is because, in contrast to the OT approach which is based on the one-particle properties of the HOMO and LUMO, it includes the electron hole effects that are associated with the excited state. As the name might suggest it is based upon the character of the lowest excited triplet state, this can be strongly dependent on ω. The lowest triplet state is a $\pi \rightarrow \pi^*$ triplet local excitation (^{3}LE($\pi\pi*$)), as this has no CT character the state is well described with small amounts of exact exchange and therefore $\omega^* \rightarrow 0$. For both the *eq* and S_1^{Min} the lowest initial state is the ^{3}CT, this is routinely underestimated in TDDFT due to the CT problem, therefore a larger ω value is required to improve the descriptions of these states. The CT states can be considered as pseudo-one-particle properties, and thus one would expect that the ω_{TT} would converge onto the ω_{OT}, this is the case for the S_1^{Min} but not for the *eq* geometry.

Table 6.1 shows the energetics of the low lying singlet and triplet excited states. For the different optimally tuned values of ω, there is a significant effect on key photophysical properties, e.g. the onset of the absorption and emission bands. For the energies calculated using PBEh (i.e. $\omega = 0.000 a_0^{-1}$), a poor description of the both the absorption and emission is achieved because of the involvement of the CT states because the TT was performed for ^{3}LE state. The energy of the S_1 state at the excited state geometry is 1.62 eV (765 nm) and is in poor agreement with the emission observed experimentally of $\sim$590 nm [145]. In addition, the onset of the absorption band observed experimentally is around 350-400 nm, which does not agree with the lowest singlet state of either the axial (3.70 eV) or equatorial (2.57 eV) structures. In contrast, both $\omega = 0.113 a_0^{-1}$ and $\omega = 0.160 a_0^{-1}$ yield much better agreement with both the absorption and emission energies observed experimentally.

Importantly, the fragility of the application of the TT approach, especially when there are low lying CT and LE states that can mix, has clearly been highlighted here. Indeed, the method will produce the optimal range separation parameter, ω, for the lowest lying triplet state of any nature, but as demonstrated this will be very sensitive to change if the molecule displays a high density of states. For efficient TADF it has been reported that mixing of states is integral to the TADF mechanism, there is a second order vibronically coupled mechanism at play. The rISC mechanism in D-A CT molecules relies on close lying states, such as local triplet states, to mediate the spin orbit coupling between the singlet and triplet states.[2] Thus, the fragility displayed by the TT approach will become cumbersome when applying to TADF emitters, for which the photophysical mechanism relies on the mixing of these close lying states. Futhermore, when considering the TT functional for the S_1 configuration it is reported, in Figure 6.4b, that for ω=0.4-0.5a_0^{-1} the functional becomes very close to zero. This result has been disregarded the character of the T_1 state obtained with TDDFT becomes a ^{3}LE(A) for values of ω>0.35a_0^{-1}, which is different to the nature obtained with uDFT. Therefore, the small value of the TT functional is coincidental and cannot be considered to provide a physical solution.[7]

PBEh ($\omega = 0a_0^{-1}$)								
axial			equatorial			S_1^{Min}		
State	Nature	ΔE/eV	State	Nature	ΔE/eV	State	Nature	ΔE/eV
T_1	^3LE_A	3.00	T_1	$^3CT_{D\to A}$	2.56	T_1	$^3CT_{D\to A}$	1.61
T_2	^3LE_A	3.48	S_1	$^1CT_{D\to A}$	2.57	S_1	$^1CT_{D\to A}$	1.62
T_3	^3LE_A	3.54	T_2	$^3CT_{D\to A}$	2.88	T_2	$^3CT_{D\to A}$	2.39
S_1	$^3CT_{D\to A}$	3.70	S_2	$^3CT_{D\to A}$	3.95	S_2	$^3CT_{D\to A}$	2.61
T_4	^3LE_D	3.72	T_3	$^3CT_{D\to A}/^3LE_D$	3.21	T_3	$^3CT_{D\to A}/^3LE_D$	2.61
T_5	^3LE_D	3.73	T_4	$^3CT_{D\to A}$	3.71	T_4	^3LE_A	2.76
LRC-ωPBEh ($\omega = \omega^*_{OT}a_0^{-1}$)								
axial			equatorial			S_1^{Min}		
State	Nature	ΔE/eV	State	Nature	ΔE/eV	State	Nature	ΔE/eV
T_1	^3LE_A	3.16	T_1	^3LE_D	3.24	T_1	$^3CT_{D\to A}/^3LE_D$	2.58
T_2	$^3LE_A/^3CT_{D\to A}$	3.68	T_2	^3LE_A	3.31	S_1	$^1CT_{D\to A}$	2.67
T_3	$^3LE_A/^3CT_{D\to A}$	3.69	T_3	$^3CT_{D\to A}$	3.57	T_2	$^3CT_{D\to A}/^3LE_D$	2.76
T_4	^3LE_D	3.82	S_1	$^1CT_{D\to A}$	3.59	T_3	^3LE_A	2.83
T_5	$^3LE_D/^3LE_A$	3.85	S_2	$^1CT_{D\to A}$	3.76	S_2	$^3CT_{D\to A}$	3.31
S_1	$^3CT_{D\to A}$	4.18	T_4	^3LE_D	3.77	T_4	$^3CT_{D\to A}$	3.32
LRC-ωPBEh ($\omega = \omega^*_{TT}a_0^{-1}$)								
axial			equatorial			S_1^{Min}		
State	Nature	ΔE/eV	State	Nature	ΔE/eV	State	Nature	ΔE/eV
T_1	^3LE_A	3.16	T_1	$^3CT_{D\to A}/^3LE_D$	3.12	T_1	$^3CT_{D\to A}/^3LE_D$	2.58
T_2	$^3LE_A/^3CT_{D\to A}$	3.68	T_2	$^3CT_{D\to A}/^3LE_D$	3.14	S_1	$^1CT_{D\to A}$	2.67
T_3	$^3LE_A/^3CT_{D\to A}$	3.69	S_1	$^3CT_{D\to A}$	3.15	T_2	$^3CT_{D\to A}/^3LE_D$	2.76
T_4	^3LE_D	3.82	T_3	^3LE_D	3.26	T_3	^3LE_A	2.83
T_5	$^3LE_D/^3LE_A$	3.85	S_2	$^1CT_{D\to A}$	3.40	S_2	$^1CT_{D\to A}$	3.31
S_1	$^3CT_{D\to A}$	4.18	T_4	$^3CT_{D\to A}$	3.47	T_4	$^3CT_{DA}$	3.32

TABLE 6.1: Electronic structure of PTZ-DBTO$_2$ at all three studied geometries and at the optimal values of $\omega = 0a_0^{-1}$, $\omega = \omega^*_{OT}$ and $\omega = \omega^*_{TT}$.

TAT-3DBTO$_2$

The emitter TAT-3DBTO$_2$ has a rigid triazatruxene central donor that is surrounded by three acceptors of DBTO$_2$ forming a D-A$_3$ structure. As with the PTZ-DBTO$_2$ system, there are multiple geometries investigated in this study, in this case just two. The Franck-Condon (FC) geometry and the optimised excited S$_1$, S_1^{Min}, geometry. The S_1^{Min} geometry displays CT character involving the D and one A. The CT character of the state is enhanced by the reduction in electronic coupling of the D and A groups upon electron transfer to the A, when this electron transfer takes place the A rotates about the C-N bond to form a perpendicular arrangement with the D centre. It is known that this design (D-A$_3$) exhibits a high density of excited states, therefore, as shown above, this could prove challenging for the tuning methods.[130]

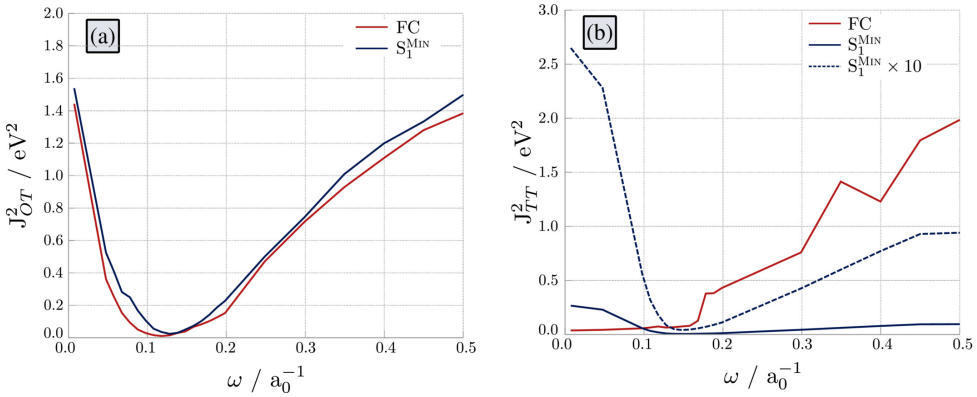

FIGURE 6.5: Evolution of J_{OT}^2 (a) and J_{TT}^2 (b) as a function of the range separation parameter ω for the FC (red) and S_1^{Min} (blue) structures of TAT-3DBTO$_2$.[8]

Figure 6.5 shows both the J_{OT}^2 and J_{TT}^2, (a) and (b) respectively, for the FC and S_1^{Min} geometries. Similarly to the PTZ-DBTO$_2$ study, the OT approach yields similar minima for both geometries, the values of ω_{OT}^* for the FC and S_1^{Min} geometries were $0.118a_0^{-1}$ and $0.131a_0^{-1}$, respectively. At larger values of ω some discontinuities were exhibited for J_{OT}^2, this is due to symmetry-induced degeneracy of the LUMO and LUMO+1 at this geometry causing an instability in the SCF convergence. When studying large systems that exhibit symmetry care must be taken, in this case the irreducible representations of the C$_3$ point group of symmetry are A and E, the latter are doubly degenerate. However, for TAT-3DBTO$_2$, the problem usually affects larger values of ω and therefore does not impact the determination of ω_{OT}^*.[7] Furthermore, when considering J_{TT}^2, Figure 6.5b, the S_1^{Min} state shows good agreement with the J_{OT}^2, in this case $\omega_{TT}^* = 0.160a_0^{-1}$ this is due to the CT character of this state. However, as expected, when there is a high density of states, the TT method is more challenged. In this case, in the ground state (FC), there is a high density of states due to the three acceptor units, for which only one is involved in the excited state. In TAT-3DBTO$_2$ there are six triplet states within

0.15 eV at $\omega \rightarrow 0a_0^{-1}$ and four triplet states within 0.6 eV at $\omega = 0.600a_0^{-1}$.[7] As shown in Figure 6.5b J_{TT}^2 is at a minimum when $\omega = 0.000a_0^{-1}$, this is due to the mixing that is induced by degeneracy between the lowest lying triplet states and the higher lying triplet states. Additionally, a further minima, that looks to be in agreement with the S_1^{Min} geometry is seen at $\omega = 0.160a_0^{-1}$, this is because the ^3CT has switched to the lowest state in place of the lowest triplet state.[7] Therefore concurring that the TT approach is very sensitive to geometry. Crucially in the case of D-A TADF emitters when close lying states are important for the emission process, this method is likely to be inappropriate for application in these cases.

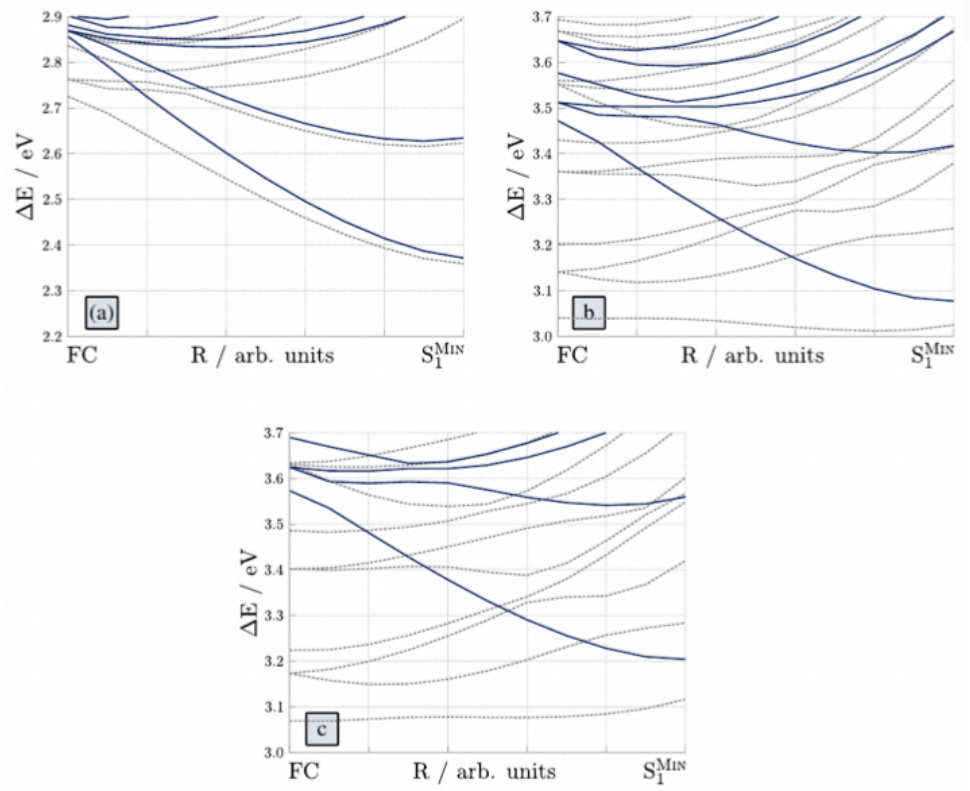

FIGURE 6.6: The linear reaction pathway between the FC geometry and S_1^{MIN} (calculated at PBE0 level) of TAT-3DBTO$_2$ using the (a) ω=0.000 a_0^{-1} (b) ω=0.118 a_0^{-1} and (c) ω=0.131 a_0^{-1}. The solid blue lines are singlet states and the Dash lines are triplet states. All energies are plotted relative to the ground state energy at the FC geometry.[8]

The potential energy curves in Figure 6.6 are a linear reaction pathway between the FC geometry and the S_1 minimum using the ω obtained from Figure 6.6. Clearly, as observed for PTZ-DBTO$_2$, in the case that $\omega \rightarrow 0a_0^{-1}$ (PBEh) the potential energy curves are dominated by low lying CT states. Indeed, as shown in Tables 6.2-6.4, the vertical energy gap between the S_1 and the ground state at this geometry is 1.96 eV (630 nm) which offers poor

PBEh ($\omega = 0a_0^{-1}$)					
FC			S_1^{MIN}		
State	Nature	ΔE / eV	State	Nature	ΔE / eV
T_1	$^3CT_{D\rightarrow A}$	2.73	T_1	$^3CT_{D\rightarrow A_1}$	1.95
T_2	$^3CT_{D\rightarrow A}$	2.76	S_1	$^1CT_{D\rightarrow A_1}$	1.96
T_3	$^3CT_{D\rightarrow A}$	2.76	T_2	$^3CT_{D\rightarrow A_1}$	2.21
T_4	$^3CT_{D\rightarrow A}$	2.84	S_2	$^1CT_{D\rightarrow A_1}$	2.23
S_1	$^1CT_{D\rightarrow A}$	2.86	T_3	$^3CT_{D\rightarrow A_3}$	2.49
T_5	$^3CT_{D\rightarrow A}$	2.87	S_3	$^1CT_{D\rightarrow A_3}$	2.55
T_6	$^3CT_{D\rightarrow A}$	2.87	T_4	$^3CT_{D\rightarrow A_2}$	2.56
S_2	$^1CT_{D\rightarrow A}$	2.87	S_4	$^1CT_{D\rightarrow A_2}$	2.59
S_3	$^1CT_{D\rightarrow A}$	2.87	T_5	$^3CT_{D\rightarrow A_3}$	2.70
S_4	$^1CT_{D\rightarrow A}$	2.88	T_6	$^3CT_{D\rightarrow A_1}/^3LE_{A_1}$	2.83
S_5	$^1CT_{D\rightarrow A}$	2.90	T_7	$^3CT_{D\rightarrow A_2}$	2.75
S_6	$^1CT_{D\rightarrow A}$	2.90	S_5	$^1CT_{D\rightarrow A_3}$	2.75
T_7	$^3CT_{D\rightarrow A}$	3.08	T_8	$^3CT_{D\rightarrow A_1}$	2.81
T_8	$^3CT_{D\rightarrow A}$	3.20	S_6	$^1CT_{D\rightarrow A_2}$	2.82
T_9	$^3CT_{D\rightarrow A}$	3.20	S_7	$^1CT_{D\rightarrow A_1}$	2.83

TABLE 6.2: Electronic structure of TAT-3DBTO$_2$ at the minima of the ground state and ^{1}CT and at the $\omega = 0.0a_0^{-1}$.

agreement with the experimental emission spectrum (490 nm) [130]. In contrast, the emission energy estimated is in much better agreement for the ω obtained by OT and TT which are 2.78 eV (445 nm) and 2.95 eV (420 nm), respectively. In addition, the energy of the lowest triplet state for both approaches agrees with the phosphorescence spectrum recorded in ref. [130] and the mixed CT/LE character observed is in good agreement with the vibronic transitions observed experimentally. In contrast the low energy of the CT states calculated using PBEh predicts the lowest triplet state exhibits only CT character which is inconsistent with the experimentally observed spectrum. Finally, besides the differences in the absolute energy, the potential energy curves for the ω's obtained by OT and TT exhibit similar shapes, suggesting that although the values obtained are geometry dependent, fixing the value does not have a dramatic effect of the interpretation obtained.

LRC-ωPBEh ($\omega = \omega^*_{OT}$)					
FC			S_1^{MIN}		
State	Nature	ΔE / eV	State	Nature	ΔE / eV
T_1	$^3CT_{D\to A}/^3LE_D$	3.04	T_1	$^3CT_{D\to A_1}/^3LE_{A_1}$	2.69
T_2	$^3CT_{D\to A}/^3LE_A$	3.14	S_1	$^1CT_{D\to A_1}$	2.78
T_3	$^3CT_{D\to A}/^3LE_A$	3.14	T_2	$^3CT_{D\to A_1}/^3LE_{A_1}$	2.86
T_4	$^3LE_D/^3LE_A$	3.20	T_3	$^3CT_{D\to A_{1,2}}/^3LE_D$	3.00
T_5	$^3CT_{D\to A}/^3LE_D$	3.36	T_4	$^3CT_{D\to A_1}$	3.12
T_6	$^3CT_{D\to A}/^3LE_D$	3.36	S_2	$^1CT_{D\to A_1}$	3.13
T_7	$^3CT_{D\to A}/^3LE_D$	3.43	T_5	$^3CT_{D\to A_2}/^3LE_{A_2}$	3.15
S_1	$^1CT_{D\to A}$	3.47	T_6	$^3CT_{D\to A_3}/^3LE_{A_3}$	3.18
S_2	$^1CT_{D\to A}$	3.51	T_7	$^3CT_{D\to A_2}$	3.30
S_3	$^1CT_{D\to A}$	3.51	S_3	$^1CT_{D\to A_2}$	3.37
T_8	$^3CT_{D\to A}/^3LE_A$	3.55	T_8	$^3CT_{D\to A_{2,3}}$	3.39
T_9	$^3CT_{D\to A}/^3LE_A$	3.55	S_4	$^1CT_{D\to A_3}$	3.42
S_4	$^1CT_{D\to A}$	3.56	T_9	$^3CT_{D\to A_{2,3}}$	3.45

TABLE 6.3: Electronic structure of TAT-3DBTO$_2$ at the minima of the ground state and ^{1}CT and at the optimal value of $\omega = \omega^*_{OT}$.

LRC-ωPBEh ($\omega = \omega^*_{TT}$)					
FC			S_1^{MIN}		
State	Nature	ΔE / eV	State	Nature	ΔE / eV
T_1	$^3CT_{D\to A}$	2.73	T_1	$^3CT_{D\to A_1}/^3LE_{A_1}$	2.76
T_2	$^3CT_{D\to A}$	2.76	T_2	$^3CT_{D\to A_1}/^3LE_{A_1}$	2.95
T_3	$^3CT_{D\to A}$	2.76	S_1	$^1CT_{D\to A_1}$	2.95
T_4	$^3CT_{D\to A}$	2.84	T_3	$^3CT_{D\to A_1}/^3CT_{D\to A_3}/^3LE_{A_1}/^3LE_{A_3}$	3.06
S_1	$^1CT_{D\to A}$	2.86	T_4	$^3CT_{D\to A_2}/^3CT_{D\to A_3}/^3LE_{A_2}/^3LE_{A_3}$	3.20
T_5	$^3CT_{D\to A}$	2.87	T_5	$^3CT_{D\to A_2}/^3CT_{D\to A_3}/^3LE_{A_2}/^3LE_{A_3}$	3.22
T_6	$^3CT_{D\to A}$	2.87	T_6	$^3CT_{D\to A_1}$	3.31
S_2	$^1CT_{D\to A}$	2.87	S_2	$^1CT_{D\to A_1}$	3.33
S_3	$^1CT_{D\to A}$	2.87	T_7	$^3CT_{D\to A_1}/^3CT_{D\to A_2}/^3LE_D/^3LE_{A_2}$	3.36
S_4	$^1CT_{D\to A}$	2.88	T_8	$^3CT_{D\to A_2}/^3CT_{D\to A_3}/^3LE_D$	3.47
S_5	$^1CT_{D\to A}$	2.90	S_3	$^1CT_{D\to A_2}$	3.54
S_6	$^1CT_{D\to A}$	2.90	T_9	$^3CT_{D\to A_2}/^3CT_{D\to A_3}/^3LE_{A_2}$	3.56
T_7	$^3CT_{D\to A}$	3.08	S_4	$^1CT_{D\to A_3}$	3.59
T_8	$^3CT_{D\to A}$	3.20	T_{10}	$^3CT_{D\to A_1}/^3CT_{D\to A_2}/^3CT_{D\to A_3}$	3.61
T_9	$^3CT_{D\to A}$	3.20	T_{11}	$^3CT_{D\to A_1}/^3CT_{D\to A_2}/^3CT_{D\to A_3}$	3.64

TABLE 6.4: Electronic structure of TAT-3DBTO$_2$ at the minima of the ground state and ^{1}CT and at the optimal value of $\omega = \omega^*_{TT}$.

6.4.2 Assessing Chiral Perturbation for achieving CP-TADF Emitters

The methods described above have shown that the inclusion of the description of the non-local effects through optimally tuned-range separated exchange and correlation functions is crucial for TDDFT calculations which include CT states. This has demonstrated a significant improvement in the energetics of the excited states. However, this will also influence other properties in the system. In this section, we will study the influence of the optimal tuning approach on the chiroptical response of molecules. In the context of organic electronics, delivering molecules which chiroptical response can bypass the need for anti-glare filters, not only reducing power consumption but also reducing the driving voltages of the devices. The following molecules, Figure 6.2 combine traditional TADF D-A emitters with a chiral perturbation with the intention to create TADF emitters that emit CP luminescence. [146] The appeal of this approach is that it can exploit well known TADF emitters and achieve CP emission using simple modifications.

Excited State Properties and CPL at Critical Points

Firstly, the study implemented a hybrid functional, in this case B3LYP[134, 135], this was compared to the OT approach for each emitter. The results of the studies are shown in Tables 6.5-6.8. This shows, consistent with the previous section, there is a significant effect on the energy of the excited states. A similar effect is also observed with the g-factor, although its apparent influence appears reduced due to the small numbers involved.

As expected, all four emitters showed good TADF properties. The results of the studies for both the B3LYP and OT approach show close lying S_1 and T_1 states with CT_{DA} character, particularly in the S_1 optimised geometries. The emitters show small values for ΔE_{ST}, 0.03 eV, 0.03 eV, 0.09 eV and 0.11 eV for emitters **A**, **B**, **C** and **D**, respectively. Therefore, showing that they will enable efficient ISC. For the higher lying states some LE character can be seen, this is expected. However for emitter **D** in the S_0 geometry, the low lying triplet states (T_1, T_2 and T_3) exhibit LE character. There is a LE, $^3LE_{Deloc}$, is shown to be delocalised across the whole molecule and also a LE, ^3LE_C , localised on the chiral perturbing unit, as shown in Figure 6.7. However, as it is of LE character it will not emit via TADF.

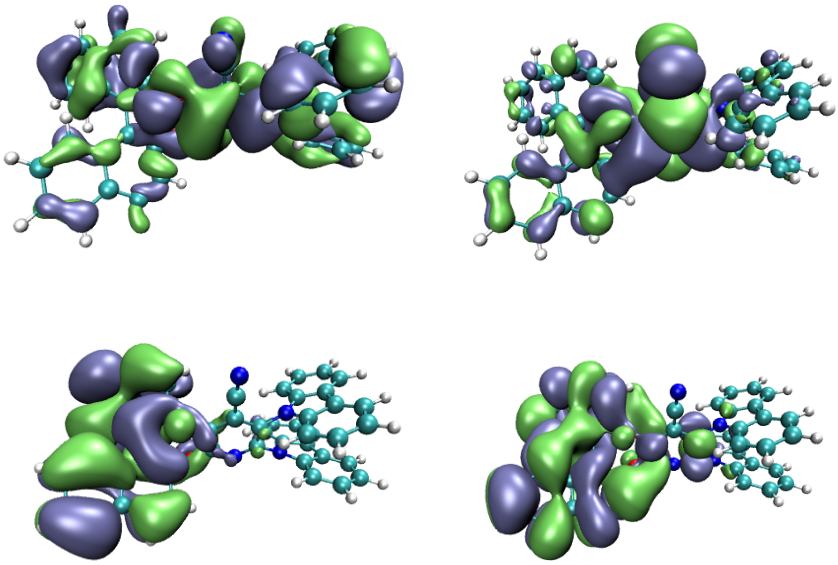

FIGURE 6.7: Location of the frontier orbitals for Emitter **6** in the OT, S_0 geometry study. Top shows the orbitals involved in a $^3LE_{Deloc}$ transition. Bottom shows the orbitals involved in a ^3LE_C transition.

Indeed, throughout the g-factor calculated is <0.005. This is typical for molecular scale dissymmetry factors. This is because, in the visible regime the wavelength of light is much larger (hundreds of nanometres) than the typical size of a molecule (tens of Angström) and therefore the electric dipole approximation is valid meaning that the electric-magnetic coupling (natural optical activity) is small. The magnetic transition dipole only becomes significant for dipole forbidden transitions or when $kr > 1$, *i.e.* high photon energies when $k = 2\pi/\lambda$ becomes large or if the exciton size, which influences the electron separation occurring in r becoming $\sim$ to the wavelength of light.

Another reason the g-factors for each of the emitters are small is due to the nature of the chiral pertubation approach. Indeed, by scrutinising the character of the frontier orbitals this can be further appreciated. For emitter **A**, Figure 6.8 shows that very little of the S_1 state is spread over the chiral perturbing unit of the molecule, with this small spread of the S_1 comes a small influence on the chiroptical response of the system. However, the frontier orbitals from the OT study show slightly more localisation on the chiral perturbing unit, as shown in Figure 6.8. Therefore, providing an explanation for why an, albeit very slightly, larger g-factor is reported for the OT method when compared to the B3LYP study. The same can be said for the frontier orbitals of emitters **B**, **C** and **D**. Furthermore, these results suggest that the traditional design of using a D-A structure with a chiral appendage that is not involved in the active chromophore may not be the optimal way to move

Emitter A							
S_0 Geometry							
B3LYP				OT			
State	Nature	ΔE/eV	*g*-factor	State	Nature	ΔE/eV	*g*-factor
T_1	$^3CT_{D\to A}$	2.40	-	T_1	$^3CT_{D\to A}$	2.56	-
T_2	$^3CT_{D\to A}$	2.52	-	T_2	$^3CT_{D\to A}$	2.81	-
S_1	$^1CT_{D\to A}$	2.53	-0.0003	S_1	$^1CT_{D\to A}$	2.85	-0.0004
S_2	$^1CT_{D\to A}$	2.62	0.01	T_3	^3LE_C	2.91	0.03
T_3	$^3CT_{D\to A}$	2.80	-	T_4	^3LE_C	3.02	-
S_1 Geometry							
B3LYP				OT			
State	Nature	ΔE/eV	*g*-factor	State	Nature	ΔE/eV	*g*-factor
T_1	$^3CT_{D\to A}$	1.77	-	T_1	$^3CT_{D\to A}$	2.05	-
S_1	$^1CT_{D\to A}$	1.78	0.0005	S_1	$^1CT_{D\to A}$	2.08	0.0002
T_2	$^3CT_{D\to A}$	2.06	-	T_2	$^3CT_{D\to A}$	2.43	-
S_2	$^1CT_{D\to A}$	2.08	0.006	S_2	$^1CT_{D\to A}$	2.48	0.02
T_3	$^3CT_{D\to A}$	2.22	-	T_3	$^3CT_{D\to A}$	2.78	-
T_1 Geometry							
B3LYP				OT			
State	Nature	ΔE/eV	*g*-factor	State	Nature	ΔE/eV	*g*-factor
T_1	$^3CT_{D\to A}$	1.77	-	T_1	$^3CT_{D\to A}$	2.05	-
S_1	$^1CT_{D\to A}$	1.78	0.0005	S_1	$^3CT_{D\to A}$	2.08	0.0002
T_2	$^3CT_{D\to A}$	2.06	-	T_2	$^3CT_{D\to A}$	2.43	-
S_2	$^1CT_{D\to A}$	2.08	0.006	S_2	$^1CT_{D\to A}$	2.48	0.0007
T_3	$^3CT_{D\to A}$	2.22	-	T_3	^3LE_C	2.78	-

TABLE 6.5: Energies and *g*-factors of the two studies, DFT(B3LYP) (left) and OT(LC-BLYP) (right), on the emitter **A**, for the optimised S_0, S_1 and T_1 geometries.

Emitter B							
S_0 Geometry							
B3LYP				OT			
State	Nature	ΔE/eV	*g*-factor	State	Nature	ΔE/eV	*g*-factor
T_1	$^3CT_{D\to A}$	2.07	-	T_1	$^3CT_{D\to A}$	2.35	-
S_1	$^1CT_{D\to A}$	2.12	0.001	T_2	$^3CT_{D\to A}$	2.50	-
T_2	$^3CT_{D\to A}$	2.12	-	S_1	$^1CT_{D\to A}$	2.51	0.008
S_2	$^1CT_{D\to A}$	2.16	0.003	S_2	$^1CT_{D\to A}$	2.62	0.005
T_3	$^3CT_{D\to A}$	2.49	-	T_3	^3LE_C	2.89	-
S_1 Geometry							
B3LYP				OT			
State	Nature	ΔE/eV	*g*-factor	State	Nature	ΔE/eV	*g*-factor
T_1	$^3CT_{D\to A}$	1.36	-	T_1	$^3CT_{D\to A}$	1.76	-
S_1	$^1CT_{D\to A}$	1.37	-0.002	S_1	$^1CT_{D\to A}$	1.79	0.002
T_2	$^3CT_{D\to A}$	1.63	-	T_2	$^3CT_{D\to A}$	2.06	-
S_2	$^1CT_{D\to A}$	1.64	0.0007	S_2	$^1CT_{D\to A}$	2.09	0.003
T_3	$^3CT_{D\to A}$	1.81	-	T_3	$^3CT_{D\to A}$	2.42	-
T_1 Geometry							
B3LYP				OT			
State	Nature	ΔE/eV	*g*-factor	State	Nature	ΔE/eV	*g*-factor
T_1	$^3CT_{D\to A}$	1.36	-	T_1	$^3CT_{D\to A}$	1.76	-
S_1	$^1CT_{D\to A}$	1.37	-0.002	S_1	$^1CT_{D\to A}$	1.79	-0.001
T_2	$^3CT_{D\to A}$	1.63	-	T_2	$^3CT_{D\to A}$	2.06	-
S_2	$^1CT_{D\to A}$	1.64	0.0007	S_2	$^1CT_{D\to A}$	2.09	-0.006
T_3	$^3CT_{D\to A}$	1.81	-	T_3	$^3CT_{D\to A}$	2.42	-

TABLE 6.6: Energies and *g*-factors of the two studies, DFT(B3LYP) (left) and OT(LC-BLYP) (right), on the emitter **B**, for the optimised S_0, S_1 and T_1 geometries.

Emitter C							
S_0 Geometry							
B3LYP				OT			
State	Nature	ΔE/eV	*g*-factor	State	Nature	ΔE/eV	*g*-factor
T_1	$^3CT_{D\to A}$	2.18	-	T_1	$^3CT_{D\to A}$	2.35	-
T_2	$^3CT_{D\to A}$	2.26	-	S_1	$^1CT_{D\to A}$	2.48	0.0003
S_1	$^1CT_{D\to A}$	2.26	0.0002	T_2	$^3CT_{D\to A}$	2.64	-
S_2	$^1CT_{D\to A}$	2.32	0.003	S_2	$^1CT_{D\to A}$	2.76	-0.003
T_3	$^3CT_{D\to A}$	2.65	-	T_3	^3LE_C	2.88	-
S_1 Geometry							
B3LYP				OT			
State	Nature	ΔE/eV	*g*-factor	State	Nature	ΔE/eV	*g*-factor
T_1	$^3CT_{D\to A}$	1.49	-	T_1	$^3CT_{D\to A}$	2.04	-
S_1	$^1CT_{D\to A}$	1.50	0.0002	S_1	$^1CT_{D\to A}$	2.13	0.0006
T_2	$^3CT_{D\to A}$	1.72	-	T_2	$^3CT_{D\to A}$	2.42	-
S_2	$^1CT_{D\to A}$	1.76	0.0003	S_2	$^1CT_{D\to A}$	2.52	-0.005
T_3	$^3CT_{D\to A}$	2.03	-	T_3	$^3CT_{D\to A}$	2.80	-
T_1 Geometry							
B3LYP				OT			
State	Nature	ΔE/eV	*g*-factor	State	Nature	ΔE/eV	*g*-factor
T_1	$^3CT_{D\to A}$	2.24	-	T_1	$^3CT_{D\to A}$	1.94	-
S_1	$^1CT_{D\to A}$	2.33	0.0001	S_1	$^1CT_{D\to A}$	1.99	0.0006
T_2	$^3CT_{D\to A}$	2.33	-	T_2	$^3CT_{D\to A}$	2.29	-
S_2	$^1CT_{D\to A}$	2.73	0.004	S_2	$^1CT_{D\to A}$	2.33	0.003
T_3	$^3CT_{D\to A}$	2.71	-	T_3	$^3CT_{D\to A}$	2.72	-

TABLE 6.7: Energies and *g*-factors of the two studies, DFT(B3LYP) (left) and OT(LC-BLYP) (right), on the emitter **C**, for the optimised S_0, S_1 and T_1 geometries.

Emitter D							
S_0 Geometry							
B3LYP				OT			
State	Nature	ΔE/eV	g-factor	State	Nature	ΔE/eV	g-factor
T_1	$^3CT_{D\rightarrow A}$	2.59	-	T_1	$^3LE_{Deloc}$	2.66	-
T_2	$^3CT_{D\rightarrow A}$	2.78	-	T_2	$^3LE_{Deloc}/^3LE_C$	2.90	-
S_1	$^1CT_{D\rightarrow A}$	2.81	0.0006	T_3	^3LE_C	3.01	-
T_3	$^3LE_{Deloc}/^3LE_C$	2.85	-	S_1	$^1CT_{D\rightarrow A}$	3.03	0.0007
S_2	$^1CT_{D\rightarrow A}$	2.89	-0.007	T_4	$^3CT_{D\rightarrow A}$	3.06	-
S_1 Geometry							
B3LYP				OT			
State	Nature	ΔE/eV	g-factor	State	Nature	ΔE/eV	g-factor
T_1	$^3CT_{D\rightarrow A}$	1.83	-	T_1	$^3CT_{D\rightarrow A}$	2.05	-
S_1	$^1CT_{D\rightarrow A}$	1.87	0.0003	S_1	$^1CT_{D\rightarrow A}$	2.16	0.0001
T_2	$^3CT_{D\rightarrow A}$	2.18	-	T_2	$^3CT_{D\rightarrow A}$	2.61	-
S_2	$^1CT_{D\rightarrow A}$	2.22	-0.002	S_2	$^1CT_{D\rightarrow A}$	2.71	-0.0001
T_3	$^3CT_{D\rightarrow A}$	2.37	-	T_3	$^3LE_{Deloc}/^3LE_C$	2.86	-
T_1 Geometry							
B3LYP				OT			
State	Nature	ΔE/eV	g-factor	State	Nature	ΔE/eV	g-factor
T_1	$^3CT_{D\rightarrow A}$	1.83	-	T_1	$^3CT_{D\rightarrow A}$	2.13	-
S_1	$^1CT_{D\rightarrow A}$	1.87	0.0003	S_1	$^1CT_{D\rightarrow A}$	2.27	0.0003
T_2	$^3CT_{D\rightarrow A}$	2.18	-	T_2	$^3CT_{D\rightarrow A}$	2.57	-
S_2	$^1CT_{D\rightarrow A}$	2.22	-0.002	S_2	$^3CT_{D\rightarrow A}$	2.70	-0.001
T_3	$^3CT_{D\rightarrow A}$	2.37	-	T_3	$^3LE_{Deloc}/^3LE_C$	2.86	-

TABLE 6.8: Energies and g-factors of the two studies, DFT(B3LYP) (left) and OT(LC-BLYP) (right), on the emitter **D**, for the optimised S_0, S_1 and T_1 geometries.

forward with the design of CP-TADF emitter. However, it is important to note that the work by Feuillastre *et al.*,[132] reports g-factors of 0.0013 for emitter **B**. When considering the calculated emission, shown in Table 6.6, it is clear that the OT approach reports g-factors of the same magnitude for all three geometries. Thus showing that the OT approach provides reasonable agreement with the experimental results.

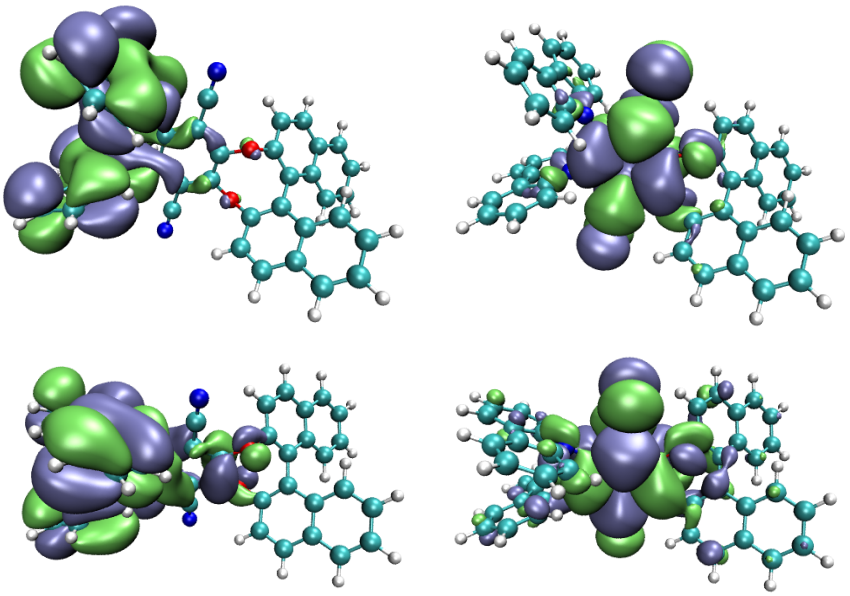

FIGURE 6.8: The HOMO (right) and LUMO (left) orbitals for Emitter **A**. Top B3LYP S_1 geometry, Bottom OT S_1 geometry.

Assessing the Potential for Axially Chiral TADF Emitters

The aforementioned limitations of the chiral perturbation approach leads us to consider an alternative approach. A second possible way to design a CP-TADF emitter, is to build the molecule with a design that minimises the distance between the chiral perturbing unit and the active chromophore, with the aim for the chiral section to play a greater role in the emission properties, and thus increase the chiroptical response.[146]

This section investigates the axially chiral emitter, shown in Figure 6.2 **E**. The emitter is comprised of a carbazole D, a triazine A component, as well as, a phenyl bridge between the two, therefore, localising the HOMO and LUMO on the D and A, respectively, as shown in Figure 6.9. Thus, minimising the energy gap between the first excited singlet and triplet states (ΔE_{S1-T1}) and therefore, creating the CT state that is favourable for TADF. The D and bridging groups include asymmetric methyl groups to enforce axial chirality. Importantly, the size of the methyl group is sufficiently small to distort the D-A group sufficiently from orthongonality to prevent TADF.

Critical points, S_0, S_1 and T_1 optimised geometries, along the potential energy surfaces were calculated for this emitter and the energetics and g-factor of the important states are shown in Table 6.9. There is a noticeable difference between the B3LYP results and the OT results. This is not surprising due to the improved description of the excited states by the OT approach. For applications in OLEDs the energy difference between the S_1 and T_1 states, $\Delta E_{S_1-T_1}$, is crucial to predicting their efficiency. The mechanism of TADF uses rISC to reengage the dark triplet states. There are many competing pathways that can occur upon excitation. The first is prompt fluorescence from the S_1 to the S_0. Competing with this pathway, is decay involving the triplet manifold, from which phosphorescent decay can occur, unfavourable in OLEDs. The process of rISC is possible when $\Delta E_{S_1-T_1}$ is small and phosphorescence is slow, therefore this is ideal for OLED devices. A crucial factor when considering the TADF performance of a system is the ΔE_{ST}. A small energy gap allows for efficient ISC between the light and dark states and therefore is a mechanism to re-engage the inherent loss of 75% upon excitation to the dark states. With a small energy gap, ΔE_{ST} of 0.07eV, Table 6.9, enabling efficient ISC, thus the emitter is likely to exhibit efficient TADF. Figure 6.9 shows the CT character of the HOMO and LUMO of the emitter, left and right respectively, for the B3LYP study (top) and OT study (bottom).

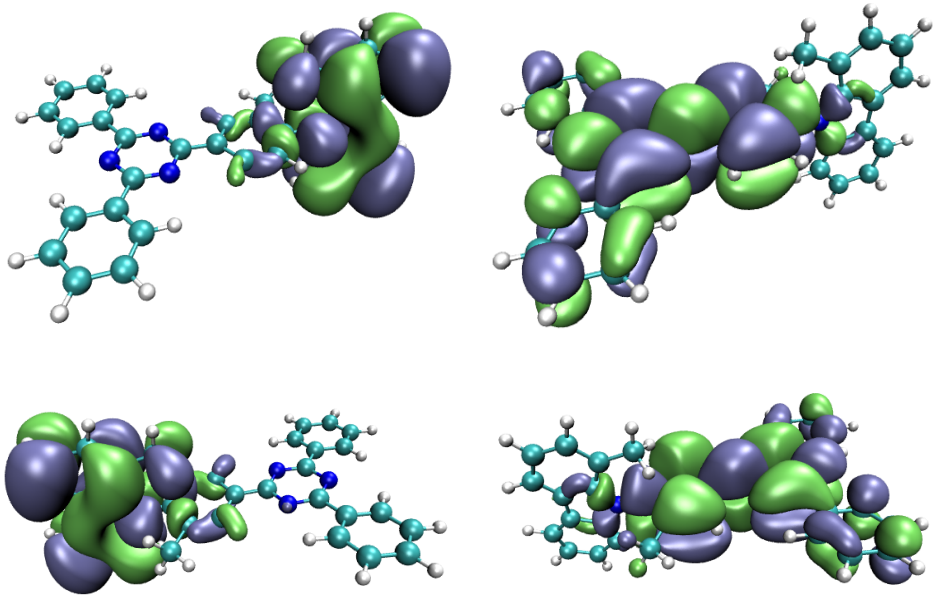

FIGURE 6.9: The HOMO (right) and LUMO (left) orbitals for emitter **E**. For the B3LYP approach (top) and the OT approach (bottom).

As discussed previously, dynamics around the D-A bond have a strong effect on the performance of TADF emitters via the spin-vibronic mechanism, however, its effect on the CPL is less clear. To study this in more detail, MD

Emitter E							
S_0 Geometry							
B3LYP				OT			
State	Nature	ΔE/eV	g_{lum}	State	Nature	ΔE/eV	g_{lum}
T_1	$^3CT_{D-A}$	2.82	-	T_1	^3LE_A	2.25	-
S_1	$^1CT_{D-A}$	2.83	-3.75E-3	T_2	^3LE_A	2.45	-
T_2	$^3CT_{D-A}$	3.08	-	T_3	^3LE_D	2.50	-
S_2	$^1CT_{D-A}$	3.08	-4.24E-4	T_4	^3LE_A	3.54	-
T_3	$^3CT_{D-A}$	3.24	-	S_1	$^1CT_{D-A}$	3.65	-7.11E-4
S_1 Geometry							
B3LYP				OT			
State	Nature	ΔE/eV	g_{lum}	State	Nature	ΔE/eV	g_{lum}
T_1	$^3CT_{D-A}$	2.42	-	T_1	$^3CT_{D-A}$	2.98	-
S_1	$^1CT_{D-A}$	2.43	-0.0013	T_2	$^3CT_{D-A}$	3.03	-
T_2	$^3CT_{D-A}$	2.99	-	S_1	$^1CT_{D-A}$	3.05	-0.004
T_3	$^3CT_{D-A}$	3.00	-	T_3	^3LE_D	3.28	-
S_2	$^1CT_{D-A}$	3.01	-0.0018	T_4	^3LE_A	3.37	-
T_1 Geometry							
B3LYP				OT			
State	Nature	ΔE/eV	g_{lum}	State	Nature	ΔE/eV	g_{lum}
T_1	$^3CT_{D-A}$	2.42	-	T_1	$^3CT_{D-A}$	2.98	-
S_1	$^1CT_{D-A}$	2.43	-0.009	T_2	$^3CT_{D-A}$	3.03	-
T_2	$^3CT_{D-A}$	2.99	-	S_1	$^1CT_{D-A}$	3.05	-0.004
T_3	$^3CT_{D-A}$	3.00	-	T_3	$^3CT_{D-A}$	3.28	-
S_2	$^1CT_{D-A}$	3.01	-0.002	T_4	$^3CT_{D-A}$	3.37	-

TABLE 6.9: Energies and g-factors from the two studies, B3LYP (left) and OT (right), for emitter **E**, for the optimised S_0, S_1 and T_1 geometries.

of the emitter in the ground and excited S_1 state were performed. These were then sampled using B3LYP and the OT LC-BLYP functional. The dynamics were run for 10ps and for each geometry that was sampled the dissymmetry was calculated.

Figure 6.10 shows the distribution of the g-factors achieved from the structures sampled from the MD. This shows that fluctuations of the structure lead to a distribution of g_{lum} which oscillates either side of 0. The results shows that once an average of the g_{lum} for each geometry was taken the resulting dissymmetry emitted the emitter was 0 for both the ground and excited state geometries. Consequently, while at a single geometry, the dissymetry calculated was non-zero, we would expect these to exhibit close to zero g_{lum}.

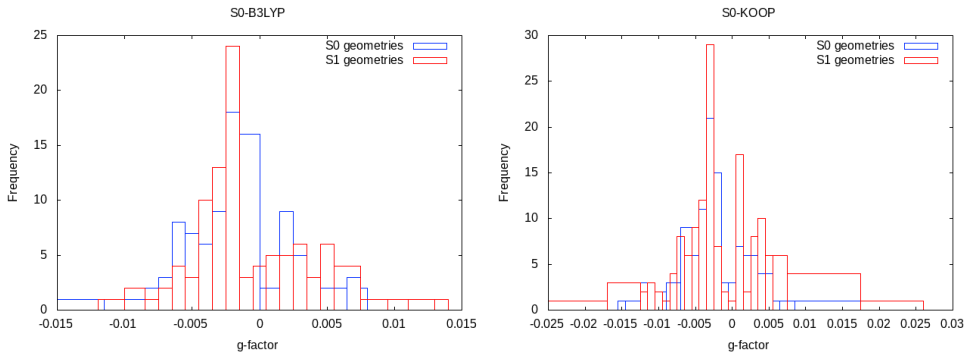

FIGURE 6.10: Distribution of g-factors from MD sampling of emitter **E** for the B3LYP study (top) and OT study (bottom). The geometries in the S_0 is shown in blue and the geometries in the S_1 state are shown in red.

As described previously, when using the D-A design for building TADF materials the aim is to create orthogonality between the D and A parts of the molecule. The purpose of this is to localise the HOMO and LUMO densities on separate parts of the molecule to create the CT character. Therefore, minimising the ΔE_{ST} and encouraging efficient ISC. It is clear from the results above that if the molecule remained static in this optimised orthogonal geometry, the emitter displays both CT TADF character and reasonable dissymmetry emission. However, this static description of emission is unrealistic and therefore the MD picture is most appropriate. With the results from the MD study displaying a zero dissymmetry it is important to consider the implications of this result. This observation is consistent with recently published experimental results [147], which demonstrated that dynamics around the D-A bond is responsible for changing the sign of the dissymmetry and ultimately quenching CP emission characteristics.

To increase the dissymmetry of these molecules it would be necessary to increase the distortion of the system around the D-A bond. This would allow for more intense dissymmetry in the emission, but the outcome of this would incur detrimental effects on the TADF emission, it would counteract the efforts to encourage the orthogonal geometry. Increased distortion will

increase the singlet-triplet gap. When building emitters for TADF there is a clear balance that must be struck between the singlet-triplet energy gap and the radiative rate. To integrate CPL properties into the existing design strategy for TADF emitters this balance would be further complicated to include the increased distortion for CPL. If the balance was struck there is also an intrinsic limit for the magnetic transition dipole moment in small molecules that will hinder the capacity of the molecule to emit both TADF and CPL.

6.5 Conclusions

To design effective new emitters being able to accurately model the excited states and their properties is critical. This allows for better prediction of efficient designs for future emitters. As described above, many TADF emitters are built in the D-A form, however, this design often results in the formation of CT states. Therefore, there are both long-range and short-range interactions that need to be described. DFT provides a very good description of short-range interactions, however does not provide such an accurate description of long-range effects. To improve this description of states that exhibit a small exchange overlap the TT and OT approaches can be utilised.

This work began by examining two methods that had the potential to improve the description of the CT state that is commonly exhibited in TADF emitters. This character of state is poorly described by traditional DFT methods as long-range interactions are not effectively described. When designing new emitters it is vital that one is able to effectively model the excited states, and thus predict or explain the emission of the chromophore. With the ever-increasing need for new, more efficient TADF emitters for applications in display and lighting technology, methods that improve computational modelling are paramount. The methods that were studied, namely, OT[148] and the TT method[139]. They were applied to study the excited states of two typical D-A TADF emitters, PTZ-$DBTO_2$ and TAT-$3DBTO_2$. Both the TT method and OT method were effective when modelling CT states when there was a small exchange overlap. In both cases similar values for ω were reported. In the case of the CT states, the states are single particle properties that depend mostly on the energy gap between the HOMO and LUMO. However, both methods showed a geometry dependence, with the TT method showing a greater geometry dependence, especially when there are close lying states that could exchange along the reaction coordinates. This is due to the TT method accounting for effective electron-hole interactions explicitly, therefore smaller range separated parameters are required and thus a standard hybrid exchange and correlation parameters can be used to describe these states.[8]

Furthermore, Koopmans OT approach was then applied to a selection of CP-TADF emitters. The first emitters that were studied had a chiral appendage that was added to a D-A TADF emitter, therefore, it was expected

that the improved description of the long-range interactions by the OT approach will provide more accurate energies and *g*-factors for the emitters. The *g*-factors calculated for emitter **4** showed good agreement with those reported in the literature.[132] However, the impact on the energies of the OT approach was seen to a lesser extent for the *g*-factors, this could be due to their relatively small size.

Overall, the emitters displayed relatively small *g*-values, when the frontier orbitals were considered, they showed that the exciton was not delocalised over the chiral part of the chromophore. Therefore, it is expected that this is the limiting factor when applying this architecture to the emitters. Moreover, the final emitter included the chiral perturbing unit closer to the active chromophore and therefore it played a larger role in the emission process. Despite showing promise in the initial studies, displaying both close lying S_1 and T_1 and some chiroptical response, the Fuchter Group, who obtained the photophysical measurements, saw no chiroptical response. Therefore, the study looked to explain this discrepancy. The MD study showed that there was a broad spread of disymmetry of emission. This was due to the fine-motion of the system throughout the emission process. For efficient TADF emission, some vibration of the emitter is required to allow the emission to occur, however, this motion is detrimental to the chiroptical emission. There is also an inherent limit on the amount of chiroptical response that can be seen from a small molecule, therefore it is unlikely that this design of CP-TADF emitter in its current phase will show strong chiroptical responses necessary for applications in display technology. For that reason, this thesis moves to look at larger systems that bypass this inherent limit.

Chapter 7

CPL beyond a Single Molecule

7.1 Introduction

Chirality is a fundamental symmetry property that can be found in the natural world, it can be used to describe any object that is non-superimposable on it's mirror image, one example is the left and right human hands. Chirality can also be seen on a molecular scale, and has recently been harnessed for applications in display technology. Molecular chirality is of significant interest in optoelectronic applications, such as organic light-emitting diodes (OLEDs) and organic photodetectors, where the use of a chiral material in the active layer enables the emission or detection of circularly polarised (CP) light, respectively [20]. If direct emission of CP light can be harnessed, new OLED devices could be developed with improved device efficiencies and lifetimes.[57, 149]

Interest in the development of chiral organic materials for CP-OLEDs [150] has led to a variety of approaches being pursued. These can be broadly grouped into two classes; small-molecule emitters, [60, 61, 57, 151] and polymer-based emitters [63, 64, 149, 152, 153]. Polymer-based emitters are the focus of this Chapter. Early work in this area began with synthesising emitters with pendent chiral side-chains added to an achiral conjugated polymer backbone. One example of a successful attempt of this design architecture is a chiral-substituted poly(*p*-phenylenevinylene) (PPV) with g-factors in the region of 10^{-3}.[49] Since then, there have been emitters with similar architecture with reported g-factors of up to 0.35.[149] Interest in the influence of the pendent chiral side chains then followed, it came to light that these side chains were working to align the polymer backbone into a chiral arrangement.[154, 155] With this knowledge another way to reach this induced chirality was considered. Here a chiral small-molecule dopant is blended with a conventional achiral light-emitting polymer (LEP). In this case, the chiral small-molecule dopant acts like the side-chains, and induces the desired polymer architecture. This method is highly translatable and benefits from negating the need for bespoke polymer synthesis.[149] This approach has been applied to some chiral architectures such as biaryl compounds,[149] chiral solvent mixtures,[152] and, polysaccharides[64]. Yang *et al.* reported promising g-factors ($|g_{EL}|$=0.27 and $|g_{PL}|$=0.5) for a LEP blended with a chiral

small-molecule dopant[149], furthermore, Lee *et al.* reported concurring results using the same LEP and an commercially available chiral small-molecule dopant and an additional alignment layer.[153] Recently, Wan *et al.* have shown that this synthesis can be used to build successful CP-OLEDs with control over the handedness of the light emitted depending on the thickness of the thin-film.[64]

Inducing CP electroluminescence from achiral polymers using small molecule chiral dopants has been shown to be a elegant way to develop state of the art OLED's.[149]Thus, understanding the mechanism of emission from these chiral structures, as well as providing a reliable way to model potential systems is a crucial part of the development of such devices. This work uses fluorene-based polymeric systems, namely poly(9,9-dioctylfluorene) (PFO) and the donor-acceptor type copolymer poly(9,9-dioctylfluorene-*alt*- benzothiadiazole) (F8BT), to study the influence of the physical and chemical structure on the chiroptical response. These polymeric systems have previously been reported by Wan *et al.*[64] and have been proved to be an efficient medium for CP-OLEDs.

Currently, organic systems generating the largest dissymmetric response in the solid state (g-factors up to $\sim$1) are conjugated polymers, especially amongst the polyfluorene class [152]. It has been proposed that this strong CP luminescence occurs due to structural chirality [63, 154, 153]. However, recent works [64, 156] have indicated that long-range structural chirality only dominates the chiroptical response when an alignment layer is used to template molecular packing of polymer chains at or beyond the mesoscale. Highly dissymmetric emission from non-aligned thin polymer films (*i.e.*, those where the film thickness is considerably less than those at which this structural chiroptical phenomena manifest) suggests that intrinsic CP emission may play a significant role.[157, 156] Thus, the intermolecular interactions between the polymer chains are of great interest. This work models this long-range structural chirality by introducing dimers of the polymer systems.

7.2 Computational Details

Planar structures of the models of F8BT and PFO polymers, shown in Figure 7.1, were optimised using DFT(B3LYP) and a Def2-SVP basis set [134] as implemented within the ORCA quantum chemistry package [158]. Naturally, the polymer systems are large, particularly when considering the computational expense of the methods being implemented. Therefore, to reduce the computational expense of the quantum mechanical simulation the C_8H_{17} side chains were replaced by methyl groups for both systems. Following optimisation, the structures were manipulated as required to assess the twist angle between adjacent repeat units and the number of monomers (n). The former

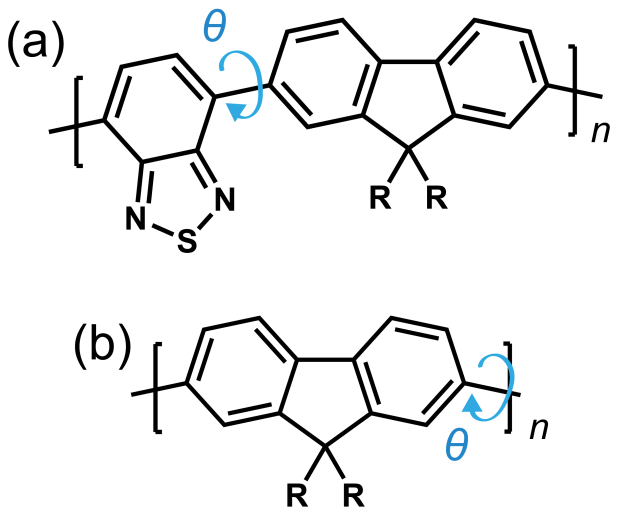

FIGURE 7.1: Structures of the simplified models of (a) F8BT and (b) PFO. R are C_8H_{17} side chains, however herein, R represents methyl groups. n represents the number of repeat units and the arrows indicate the twist angle (θ) between adjacent repeat units.[9]

was performed using the Avogadro software [134]. To generate the dimers, the centre of mass for each single polymer chain was calculated, the centre of mass of the second polymer chain was then added at a distance d and at an angle ϕ from the centre of mass of the original polymer chain.

Throughout this work, all calculations of the dissymmetry were performed using TDDFT within the approximation of the CAM-B3LYP [128] exchange and correlation functional and a Def2-SVP basis set [134] as implemented within the ORCA quantum chemistry package [158]. The calculations of the electric ($\boldsymbol{\mu}$) and magnetic ($\boldsymbol{m}$) transition dipole contributions used the length representation and the origin independent approach as described in References [68, 159]

7.3 Theory

The CP emission from the polymer-based emitters can be described by the dissymmetry of the emitted light (g-factor). The g-factor can determined by the coupling between the electric ($\boldsymbol{\mu}$) and magnetic ($\boldsymbol{m}$) transition dipole moments [67], and can be expressed as:

$$g = \frac{4R}{D} = \frac{4|\boldsymbol{\mu}_{ij}||\boldsymbol{m}_{ij}|\cos(\tau)}{|\boldsymbol{\mu}_{ij}|^2 + |\boldsymbol{m}_{ij}|^2} \tag{7.1}$$

where R is the rotatory strength and D is the overall transition strength composed of the sum of $|\boldsymbol{\mu}_{ij}|^2$ and $|\boldsymbol{m}_{ij}|^2$ and, i and j refer to the initial and final states involved in the electronic transition. Finally, τ is the angle between

$\boldsymbol{\mu}$ and $\boldsymbol{m}$. It is important to note that Equation 7.1 is valid for the g-factors associated with both absorption (g_{abs}) and emission (g_{lum}).[67] Fundamentally, the difference between the two is that g_{abs} describes the dissymmetry of thermally equilibrated ground state, while g_{lum} reflects the structure of the emissive state. Therefore, very similar g_{abs} and g_{lum} values can be expected when there is little configurational reorganisation between the ground and excited states.[67]

Throughout this work, the dissymmetry was calculated for the lowest singlet excited state using Equation 7.1. For the dimers, both the excitonic split states are included as the weakly coupled nature of the dimers means that the splitting between the two Davydov bands is <0.3 eV. The relative contributions of the upper (S_2) and lower (S_1) states is governed by a Boltzmann distribution according to:

$$\frac{Int(S_2 \rightarrow S_0)}{Int(S_1 \rightarrow S_0)} = \frac{f(S_2 \rightarrow S_0)}{f(S_1 \rightarrow S_0)} \cdot \exp\left(-\frac{\Delta E_{S_2-S_1}}{k_b T}\right) \tag{7.2}$$

where f is the oscillator strength associated with each state and $\Delta E_{S_2-S_1}$ corresponds to the Davydov splitting.

The size of a typical molecule is much smaller (tens of Angströms) than the wavelengths of the interacting light (hundreds of nanometres) in the visible light regime. Accordingly, the exponential operator responsible for the spatial term of the radiation field, $\exp(i\mathbf{k}\cdot\mathbf{r})$, when expanded as a Taylor series [68]

$$\exp(i\mathbf{k}\cdot\mathbf{r}) = 1 + i(\mathbf{k}\cdot\mathbf{r}) - \frac{1}{2}(\mathbf{k}\cdot\mathbf{r})^2 + \cdots \tag{7.3}$$

may be truncated at zeroth order corresponding to the electric dipole approximation. First-order contributions, *i.e.* the electric quadrupole and magnetic dipole terms, only become significant for electric dipole forbidden transitions or when $kr > 1$ [68]. The latter is achieved either at high photon energies or if the exciton size approaches the wavelength of the light.

The validity of the electric dipole approximation on the molecular scale implies that the $\boldsymbol{\mu}$ is typically around three orders of magnitude larger than $\boldsymbol{m}$ [68]. When considering transitions allowed within the electric dipole approximation, Equation 7.1 indicates that g-factors are limited to values of $\sim 10^{-3}$ [24]. Larger dissymmetric responses can be achieved for molecules that make use of electric-dipole forbidden transitions, including chiral lanthanide complexes ($g \sim 1.4$) [160]. However, owing to their small $\boldsymbol{\mu}$, they typically demonstrate low emission cross sections, which results in luminescence quantum yields too low for display applications. While efforts continue to address the trade-off between luminescence quantum yield and dissymmetry [24], it remains a challenge to identify highly emissive organic molecules with excellent CP characteristics.

7.4 Results

7.4.1 Single Polymer Chains

To explore the origins of the chrioptical response of the polymer thin films it is crucial to first consider the properties of the isolated polymer chains. This chapter considers influence of chemical composition, intramolecular twist angle (θ) between adjacent repeat units and the number of monomers (n) a single oligomer chain is made up of on the g-factor.

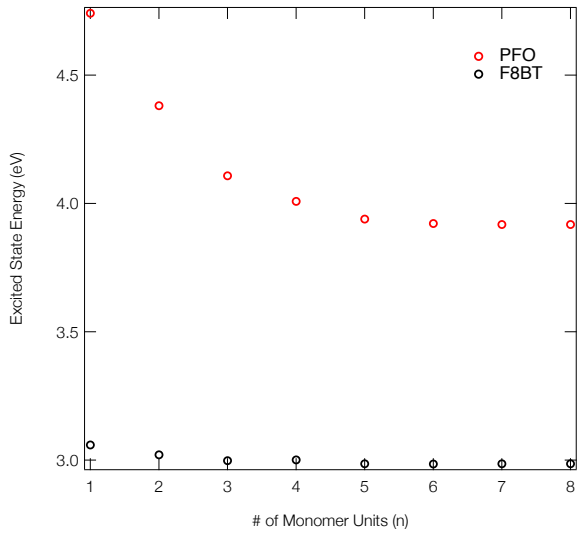

FIGURE 7.2: Energy of the S_1 state (in eV) for PFO (red) and F8BT (black) as a function of the number of repeat units.[9]

The lowest excited state of PFO corresponds to the $\pi \rightarrow \pi^*$ transition. The calculated S_1 state of an isolated oligomer (θ= 40°, n >4) is 318 nm, as shown in Figure 7.2. For F8BT (θ= 40°, n >3), the lowest transition exhibits a charge-transfer character between the F8 and BT units and the calculated S_1 state of the isolated oligomer is 427 nm, as shown in Figure 7.2. These are in reasonable agreement with the lowest absorption bands, as reported by Wade *et al.*, 375 nm and 475 nm, measured for PFO and F8BT, respectively [161].

Figure 7.3a shows the g-factor, calculated using Equation 7.1, of the S_1 state of isolated PFO and F8BT oligomers as a function of n with a fixed θ= 40°, close to the optimised twist angle for F8BT [64] and the glassy-phase PFO [162]. In both cases, the g-factor initially increases before a plateau is reached at n=3 and n=5 for PFO and F8BT, respectively. This behaviour bears some resemblance to the work of Greenfield *et al.* [163], who reported a plateau associated maximum length over which the exciton can delocalise for a given configuration. Here the plateau is reached earlier for PFO (n= 3) than F8BT

n	PFO		F8BT	
	$\boldsymbol{\mu}$	$\boldsymbol{m}$	$\boldsymbol{\mu}$	$\boldsymbol{m}$
1	1.244	0.116	3.901	0.342
2	3.840	0.187	4.773	0.685
3	5.266	0.293	5.823	1.278
4	6.292	0.419	6.656	1.435
5	7.203	0.642	7.111	1.563
6	7.768	0.818	7.694	1.664
7	7.928	1.527	8.173	1.759
8	8.165	2.563	8.421	2.292

TABLE 7.1: The electric and the magnetic transition dipole moments for PFO and F8BT as a function of the number of repeat units (n). Atomic units are used throughout. A fixed twist angle (θ=40°) was used throughout.

owing to a larger exciton binding energy of PFO compared to F8BT (F8BT =0.2 eV [64], PFO=0.3 eV [164]). For the non-planar polymers studied in the present work, the enhanced delocalisation of F8BT [64] means that kr for F8BT will be larger than that of PFO. This results in an increase of $\boldsymbol{m}$ relative to $\boldsymbol{\mu}$, which can be seen in the decreasing μ^2/m^2 ratio, shown in Figure 7.3c, Table 7.1, and the larger predicted g-factors.

Figure 7.3b shows the g-factor as a function of θ for PFO and F8BT 2-mers (*i.e.*, n = 2). In both cases the g-factor increases with the magnitude of θ, and its sign is determined by direction, which indicates that the handedness/sign of the CP response can be controlled by the direction of the cumulative twist along the polymer backbone. The impact of θ is more pronounced for PFO for two reasons. Firstly, because the ratio μ^2/m^2 is considerably smaller in PFO for θ >30° (Figure 7.4a, Table 7.2) and secondly, because, the angle τ between $\boldsymbol{\mu}$ and $\boldsymbol{m}$ (Figure 7.4b) deviates more from 90°. In general, $\boldsymbol{\mu}$ and $\boldsymbol{m}$ decreases as θ increases and this reduction is greater for F8BT as the coupling strength between the (intrachain) donor and acceptor decreases as θ approaches orthogonality. This leads to a larger relative decrease in $\boldsymbol{m}$ compared to $\boldsymbol{\mu}$ and therefore an increase in the ratio μ^2/m^2, as shown in Figure 7.4a. Whilst this is unfavourable for achieving high g-factors, it is offset by the increase in cos(τ). The same is not observed for PFO as we are considering the π-π^* transition of the homopolymer. As θ increases, the delocalised exciton exhibits an increased $\boldsymbol{m}$ compared to $\boldsymbol{\mu}$, reflected in the ratio μ^2/m^2, as shown in Figure 7.4a. The angle τ between $\boldsymbol{m}$ and $\boldsymbol{\mu}$ increases, which supports the enhancement of the g-factor.

Angle	PFO		F8BT	
	$\boldsymbol{\mu}$	$\boldsymbol{m}$	$\boldsymbol{\mu}$	$\boldsymbol{m}$
-70	5.326	0.470	4.036	0.327
-60	6.689	0.345	4.623	0.578
-50	6.036	0.236	5.055	0.820
-40	6.209	0.188	5.392	1.093
-30	6.413	0.123	5.765	1.360
-20	6.505	0.085	5.978	1.564
-10	6.603	0.072	6.099	1.695
0	6.783	0.064	6.142	1.740
10	6.603	0.072	6.096	1.694
20	6.505	0.085	5.974	1.563
30	6.413	0.123	5.767	1.360
40	6.209	0.188	5.391	1.093
50	6.036	0.236	5.062	0.822
60	6.689	0.345	4.623	0.579
70	5.326	0.470	4.033	0.326

TABLE 7.2: The electric and the magnetic transition dipole moments for PFO and F8BT 2-mers (n=2) as a function of the twist angle between the monomer units.

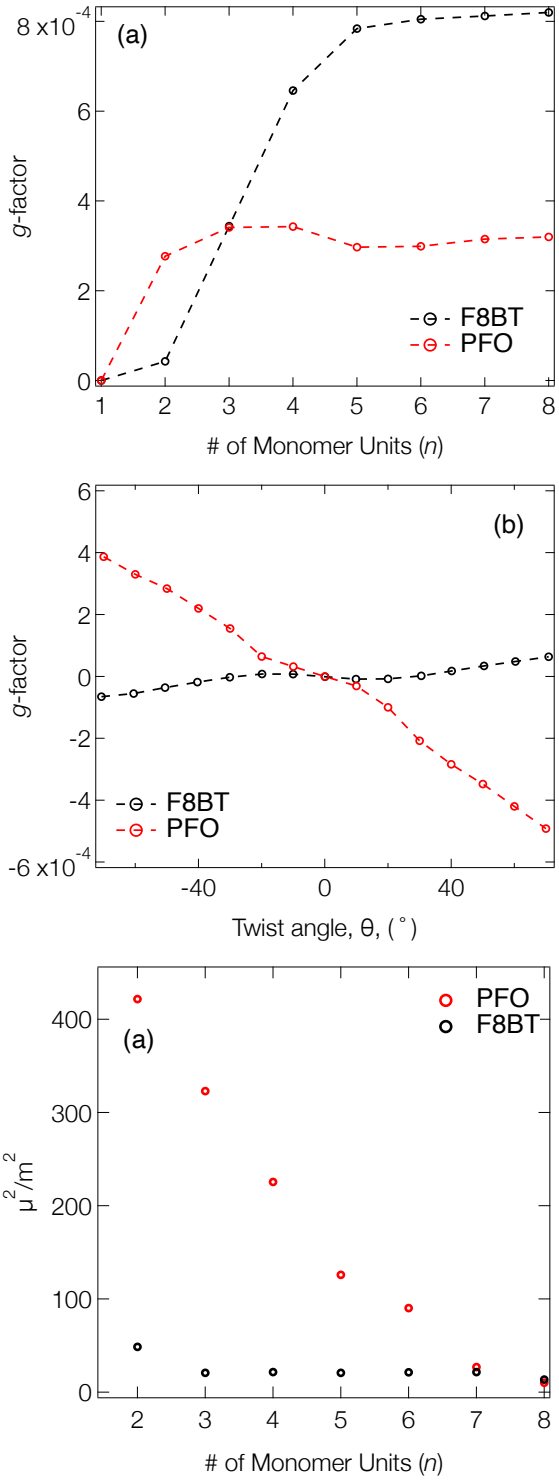

FIGURE 7.3: (a) g-factor of the S_1 state as a function of the number of monomer units (n) for PFO (red) and F8BT (black) oligomers. A fixed twist angle (θ=40°) was used throughout. (b) g-factor as a function of θ for PFO (red) and F8BT (black) 2-mers (n=2). The dashed line between the points are a guide for the eye. (c) The ratio between the electric and magnetic transition dipole moments, μ^2/m^2 for PFO (red) and F8BT (black) as a function of the number of repeat units. [9]

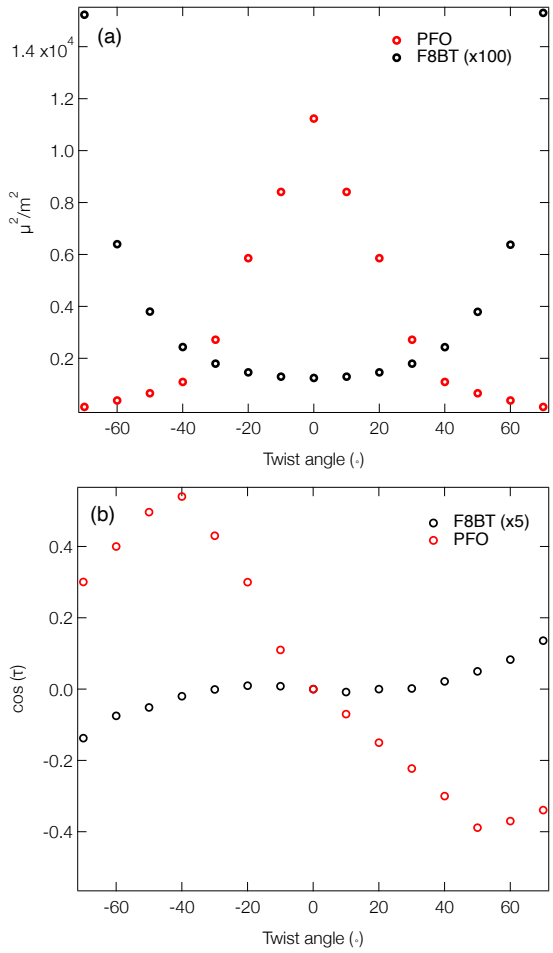

FIGURE 7.4: (a) The ratio between the electric and magnetic transition dipole moments, μ^2/m^2 for PFO (red) and F8BT (black) as a function of the twist angle between the monomer units. (b) $\cos(\tau)$, where τ is the angle between the electric and magnetic dipole moments, as a function of the twist angle between each monomer units for PFO (red) and F8BT (black).[9]

7.4.2 Interchain Coupling of Dimers

The above examples have shown how, for isolated oligomers, the g-factor depends on the extent of exciton delocalisation, which is ultimately related to the validity of the dipole approximation (Equation 7.4). Despite increasing kr and a larger contribution from the magnetic transition dipole moment, the calculated g-factors still do not exceed 10^{-3}, *i.e.* values that are consistent with molecular-level mechanisms and considerably smaller than dissymmetry factors reported for chiral polyfluorene thin films [64, 161]. Instead of isolated oligomers, we next consider the impact of inter-chain coupling on the g-factors.

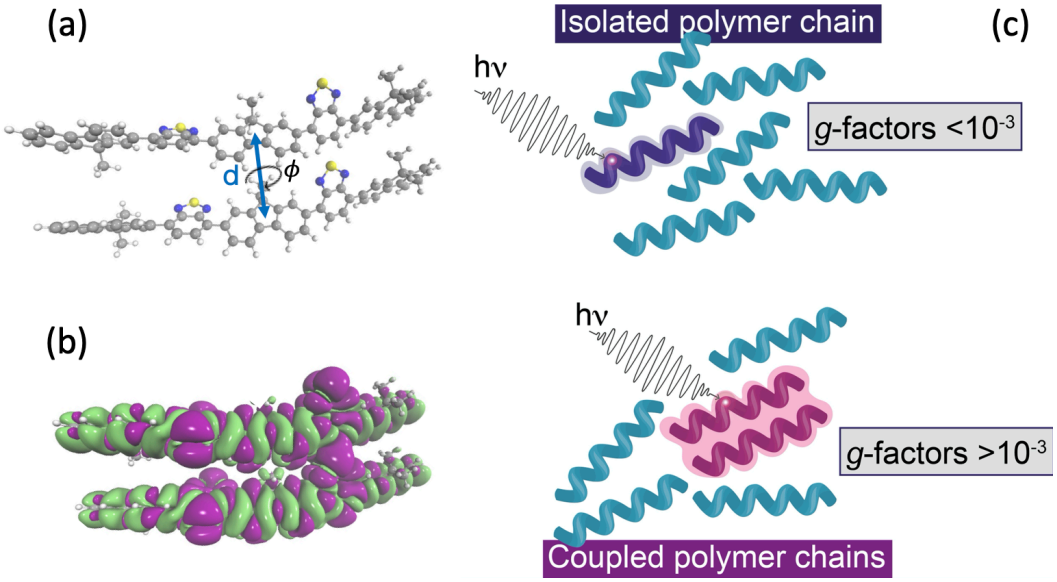

FIGURE 7.5: (a) Schematic of two polymer chains and the coordinates (d and ϕ) manipulated in Figure 7.6. (b) Density difference of the lowest exciton of a F8BT dimer model illustrating the electron density delocalised over the two chains. (c) Schematic of the effect of interacting polymer chains on the electric and magnetic transition dipole moments.[9]

Figure 7.6a shows the dissymmetry of coupled F8BT and PFO dimers, where the geometry is determined by the the centre-of-mass separation (d) and and mutual orientation (ϕ) of the two oligomers, as shown in Figure 7.5a. Initially, we fixed both the mutual orientation of the oligomers (ϕ=10°) and the intrachain twist angle (θ=40°). It is immediately evident that exciton delocalisation over two polymer chains, illustrated in Figure 7.5b, leads to an increase in the calculated dissymmetry. At short distances (d <7 Å) g-factors of ∼0.1 and ∼0.03 are observed for PFO and F8BT, respectively. The g-factor decreases as a function of d^{-3} (dashed line in Figure 7.6a) reflecting the decrease in exciton coupling (V) with distance. Figure 7.6b shows the dissymmetry of the F8BT or PFO 2-mers as a function of ϕ, the angle between

the oblique chains, as shown in Figure 7.5b. This shows that for ϕ=0°, the dissymmetry is similar to that of the isolated oligomers. However, as the angle increases, a large increase in the dissymmetry is observed as the coupling between the oligomers becomes which reaches a maximum at ϕ=10°. After this the dissymmetry decreases as $\boldsymbol{\mu}$ increases and $\boldsymbol{m}$ decreases. These calculations demonstrate that like θ for the isolated polymers, the direction of ϕ can control the sign of the g-factor and overall only small angles are preferred to maximise the g-factor. Figures 7.7 and 7.8 confirms that the individual polymer chains did in fact form dimers. The spectra show typical profiles of dimer systems, thus the associated results can be confidently assigned to a dimer system.

To understand the origin of the increase in dissymmetry shown in Figure 7.6 we turn to the well-established exciton chirality model (ECM) [165, 166], where the rotatory strength (R) for a dimer of coupled excitonic states can be defined as:

$$R = \pm\frac{1}{2}\pi\sigma\boldsymbol{d_{kl}}\cdot(\boldsymbol{\mu}_k\times\boldsymbol{\mu}_l)+\frac{1}{2}Im\{(\boldsymbol{\mu}_k\pm\boldsymbol{\mu}_l)\cdot(\boldsymbol{m}_k\pm\boldsymbol{m}_l)\} \tag{7.4}$$

where $\boldsymbol{d_{kl}}$ is the distance vector between the two individual chromophores k and l, and σ is the transition energy. For the majority of coupled chromophores, one assumes that terms involving $\boldsymbol{m}$, generally referred to as $\boldsymbol{\mu}$-$\boldsymbol{m}$ terms, are negligible because of the magnetically forbidden nature of their transition; therefore the rotatory strength can be evaluated simply by considering the coupled $\boldsymbol{\mu}$ ($\boldsymbol{\mu}$-$\boldsymbol{\mu}$, first term in Equation 7.4). Using this approach, the maximum value of dissymmetry is $g = \pi\sigma d_{kl}$ [167]. In the case of PFO (S_1=318 nm), the g-factor would only reach 0.1, as shown in Figure 7.6, if d_{kl} =100 Å, which is clearly unrealistic. This represents the breakdown of the standard ECM and emphasises that the consideration of $\boldsymbol{m}$ for conjugated polymer systems could be important to rationalise the magnitude of the dissymmetry observed. To explore this further we compare R evaluated using each component of the ECM model (Equation 7.4) with those calculated using TD-DFT for a coupled dimer of a PFO 2-mer with d=6 Å, θ=40° and ϕ=10°. R calculated using Equation 7.4 is 608×10^{-40} esu^{2}cm^2, which is in good agreement with the TDDFT calculation of 625×10^{-40} esu^{2}cm^2. Importantly, the relative strengths of $\boldsymbol{\mu}$-$\boldsymbol{\mu}$ term (368×10^{-40} esu^{2}cm^2) and $\boldsymbol{\mu}$-$\boldsymbol{m}$ (240×10^{-40} esu^{2}cm^2) highlights that the $\boldsymbol{\mu}$-$\boldsymbol{m}$ coupling is important for evaluating the total rotatory strength and the g-factors predicted by the coupled dimer models. When θ=0° (*i.e.* a planar configured polymer backbone), R (Equation 7.4) is 853×10^{-40} esu^{2}cm^2. However, in contrast to the case of twisted polymer backbones, the contribution of the $\boldsymbol{\mu}$-$\boldsymbol{\mu}$ term (818×10^{-40} esu^{2}cm^2) dominates over $\boldsymbol{\mu}$-$\boldsymbol{m}$ (35×10^{-40} esu^{2}cm^2). This highlights the role of the $\boldsymbol{\mu}$-$\boldsymbol{m}$ term in the generation of high g-factors in non-planar polymer systems.

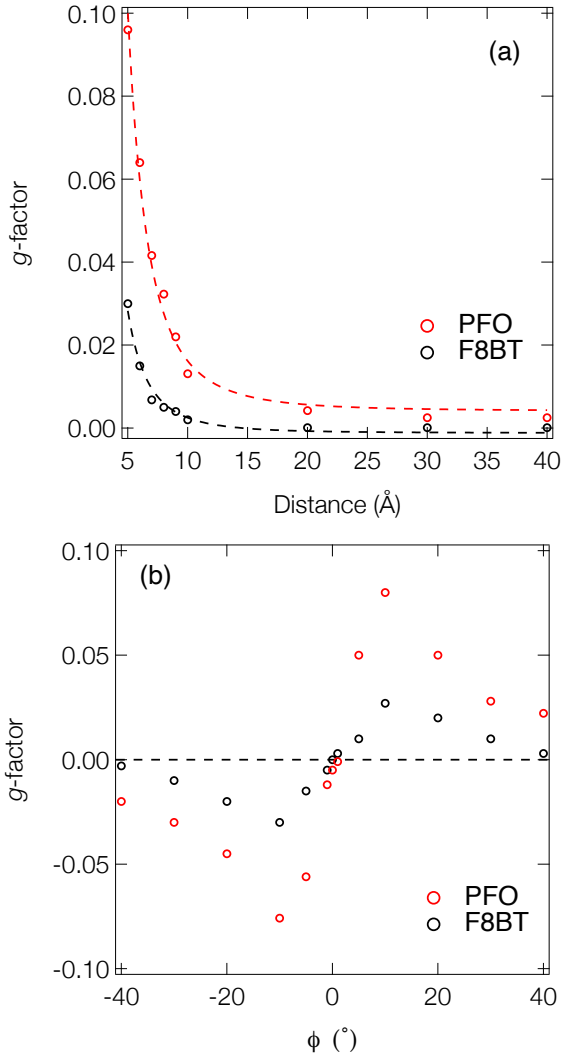

FIGURE 7.6: a) g-factor as a function of the distance between the centre-of-mass of each chain in a dimer of PFO (red) and F8BT (black) 2-mers (n=2, θ=40°). The angle between the two polymer chains in the dimer (ϕ) was fixed at 2°. The dashed line is a fit using d^{-3} illustrating a decay in the dissymmetry consistent with a reduction in the exciton coupling. (b) g-factor as a function of the angle (ϕ) between the two polymer chains (n=2, θ=40°) in the dimer. The distance between the 2-mers was fixed at 6 Å.[9]

Figure 7.6 shows the effect of interacting polymer (2-mer) chains on the magnitude of the g-factor. It is worth emphasising that this limited size may influence the dissymmetry, as it does the excited state energies shown in Figure 7.2. Consequently, Figure 7.9 shows the dimer calculation (d=6 Å, θ=40° and ϕ=2°) as a function of the number of monomer units (n) for PFO. This demonstrates that as n increases, the g-factor decreases until reaching convergence of ∼0.02 for n >4. It is noted that this convergence in very similar to that observed in Figure 7.2. The number of atoms required for a similar

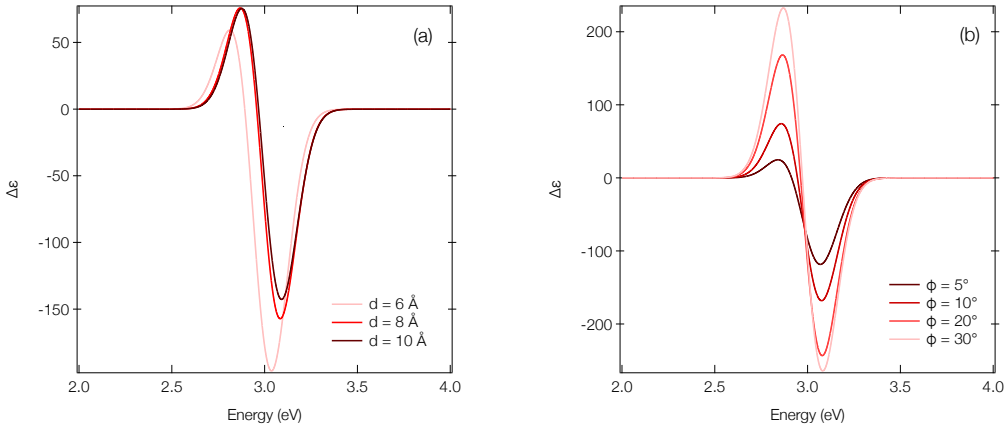

FIGURE 7.7: $\Delta\epsilon$ for the lowest exciton couplet of the F8BT model as a function of the (a) distance (d, n=2, θ=40° and ϕ=10°) and (b) angle (ϕ, d=6 Å, n=2, θ=40°) between the monomer chains. Spectra broadened using Gaussian function 0.25 eV FWHM.[9]

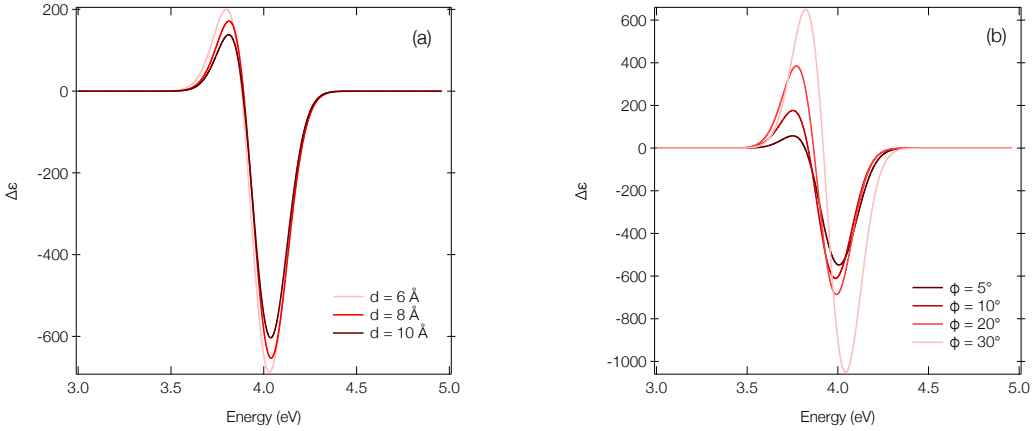

FIGURE 7.8: $\Delta\epsilon$ for the lowest exciton couplet of the PFO model as a function of the (a) distance (d, n=2, θ=40° and ϕ=10°) and (b) angle (ϕ, d=6 Å, n=2, θ=40°) between the monomer chains. Spectra broadened using Gaussian function 0.25 eV FWHM.[9]

Angle	PFO	F8BT
-40	0.126	0.031
-30	0.160	0.062
-20	0.194	0.101
-10	0.232	0.122
-5	0.248	0.193
-1	0.258	0.213
0	0.260	0.215
1	0.262	0.214
5	0.262	0.182
10	0.248	0.116
20	0.196	0.090
30	0.202	0.059
40	0.160	0.030

TABLE 7.3: The coupling potential between the excitonic states (V) in eV for PFO and F8BT as a function of the angle (ϕ) between the monomer chains.

Distance	PFO	F8BT
5.0	0.282	0.213
6.0	0.234	0.154
7.0	0.190	0.112
8.0	0.156	0.094
9.0	0.130	0.080
10.0	0.128	0.070
20.0	0.030	0.024
30.0	0.012	0.010

TABLE 7.4: The coupling potential between the excitonic states (V) in eV for PFO and F8BT as a function of the distance (d) between the monomer chains.

study of F8BT make it very challenging and as the convergence effect show in Figure 7.2, is weaker than PFO and so a similarly small effect is expected for the g-factor.

7.5 Conclusions

Understanding the relative contributions of local short-range electric-magnetic coupling and longer-range structural chirality is crucial for the rational design of new materials that exhibit an intense chiroptical response. This work demonstrates that the extension of the exciton over nearby polymer chains

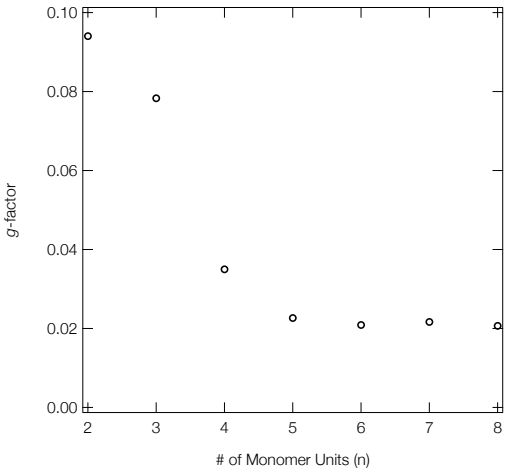

FIGURE 7.9: g-factor of the S_1 state as a function of the number of monomer units (n) for a dimer of PFO (black). d=7 Å, θ=40° and ϕ=2°. Reproduced with permission from Royal Society of Chemistry.[9]

is critically important for enhancing the dissymmetry. By exploiting the intrinsic magnetic transition dipole moment (and therefore invoking $\boldsymbol{\mu}$-$\boldsymbol{m}$ coupling) arising from the helically configured polymer backbones it is possible to significantly increase the dissymmetry of dimer systems. This model may not hold in polymers which adopt a planar structure in the aggregate state as they are more likely to have negligible transition magnetic dipoles [168], however when strong interchain excitonic coupling dominated, as recently shown in thin films of PFO [157] exceptional chiroptical response can still be achieved, but in this case it would be dominated by the $\boldsymbol{\mu} - \boldsymbol{\mu}$ coupling, as the electric-magnetic coupling is negligible.

Finally, it should be noted that the present work does not consider further exciton delocalisation over a larger stack (*e.g.* trimers, tetramers), nor how the delocalisation would be impacted by conformational and environmental disorder, which are likely to play a role for longer polymer chains and excitonically coupled systems comprising a larger number of chains. In addition, it is important to recognise that the polymer thin films optimised for CP-OLEDs [169] are only weakly ordered and therefore the dissymmetry will be an average over multiple orientations and configurations which emit in the film. Given that reducing the inter-chain coupling significantly quenches the dissymmetry, it is possible that the overall chiroptical response would be reduced if all sites were equally likely to interact with the CP light. However, this inter-chain coupling modulates both the energy and oscillator strengths of the states involved meaning that not all sites are equally likely to absorb/emit light. To understand this, further investigations using molecular dynamics is essential and will be the focus of future work.

Chapter 8

Conclusion

8.1 Conclusion and Future Work

Display technology is a mainstay of everyday life in the western world. With the huge increase in employees working from home due to the Covid-19 pandemic, there is an ever increasing need for affordable, efficient displays on smartphones, laptops and televisions. The most recent state-of-the-art smartphone designs have integrated OLEDs, despite this success, there remains a need to further innovative, especially with respect to improving the energy efficiency and sustainability of current technologies. OLEDs have proved to be the state-of-the art technology within the displays and lighting sector, this can be seen in the successful integration of OLED technology into the majority of smartphone designs. To continue this success it is important to continually innovate the technology. One focus of the innovations is improving the energy efficiency and sustainability of the existing technology. With the imminent integration of 5G technology in smartphones, a critical consideration for energy efficient devices is the minimisation of the power consumption from the OLED technology.

Improvement of OLED display efficiency beyond device fabrication can be achieved in two ways. Firstly, by improving the IQE of the emissive materials used within the OLED device. Statistically, only 25% of excitons formed within the emissive material are singlets and can radiatively relax via fluorescence. The remaining 75% are triplet (dark) excitons which do not emit in conventional fluorescent materials and therefore their energy is lost to heat. Thus, mechanisms that can allow the 'capture' of triplets increase the IQE of an OLED emitter. Secondly, by bypassing anti-glare filters. OLED display technologies require anti-glare filters to improve viewing contrast when routinely used under conditions of high ambient light. Anti-glare filters use a double layer of linear polariser and quarter wave plate to ensure that any ambient light which enters the device is not reflected off the cathode back towards the viewer. However, this also absorbs 50% of the light generated by the OLED meaning higher driving voltages are required to achieve set brightness levels. This increases power consumption and decreases device operation lifetimes. Thus, mechanisms that decrease absorption by the anti-glare filter would increase the energy efficiency of an OLED display.

When approaching these factors to improve OLED devices, gaining some fine molecular control of the emitters is pivotal to future success, particularly when aiming to improve the IQE of a system. A current design strategy for TADF molecules is the D-A architecture, whereby, the emitter is built with the D intentionally localised on one part of the structure and the acceptor on another. To initiate TADF a near 90° angle between the D and A units is superior to activate the spin vibronic mechanism. However, enforcing complete rigidity upon a system will be counterproductive and yield phosphorescence. Too much flexibility however will cause a broadening of the emission, and increase non-radiative decay. Therefore, an ideal solution is an intermediate level of control. This work demonstrates that rotaxanes can provide this fine molecular control, displaying a balance between ridgity and flexibility to create efficient TADF emitters. Overall, this improvement in TADF means that the inherent 25% IQE due to spin statistics is broken and thus higher rates of IQE can be achieved.

The work has shown how theoretical methods can work harmoniously alongside physical analysis to provide a description of how the MIM improves the TADF output. In both the ground and excited states the mechanical bond decreases the energy gap between the two CT states and decreases the oscillator strength of the S_1 state. The control of both of these properties is advantageous when designing TADF emitters. Modelling the dynamics of the systems using *ab inito* MD gave good insight into the role of the macrocyclic ring. It was seen that the macrocyclic ring did no sit directly over the D-A bond, despite this the addition of the ring did increase the photoluminescence quantum yields. It would be an interesting future study to see the effect of the location of the macrocyclic ring on the quantum yield. Furthermore, this study showed the potential of this type of MIM for applications in TADF emitters, future work should investigate similar structures.

To have the ability to effectively model molecules and their properties provides a basis for not only developing new technology, but also gaining a better understanding as to existing systems. In the case of TADF, it is common to design emitters with a D-A architecture, this structure encourages CT character of the first excited state. Therefore, reducing the energy gap between the first excited singlet and triplet states, and thus improving the efficiency of TADF. However, it is known that standard hybrid exchange functionals do not provide a good description when there is a small exchange overlap. This work studied two tuned range-separated functionals, namely Koopmans OT and TT. In the case of both tuned range-separated functionals, they provided a better description of the states with CT character that did not have any other close lying states than the standard hybrid exchange functionals. However, they did show a geometry dependence, this was clear when the geometry allowed for mixing of close lying states. The TT approach showed the most geometry dependence.

The study continued to probe a selection of emitters that were designed to

have CP-TADF properties. They were of D-A architecture with a chiral perturbing unit added as an appendage. It was evident that the OT approach provided a better description than the standard exchange functional for the energies of the CT states, as expected, but an influence was also seen on the *g*-factors. Despite the emitters showing some chiroptical activity, this activity was very minimal. It is expected that this is due to the electric magnetic coupling remaining very small due to the small molecular size. The nature of the chiral perturbing unit is another reason why the *g*-factors remain small, this study has shown that very little of the S_1 state is spread over the chiral perturbing moiety. Therefore, this moiety has very little effect on the emission of the system.

Continuing the study of emitter with CP-TADF emission, a further emitter was investigated. This time the chiral perturbing was put closer to the active chromophore. Upon initial exploration, the emitter showed some promising features for both TADF emission and CP emission. However, upon comparison with experimental findings by The Fuchter Group, there was no CP emission observed. Furthermore, a more in depth study was undertaken in which the MD was scrutinised. This resulted in a large spread of chiroptical emission being observed, this is due to the fine-motion of the emitter throughout the emission process. This motion is critical for TADF emission but detrimental to CP emission, thus the design of this emitter was not a feasible solution to creating an efficient TADF emitter that also displayed CP emission. Therefore, the thesis moves to consider larger polymer systems that do not have an inherent limit to CP emission due to their size, which is a factor when designing small molecule CP-TADF emitters.

Finally, to improve device architecture, decrease power consumption and increase out-coupling, the integration of CP luminescence into emitters can not only reduce the need for polarisers, but also ensure that there is less light reflected back into the device itself therefore, reducing power consumption. Traditional TADF emitters designed with the D-A architecture can be manipulated to include a chiral section to induce both TADF and CP luminescence. However, this work concludes that the fine movement required for TADF quenches the CP luminescence of the emitter. Thus, a new strategy to design emitters that display both of these properties is brought forward. This work builds upon the work by Yang *et al.*[149] who present a chiral polymer synthesised by doping an achiral light-emitting polymer, namely F8BT, with a helically chiral aromatic molecule; the resultant polymer chain forms in a helical arrangement and showed to emit CP luminescence. This study aimed to understand the contributions of local short-range electric-magnetic coupling and longer-range structural chirality to aid the design of new materials with favourable CP emission.

In the short-range regime, the theoretical study found that CP light can be induced by the twisting of the polymer chain, and furthermore, that the direction of this twist will control the sign of the dissymmetry produced. This conclusion supported the experimental findings of Wan *et al.*[64] This study

also concluded that the excited state can be delocalised across the polymer structure and the length of the polymer, and importantly the length of the excited state, is most crucial to the size of the g_{lum}. To develop an understanding of the longer-range structural chirality, dimers were created. These dimers demonstrated that the exciton can be extended not only over the individual polymer chains, but also over nearby polymer chains. It was reported that the dissymmetry of these systems was significantly increased by exploiting the intrinsic magnetic transition dipole moment arising from the helically configured polymer backbones. However, it is important to note that this theory may not hold if polymers adopt a planar structure in the aggregate state as they are likely to have negligible magnetic transition dipole moments. Wan *et al.* have shown exceptional chiroptical response from thin films of PFO, which have a planar structure, in this case it is expected that the coupling of the electronic transition dipole moments dominate the interaction as the electronic-magnetic coupling is negligible.[157] Furthermore, this study does not yet consider the further exciton delocalisation over a larger stack, nor how conformational and environmental disorder impacts the chiroptical response of a larger stack. Polymer films that have been optimised for CP-OLEDs are only weakly ordered, therefore it is important to consider that the resultant dissymmetry will be the average across all orientations and configurations.[169] Moreover, it is possible that the overall chiroptical response would be reduced if all sites were equally likely to interact with CP light, as reducing the inter-chain coupling quenches the dissymmetry. However, both the energy and oscillator strengths of the states involved are controlled by this inter-chain coupling, meaning that not all sites are equally likely to absorb or emit light. Future work should apply molecular dynamics to investigate this effect.

Overall, this work has dived into how the design of molecules can influence their emission properties. In the first instance, this work probed how the macrocyclic ring could be utilised to manipulate the emission properties of mechanically interlocked molecules, namely rotaxanes. This work proved that architectural engineering of molecules can be used to fine tune emission properties. Furthermore, the thesis developed a description of the interplay between the TADF and CPL properties of single molecules. It is evident that making adjustments to traditional small TADF D-A molecules in an endeavour to induce dissymmetry is not conducive to creating effective TADF-CPL emitters. This is due to the inherent limit on the size of the chiroptical response from a small molecule. For this reason, the work moved to larger systems that could bypass this inherent limit. The work presented evidence that the exciton could be delocalised across neighbouring polymers and this extension is critical in enhancing the dissymmetry. Furthermore, this thesis has highlighted some key properties that could be implemented into a machine learning algorithm to predict molecules that could display these preferential properties.

Bibliography

[1] Lucas Frédéric, Alaric Desmarchelier, Ludovic Favereau, and Grégory Pieters. Designs and Applications of Circularly Polarized Thermally Activated Delayed Fluorescence Molecules. *Advanced Functional Materials*, page 2010281.

[2] Jamie Gibson, Andrew P Monkman, and Thomas J Penfold. The Importance of Vibronic Coupling for Efficient Reverse Intersystem Crossing in Thermally Activated Delayed Fluorescence Molecules. *Chemphyschem*, 17(19):2956–2961, October 2016.

[3] Fernando B Dias, Konstantinos N Bourdakos, Vygintas Jankus, Kathryn C Moss, Kiran T Kamtekar, Vandana Bhalla, José Santos, Martin R Bryce, and Andrew P Monkman. Triplet Harvesting with 100Activated Delayed Fluorescence in Charge Transfer OLED Emitters. *Advanced Materials*, 25(27):3707–3714, July 2013.

[4] Fernando B Dias, Thomas J Penfold, and Andrew P Monkman. Photophysics of thermally activated delayed fluorescence molecules. *Methods and applications in fluorescence*, 5(1):012001, 2017.

[5] T J Penfold, F B Dias, and A P Monkman. The theory of thermally activated delayed fluorescence for organic light emitting diodes. *Chemical Communications*, 54(32):3926–3935, April 2018.

[6] Pachaiyappan Rajamalli, Federica Rizzi, Wenbo Li, Michael A Jinks, Abhishek Kumar Gupta, Beth A Laidlaw, Ifor D W Samuel, Thomas J Penfold, Stephen M Goldup, and Eli Zysman-Colman. Using the Mechanical Bond to Tune the Performance of a Thermally Activated Delayed Fluorescence Emitter**. *Angewandte Chemie International Edition*, 60(21):12066–12073, May 2021.

[7] Julien Eng, Jerry Hagon, and Thomas James Penfold. D–A 3 TADF emitters: the role of the density of states for achieving faster triplet harvesting rates. *Journal of Materials Chemistry C*, 7(41):12942–12952, 2019.

[8] Julien Eng, Beth A Laidlaw, and Thomas J Penfold. On the geometry dependence of tuned-range separated hybrid functionals. *J Comput Chem*, page jcc.25868, May 2019.

[9] Beth Laidlaw, Julien Eng, Jessica Wade, Xingyuan Shi, Francesco Salerno, Matthew J Fuchter, and Thomas J Penfold. On the factors influencing the chiroptical response of conjugated polymer thin films. *Chemical Communications*, 2021.

[10] Rafael Gómez-Bombarelli, Jennifer N Wei, David Duvenaud, José Miguel Hernández-Lobato, Benjamín Sánchez-Lengeling, Dennis Sheberla, Jorge Aguilera-Iparraguirre, Timothy D Hirzel, Ryan P Adams, and Alán Aspuru-Guzik. Automatic chemical design using a data-driven continuous representation of molecules. *ACS central science*, 4(2):268–276, 2018.

[11] Yuge Huang, En-Lin Hsiang, Ming-Yang Deng, and Shin-Tson Wu. Mini-led, micro-led and oled displays: Present status and future perspectives. *Light: Science & Applications*, 9(1):1–16, 2020.

[12] Hiroki Uoyama, Kenichi Goushi, Katsuyuki Shizu, Hiroko Nomura, and Chihaya Adachi. Highly efficient organic light-emitting diodes from delayed fluorescence. *Nature*, 492(7428):234–238, December 2012.

[13] Qisheng Zhang, Bo Li, Shuping Huang, Hiroko Nomura, Hiroyuki Tanaka, and Chihaya Adachi. Efficient blue organic light-emitting diodes employing thermally activated delayed fluorescence. *Nature Photonics*, 8(4):326–332, April 2014.

[14] Shuzo Hirata, Yumi Sakai, Kensuke Masui, Hiroyuki Tanaka, Sae Youn Lee, Hiroko Nomura, Nozomi Nakamura, Mao Yasumatsu, Hajime Nakanotani, Qisheng Zhang, Katsuyuki Shizu, Hiroshi Miyazaki, and Chihaya Adachi. Highly efficient blue electroluminescence based on thermally activated delayed fluorescence. *Nature Materials*, 14(3):330–336, March 2015.

[15] Takuro Imagawa, Shuzo Hirata, Kenro Totani, Toshiyuki Watanabe, and Martin Vacha. Thermally activated delayed fluorescence with circularly polarized luminescence characteristics. *Chemical Communications*, 51(68):13268–13271, August 2015.

[16] Amin Salehi, Xiangyu Fu, Dong Hun Shin, and Franky So. Recent Advances in OLED Optical Design. *Advanced Functional Materials*, 29(15):1808803, April 2019.

[17] Steven R LaPlante, Lee D Fader, Keith R Fandrick, Daniel R Fandrick, Oliver Hucke, Ray Kemper, Stephen PF Miller, and Paul J Edwards. Assessing atropisomer axial chirality in drug discovery and development. *Journal of medicinal chemistry*, 54(20):7005–7022, 2011.

[18] Yuuya Nagata, Ryohei Takeda, and Michinori Suginome. Asymmetric Catalysis in Chiral Solvents: Chirality Transfer with Amplification of

Homochirality through a Helical Macromolecular Scaffold. *ACS Central Science*, July 2019.

[19] Oren Ben Dor, Shira Yochelis, Shinto P Mathew, Ron Naaman, and Yossi Paltiel. A chiral-based magnetic memory device without a permanent magnet. *Nature Communications*, 4(1):1–6, August 2013.

[20] Jochen R Brandt, Francesco Salerno, and Matthew J Fuchter. The added value of small-molecule chirality in technological applications. *Nat Rev Chem*, 1(6):1–12, June 2017.

[21] Carl Graebe. Die Lagerung der Atome im Raum. In *Geschichte der organischen Chemie*, pages 388–403. Springer, Berlin, Heidelberg, 1920.

[22] Cornelia Meinert, Søren V Hoffmann, Patrick Cassam-Chenaï, Amanda C Evans, Chaitanya Giri, Laurent Nahon, and Uwe J Meierhenrich. Photonenergy-controlled symmetry breaking with circularly polarized light. *Angewandte Chemie International Edition*, 53(1):210–214, January 2014.

[23] Robert D Richardson, Matthias G J Baud, Claire E Weston, Henry S Rzepa, Marina K Kuimova, and Matthew J Fuchter. Dual wavelength asymmetric photochemical synthesis with circularly polarized light. *Chemical Science*, 6(7):3853–3862, July 2015.

[24] Jake L Greenfield, Jessica Wade, Jochen R Brandt, Xingyuan Shi, Thomas J Penfold, and Matthew J Fuchter. Pathways to increase the dissymmetry in the interaction of chiral light and chiral molecules. *Chemical Science*, 12(25):8589–8602, July 2021.

[25] Esther M Sánchez Carnerero, Antonia R Agarrabeitia, Florencio Moreno, Beatriz L Maroto, Gilles Muller, Mar J Ortiz, and Santiago de la Moya. Circularly Polarized Luminescence from Simple Organic Molecules. *Chemistry – A European Journal*, 21:13488–13500, September 2015.

[26] Ching W Tang and Steven A VanSlyke. Organic electroluminescent diodes. *Applied physics letters*, 51(12):913–915, 1987.

[27] Katsuyuki Shizu, Jiyoung Lee, Hiroyuki Tanaka, Hiroko Nomura, Takuma Yasuda, Hironori Kaji, and Chihaya Adachi. Highly efficient electroluminescence from purely organic donor–acceptor systems. *Pure and Applied Chemistry*, 87(7):627–638, July 2015.

[28] Gleb Baryshnikov, Boris Minaev, and Hans Ågren. Theory and calculation of the phosphorescence phenomenon. *Chemical reviews*, 117(9):6500–6537, 2017.

[29] Laura Talens Peiró, Gara Villalba Méndez, and Robert U Ayres. Material flow analysis of scarce metals: Sources, functions, end-uses and aspects for future supply. *Environmental science & technology*, 47(6):2939–2947, 2013.

[30] D Volz, M Wallesch, C Fléchon, M Danz, A Verma, JM Navarro, DM Zink, S Bräse, and T Baumann. From iridium and platinum to copper and carbon: new avenues for more sustainability in organic light-emitting diodes. *Green Chemistry*, 17(4):1988–2011, 2015.

[31] CA Parker. Sensitized p-type delayed fluorescence. *Proceedings of the Royal Society of London. Series A. Mathematical and Physical Sciences*, 276(1364):125–135, 1963.

[32] D Y Kondakov, T D Pawlik, T K Hatwar, and J P Spindler. Triplet annihilation exceeding spin statistical limit in highly efficient fluorescent organic light-emitting diodes. *Journal of Applied Physics*, 106(12):124510, December 2009.

[33] Chihaya Adachi. Third-generation organic electroluminescence materials. *Japanese Journal of Applied Physics*, 53(6):060101, May 2014.

[34] CA Parker and CG Hatchard. Triplet-singlet emission in fluid solutions. phosphorescence of eosin. *Transactions of the Faraday Society*, 57:1894–1904, 1961.

[35] Yirang Im, Mounggon Kim, Yong Joo Cho, Jeong-A Seo, Kyoung Soo Yook, and Jun Yeob Lee. Molecular Design Strategy of Organic Thermally Activated Delayed Fluorescence Emitters. *Chemistry Of Materials*, 29(5):1946–1963, February 2017.

[36] Mario N Berberan-Santos and Joao MM Garcia. *Unusually strong delayed fluorescence of C70*, volume 118. ACS Publications, 1996.

[37] Ayataka Endo, Mai Ogasawara, Atsushi Takahashi, Daisuke Yokoyama, Yoshimine Kato, and Chihaya Adachi. Thermally Activated Delayed Fluorescence from Sn4+-Porphyrin Complexes and Their Application to Organic Light Emitting Diodes - A Novel Mechanism for Electroluminescence. *Advanced Materials*, 21(47):4802–4806, August 2009.

[38] Joseph C Deaton, Steven C Switalski, Denis Y Kondakov, Ralph H Young, Thomas D Pawlik, David J Giesen, Seth B Harkins, Alex JM Miller, Seth F Mickenberg, and Jonas C Peters. E-type delayed fluorescence of a phosphine-supported cu2 (μ-nar2) 2 diamond core: harvesting singlet and triplet excitons in oleds. *Journal of the American Chemical Society*, 132(27):9499–9508, 2010.

[39] Ayataka Endo, Keigo Sato, Kazuaki Yoshimura, Takahiro Kai, Atsushi Kawada, Hiroshi Miyazaki, and Chihaya Adachi. Efficient upconversion of triplet excitons into a singlet state and its application for organic light emitting diodes. *Applied Physics Letters*, 98(8):083302, February 2011.

[40] Jon R Kirchhoff, Roland E Gamache, Marcus W Blaskie, Alan A Del Paggio, Russell K Lengel, and David R McMillin. Temperature dependence of luminescence from Cu(NN)2+ systems in fluid solution. Evidence for the participation of two excited states. *Inorganic Chemistry*, 22(17):2380–2384, August 1983.

[41] Kenichi Goushi, Kou Yoshida, Keigo Sato, and Chihaya Adachi. Organic light-emitting diodes employing efficient reverse intersystem crossing for triplet-to-singlet state conversion. *Nature Photonics*, 6(4):253–258, March 2012.

[42] Qisheng Zhang, Jie Li, Katsuyuki Shizu, Shuping Huang, Shuzo Hirata, Hiroshi Miyazaki, and Chihaya Adachi. Design of Efficient Thermally Activated Delayed Fluorescence Materials for Pure Blue Organic Light Emitting Diodes. *Journal Of The American Chemical Society*, 134(36):14706–14709, September 2012.

[43] Fernando B Dias. Kinetics of thermal-assisted delayed fluorescence in blue organic emitters with large singlet–triplet energy gap. *Philosophical Transactions of the Royal Society A: Mathematical, Physical and Engineering Sciences*, 373(2044):20140447, 2015.

[44] Christel M Marian. Spin-orbit coupling and intersystem crossing in molecules. *Wiley Interdisciplinary Reviews: Computational Molecular Science*, 2(2):187–203, July 2011.

[45] Paloma L Santos, Jonathan S Ward, Przemyslaw Data, Andrei S Batsanov, Martin R Bryce, Fernando B Dias, and Andrew P Monkman. Engineering the singlet–triplet energy splitting in a TADF molecule. *Journal of Materials Chemistry C*, 4(17):3815–3824, 2016.

[46] Jonathan S Ward, Roberto S Nobuyasu, Andrei S Batsanov, Przemyslaw Data, Andrew P Monkman, Fernando B Dias, and Martin R Bryce. The interplay of thermally activated delayed fluorescence (TADF) and room temperature organic phosphorescence in sterically-constrained donor–acceptor charge-transfer molecules. *Chemical Communications*, 52(12):2612–2615, February 2016.

[47] Christel M Marian. Mechanism of the Triplet-to-Singlet Upconversion in the Assistant Dopant ACRXTN. *The Journal of Physical Chemistry C*, 120(7):3715–3721, February 2016.

[48] Marc K Etherington, Flavio Franchello, Jamie Gibson, Thomas Northey, José Santos, Jonathan S Ward, Heather F Higginbotham, Przemyslaw Data, Aleksandra Kurowska, Paloma Lays Dos Santos, David R Graves, Andrei S Batsanov, Fernando B Dias, Martin R Bryce, Thomas J Penfold, and Andrew P Monkman. Regio- and conformational isomerization critical to design of efficient thermally-activated delayed fluorescence emitters. *Nature Communications*, 8:14987, April 2017.

[49] Emiel Peeters, Marwijn PT Christiaans, René AJ Janssen, Herman FM Schoo, Harry PJM Dekkers, and EW Meijer. Circularly polarized electroluminescence from a polymer light-emitting diode. *Journal of the American Chemical Society*, 119(41):9909–9910, 1997.

[50] Claudia Wagenknecht, Che-Ming Li, Andreas Reingruber, Xiao-Hui Bao, Alexander Goebel, Yu-Ao Chen, Qiang Zhang, Kai Chen, and Jian-Wei Pan. Experimental demonstration of a heralded entanglement source. *Nature Photonics*, 4(8):549–552, August 2010.

[51] Dal-Young Kim. Potential application of spintronic light-emitting diode to binocular vision for three-dimensional display technology. *Journal of the Korean Physical Society*, 49:505, 2006.

[52] Marie C Heffern, Lauren M Matosziuk, and Thomas J Meade. Lanthanide Probes for Bioresponsive Imaging. *Chemical Reviews*, 114, April 2014.

[53] JT Collins, KR Rusimova, DC Hooper, H-H Jeong, L Ohnoutek, F Pradaux-Caggiano, T Verbiest, DR Carbery, P Fischer, and VK Valev. First observation of optical activity in hyper-rayleigh scattering. *Physical Review X*, 9(1):011024, 2019.

[54] Won Jin Choi, Gong Cheng, Zhengyu Huang, Shuai Zhang, Theodore B Norris, and Nicholas A Kotov. Terahertz circular dichroism spectroscopy of biomaterials enabled by kirigami polarization modulators. *Nature materials*, 18(8):820–826, 2019.

[55] Leonardo De Boni, Carlos Toro, and Florencio E Hernández. Synchronized double l-scan technique for the simultaneous measurement of polarization-dependent two-photon absorption in chiral molecules. *Optics letters*, 33(24):2958–2960, 2008.

[56] Lukas Ohnoutek, Nam Heon Cho, Alexander William Allen Murphy, Hyeohn Kim, Dora Maria Răsădean, Gheorghe Dan Pantoş, Ki Tae Nam, and Ventsislav Kolev Valev. Single nanoparticle chiroptics in a liquid: optical activity in hyper-rayleigh scattering from au helicoids. *Nano letters*, 20(8):5792–5798, 2020.

[57] Jochen R Brandt, Xuhua Wang, Ying Yang, Alasdair J Campbell, and Matthew J Fuchter. Circularly Polarized Phosphorescent Electroluminescence with a High Dissymmetry Factor from PHOLEDs Based on a Platinahelicene. *Journal Of The American Chemical Society*, 138(31):9743–9746, August 2016.

[58] Yoshito Nakai, Tadashi Mori, and Yoshihisa Inoue. Theoretical and experimental studies on circular dichroism of carbo [n] helicenes. *The Journal of Physical Chemistry A*, 116(27):7372–7385, 2012.

[59] Jianmei Han, Song Guo, Hu Lu, Shujuan Liu, Qiang Zhao, and Wei Huang. Recent Progress on Circularly Polarized Luminescent Materials for Organic Optoelectronic Devices. *Advanced Optical Materials*, 6(17):1800538, September 2018.

[60] Francesco Zinna, Umberto Giovanella, and Lorenzo Di Bari. Highly Circularly Polarized Electroluminescence from a Chiral Europium Complex. *Advanced Materials*, 27(10):1791–1795, March 2015.

[61] Francesco Zinna, Mariacecilia Pasini, Francesco Galeotti, Chiara Botta, Lorenzo Di Bari, and Umberto Giovanella. Design of Lanthanide-Based OLEDs with Remarkable Circularly Polarized Electroluminescence. *Advanced Functional Materials*, 27(1):1603719, January 2017.

[62] Tian-Yi Li, Yi-Ming Jing, Xuan Liu, Yue Zhao, Lin Shi, Zhiyong Tang, You-Xuan Zheng, and Jing-Lin Zuo. Circularly polarised phosphorescent photoluminescence and electroluminescence of iridium complexes. *Scientific Reports*, 5:14912, October 2015.

[63] Daniele Di Nuzzo, Chidambar Kulkarni, Baodan Zhao, Eilam Smolinsky, Francesco Tassinari, Stefan CJ Meskers, Ron Naaman, EW Meijer, and Richard H Friend. High circular polarization of electroluminescence achieved via self-assembly of a light-emitting chiral conjugated polymer into multidomain cholesteric films. *Acs Nano*, 11(12):12713–12722, 2017.

[64] Li Wan, Jessica Wade, Francesco Salerno, Oriol Arteaga, Beth Laidlaw, Xuhua Wang, Thomas Penfold, Matthew J Fuchter, and Alasdair J Campbell. Inverting the handedness of circularly polarized luminescence from light-emitting polymers using film thickness. *ACS nano*, 13(7):8099–8105, 2019.

[65] Kyriaki Manoli, Maria Magliulo, and Luisa Torsi. Chiral sensor devices for differentiation of enantiomers. *Differentiation of Enantiomers II*, pages 133–176, 2013.

[66] L Rosenfeld. Quantenmechanische Theorie der natürlichen optischen Aktivität von Flüssigkeiten und Gasen. *Z. Physik*, 52(3):161–174, March 1929.

[67] Hiroki Tanaka, Yoshihisa Inoue, and Tadashi Mori. Circularly polarized luminescence and circular dichroisms in small organic molecules: correlation between excitation and emission dissymmetry factors. *ChemPhotoChem*, 2(5):386–402, 2018.

[68] Stephan Bernadotte, Andrew J Atkins, and Christoph R Jacob. Origin-independent calculation of quadrupole intensities in X-ray spectroscopy. *The Journal of Chemical Physics*, 137(20):204106, November 2012.

[69] Nanna Holmgaard List, Joanna Kauczor, Trond Saue, Hans Jørgen Aagaard Jensen, and Patrick Norman. Beyond the electric-dipole approximation: A formulation and implementation of molecular response theory for the description of absorption of electromagnetic field radiation. *The Journal of Chemical Physics*, 142(24):244111, June 2015.

[70] Nobuyuki Harada and Koji Nakanishi. Exciton chirality method and its application to configurational and conformational studies of natural products. *Accounts of Chemical Research*, 5(8):257–263, 1972.

[71] M Born and W Heisenberg. Zur quantentheorie der molekeln. In *Original Scientific Papers Wissenschaftliche Originalarbeiten*, pages 216–246. Springer, 1985.

[72] Aurora Pribram-Jones, David A Gross, and Kieron Burke. Dft: A theory full of holes? *Annual review of physical chemistry*, 66:283–304, 2015.

[73] Pierre Hohenberg and Walter Kohn. Inhomogeneous electron gas. *Physical review*, 136(3B):B864, 1964.

[74] Walter Kohn and Lu Jeu Sham. Self-consistent equations including exchange and correlation effects. *Physical review*, 140(4A):A1133, 1965.

[75] John P Perdew and Karla Schmidt. Jacob's ladder of density functional approximations for the exchange-correlation energy. *AIP Conference Proceedings*, 577(1):1–20, August 2001.

[76] Michael G Medvedev, Ivan S Bushmarinov, Jianwei Sun, John P Perdew, and Konstantin A Lyssenko. Density functional theory is straying from the path toward the exact functional. *Science*, 355(6320):49–52, January 2017.

[77] Eunji Sim, Suhwan Song, and Kieron Burke. Quantifying Density Errors in DFT. *The Journal of Physical Chemistry Letters*, October 2018.

[78] John P Perdew, Kieron Burke, and Matthias Ernzerhof. Generalized gradient approximation made simple. *Physical review letters*, 77(18):3865, 1996.

[79] A D Becke. Density-functional exchange-energy approximation with correct asymptotic behavior. *Phys. Rev. A*, 38(6):3098–3100, September 1988.

[80] Chengteh Lee, Weitao Yang, and Robert G Parr. Development of the Colle-Salvetti correlation-energy formula into a functional of the electron density. *Phys. Rev. B*, 37(2):785–789, January 1988.

[81] Andreas Dreuw, Jennifer L Weisman, and Martin Head-Gordon. Long-range charge-transfer excited states in time-dependent density functional theory require non-local exchange. *The Journal of chemical physics*, 119(6):2943–2946, 2003.

[82] B Miehlich, A Savin, H Stoll, H Preuss Chemical Physics Letters, and 1989. Results obtained with the correlation energy density functionals of Becke and Lee, Yang and Parr. *lct.jussieu.fr*.

[83] Axel D Becke. Density-functional thermochemistry. I. The effect of the exchange-only gradient correction. *The Journal of Chemical Physics*, 96(3):2155–2160, August 1998.

[84] John P Perdew, Matthias Ernzerhof, and Kieron Burke. Rationale for mixing exact exchange with density functional approximations. *The Journal of Chemical Physics*, 105(22):9982–9985, June 1998.

[85] Tamar Stein, Leeor Kronik, and Roi Baer. Reliable prediction of charge transfer excitations in molecular complexes using time-dependent density functional theory. *Journal of the American Chemical Society*, 131(8):2818–2820, 2009.

[86] Zhou Lin and Troy Van Voorhis. Triplet tuning: a novel family of non-empirical exchange-correlation functionals. *Journal of chemical theory and computation*, 15(2):1226–1241, 2019.

[87] W J Hehre, R F Stewart, and J A Pople. Self-Consistent Molecular-Orbital Methods. I. Use of Gaussian Expansions of Slater-Type Atomic Orbitals. *The Journal of Chemical Physics*, 51(6):2657, September 2003.

[88] Erich Runge and E K U Gross. Density-Functional Theory for Time-Dependent Systems. *Physical Review Letters*, 52(12):997–1000, March 1984.

[89] Samat Tussupbayev, Niranjan Govind, Kenneth Lopata, and Christopher J Cramer. Comparison of real-time and linear-response time-dependent density functional theories for molecular chromophores ranging from sparse to high densities of states. *Journal of chemical theory and computation*, 11(3):1102–1109, 2015.

[90] Mark E Casida. Time-dependent density functional response theory for molecules. In *Recent Advances In Density Functional Methods: (Part I)*, pages 155–192. World Scientific, 1995.

[91] So Hirata and Martin Head-Gordon. Time-dependent density functional theory within the Tamm–Dancoff approximation. *Chemical Physics Letters*, 314(3-4):291–299, December 1999.

[92] Benedetta Mennucci. Polarizable continuum model. *Wiley Interdisciplinary Reviews: Computational Molecular Science*, 2(3):386–404, 2012.

[93] Jacopo Tomasi, Benedetta Mennucci, and Roberto Cammi. Quantum mechanical continuum solvation models. *Chemical reviews*, 105(8):2999–3094, 2005.

[94] Marc K Etherington, Jamie Gibson, Heather F Higginbotham, Thomas J Penfold, and Andrew P Monkman. Revealing the spin-vibronic coupling mechanism of thermally activated delayed fluorescence. *Nature Communications*, 7(1):13680–7, November 2016.

[95] Bluebell H Drummond, Naoya Aizawa, Yadong Zhang, William K Myers, Yao Xiong, Matthew W Cooper, Stephen Barlow, Qinying Gu, Leah R Weiss, Alexander J Gillett, Dan Credgington, Yong-Jin Pu, Seth R Marder, and Emrys W Evans. Electron spin resonance resolves intermediate triplet states in delayed fluorescence. *Nature Communications*, 12(1):4532–11, July 2021.

[96] Thomas J Penfold, Etienne Gindensperger, Chantal Daniel, and Christel M Marian. Spin-vibronic mechanism for intersystem crossing. *Chemical reviews*, 118(15):6975–7025, 2018.

[97] Bo Li, Hiroko Nomura, Hiroshi Miyazaki, Qisheng Zhang, Kou Yoshida, Yoshinori Suzuma, Akihiro Orita, Junzo Otera, and Chihaya Adachi. Dicarbazolyldicyanobenzenes as Thermally Activated Delayed Fluorescence Emitters: Effect of Substitution Position on Photoluminescent and Electroluminescent Properties. *Chemistry Letters*, 43(3):319–321, November 2013.

[98] In Seob Park, Sae Youn Lee, Chihaya Adachi, and Takuma Yasuda. Full-Color Delayed Fluorescence Materials Based on Wedge-Shaped Phthalonitriles and Dicyanopyrazines: Systematic Design, Tunable Photophysical Properties, and OLED Performance. *Advanced Functional Materials*, 26(11):1813–1821, February 2016.

[99] Pachaiyappan Rajamalli, Dongyang Chen, Wenbo Li, Ifor D W Samuel, David B Cordes, Alexandra M Z Slawin, and Eli Zysman-Colman. Enhanced thermally activated delayed fluorescence through bridge modification in sulfone-based emitters employed in deep blue organic light-emitting diodes. *Journal of Materials Chemistry C*, 7(22):6664–6671, June 2019.

[100] Paloma Lays Dos Santos, Dongyang Chen, Pachaiyappan Rajamalli, Tomas Matulaitis, David B Cordes, Alexandra M Z Slawin, Denis Jacquemin, Eli Zysman-Colman, and Ifor D W Samuel. Use of Pyrimidine and Pyrazine Bridges as a Design Strategy To Improve the Performance of Thermally Activated Delayed Fluorescence Organic Light Emitting Diodes. *ACS Applied Materials & Interfaces*, 11(48):45171–45179, November 2019.

[101] Yuewei Zhang, Yang Miao, Xiaoxian Song, Yu Gao, Zuolun Zhang, Kaiqi Ye, and Yue Wang. Single-Molecule-based White-Light Emissive Organic Solids with Molecular-Packing-Dependent Thermally Activated Delayed Fluorescence. *The Journal of Physical Chemistry Letters*, 8(19):4808–4813, October 2017.

[102] Xian-Kai Chen, Brandon W Bakr, Morgan Auffray, Youichi Tsuchiya, C David Sherrill, Chihaya Adachi, and Jean-Luc Brédas. Intramolecular Noncovalent Interactions Facilitate Thermally Activated Delayed Fluorescence (TADF). *The Journal of Physical Chemistry Letters*, 10(12):3260–3268, May 2019.

[103] Wenbo Yuan, Hannan Yang, Chunbo Duan, Xudong Cao, Jing Zhang, Hui Xu, Ning Sun, Youtian Tao, and Wei Huang. Molecular configuration fixation with c–h··· f hydrogen bonding for thermally activated delayed fluorescence acceleration. *Chem*, 6(8):1998–2008, 2020.

[104] Xiang Ma and He Tian. Bright functional rotaxanes. *Chemical Society Reviews*, 39(1):70–80, 2010.

[105] Jason Y C Lim, Igor Marques, Vítor Félix, and Paul D Beer. Enantioselective Anion Recognition by Chiral Halogen-Bonding [2]Rotaxanes. *Journal Of The American Chemical Society*, 139(35):12228–12239, September 2017.

[106] Mathieu Denis, Jessica Pancholi, Kajally Jobe, Michael Watkinson, and Stephen M Goldup. Chelating Rotaxane Ligands as Fluorescent Sensors for Metal Ions. *Angewandte Chemie International Edition*, 57(19):5310–5314, May 2018.

[107] Yuya Tachibana, Nobuhiro Kihara, and Toshikazu Takata. Asymmetric benzoin condensation catalyzed by chiral rotaxanes tethering a thiazolium salt moiety via the cooperation of the component: can rotaxane

be an effective reaction field? *Journal of the American Chemical Society*, 126(11):3438–3439, 2004.

[108] Jack Beswick, Victor Blanco, Guillaume De Bo, David A Leigh, Urszula Lewandowska, Bartosz Lewandowski, and Kenji Mishiro. Selecting reactions and reactants using a switchable rotaxane organocatalyst with two different active sites. *Chemical Science*, 6(1):140–143, 2015.

[109] Marzia Galli, James E M Lewis, and Stephen M Goldup. A Stimuli-Responsive Rotaxane-Gold Catalyst: Regulation of Activity and Diastereoselectivity. *Angewandte Chemie International Edition*, 54(46):13545–13549, November 2015.

[110] Rajamalli Pachai Gounder, Diego Rota Martir, and Eli Zysman-Colman. Pyridine-functionalized carbazole donor and benzophenone acceptor design for thermally activated delayed fluorescence emitters in blue organic light-emitting diodes. *Journal of Photonics for Energy*, 8(3):032106, 2018.

[111] Diego Rota Martir, Antonella Pizzolante, Daniel Escudero, Denis Jacquemin, Stuart L Warriner, and Eli Zysman-Colman. Photoinduced Energy and Electron Transfer Between a Photoactive Cage Based on a Thermally Activate Delayed Fluorescence Ligand and Encapsulated Fluorescent Dyes. *ACS Applied Energy Materials*, May 2018.

[112] P Rajamalli, Diego Rota Martir, and Eli Zysman-Colman. Molecular design strategy for a two-component gel based on a thermally activated delayed fluorescence emitter. *ACS Applied Energy Materials*, 1(2):649–654, 2018.

[113] Yihan Shao, Zhengting Gan, Evgeny Epifanovsky, Andrew T B Gilbert, Michael Wormit, Joerg Kussmann, Adrian W Lange, Andrew Behn, Jia Deng, Xintian Feng, Debashree Ghosh, Matthew Goldey, Paul R Horn, Leif D Jacobson, Ilya Kaliman, Rustam Z Khaliullin, Tomasz Kuś, Arie Landau, Jie Liu, Emil I Proynov, Young Min Rhee, Ryan M Richard, Mary A Rohrdanz, Ryan P Steele, Eric J Sundstrom, H Lee Woodcock III, Paul M Zimmerman, Dmitry Zuev, Ben Albrecht, Ethan Alguire, Brian Austin, Gregory J O Beran, Yves A Bernard, Eric Berquist, Kai Brandhorst, Ksenia B Bravaya, Shawn T Brown, David Casanova, Chun-Min Chang, Yunqing Chen, Siu Hung Chien, Kristina D Closser, Deborah L Crittenden, Michael Diedenhofen, Robert A DiStasio Jr, Hainam Do, Anthony D Dutoi, Richard G Edgar, Shervin Fatehi, Laszlo Fusti-Molnar, An Ghysels, Anna Golubeva-Zadorozhnaya, Joseph Gomes, Magnus W D Hanson-Heine, Philipp H P Harbach, Andreas W Hauser, Edward G Hohenstein, Zachary C Holden, Thomas-C Jagau, Hyunjun Ji, Benjamin Kaduk, Kirill Khistyaev, Jaehoon Kim, Jihan Kim, Rollin A King, Phil Klunzinger, Dmytro Kosenkov, Tim Kowalczyk, Caroline M Krauter, Ka Un Lao, Adèle D Laurent, Keith V Lawler,

Sergey V Levchenko, Ching Yeh Lin, Fenglai Liu, Ester Livshits, Rohini C Lochan, Arne Luenser, Prashant Manohar, Samuel F Manzer, Shan-Ping Mao, Narbe Mardirossian, Aleksandr V Marenich, Simon A Maurer, Nicholas J Mayhall, Eric Neuscamman, C Melania Oana, Roberto Olivares-Amaya, Darragh P O'Neill, John A Parkhill, Trilisa M Perrine, Roberto Peverati, Alexander Prociuk, Dirk R Rehn, Edina Rosta, Nicholas J Russ, Shaama M Sharada, Sandeep Sharma, David W Small, Alexander Sodt, Tamar Stein, David Stück, Yu-Chuan Su, Alex J W Thom, Takashi Tsuchimochi, Vitalii Vanovschi, Leslie Vogt, Oleg Vydrov, Tao Wang, Mark A Watson, Jan Wenzel, Alec White, Christopher F Williams, Jun Yang, Sina Yeganeh, Shane R Yost, Zhi-Qiang You, Igor Ying Zhang, Xing Zhang, Yan Zhao, Bernard R Brooks, Garnet K L Chan, Daniel M Chipman, Christopher J Cramer, William A Goddard III, Mark S Gordon, Warren J Hehre, Andreas Klamt, Henry F Schaefer III, Michael W Schmidt, C David Sherrill, Donald G Truhlar, Arieh Warshel, Xin Xu, Alán Aspuru-Guzik, Roi Baer, Alexis T Bell, Nicholas A Besley, Jeng-Da Chai, Andreas Dreuw, Barry D Dunietz, Thomas R Furlani, Steven R Gwaltney, Chao-Ping Hsu, Yousung Jung, Jing Kong, Daniel S Lambrecht, WanZhen Liang, Christian Ochsenfeld, Vitaly A Rassolov, Lyudmila V Slipchenko, Joseph E Subotnik, Troy Van Voorhis, John M Herbert, Anna I Krylov, Peter M W Gill, and Martin Head-Gordon. Advances in molecular quantum chemistry contained in the Q-Chem 4 program package. *Molecular Physics*, December 2014.

[114] Carlo Adamo and Vincenzo Barone. Toward reliable density functional methods without adjustable parameters: The PBE0 model. *The Journal of Chemical Physics*, 110(13):6158, March 1999.

[115] Florian Weigend and Reinhart Ahlrichs. Balanced basis sets of split valence, triple zeta valence and quadruple zeta valence quality for h to rn: Design and assessment of accuracy. *Physical Chemistry Chemical Physics*, 7(18):3297–3305, 2005.

[116] Ivan S Ufimtsev and Todd J Martinez. Quantum chemistry on graphical processing units. 1. strategies for two-electron integral evaluation. *Journal of Chemical Theory and Computation*, 4(2):222–231, 2008.

[117] Ivan S Ufimtsev and Todd J Martinez. Quantum chemistry on graphical processing units. 2. direct self-consistent-field implementation. *Journal of Chemical Theory and Computation*, 5(4):1004–1015, 2009.

[118] Ivan S Ufimtsev and Todd J Martinez. Quantum chemistry on graphical processing units. 3. analytical energy gradients, geometry optimization, and first principles molecular dynamics. *Journal of Chemical Theory and Computation*, 5(10):2619–2628, 2009.

[119] M J Merriam, R Rodriguez, and Jeanne L McHale. Charge-transfer transitions of 2:1 electron donor-acceptor complexes. *ACS Publications*, 91(5):1058–1063, May 2002.

[120] Anton Pershin, David Hall, Vincent Lemaur, Juan-Carlos Sancho-Garcia, Luca Muccioli, Eli Zysman-Colman, David Beljonne, and Yoann Olivier. Highly emissive excitons with reduced exchange energy in thermally activated delayed fluorescent molecules. *Nature communications*, 10(1):1–5, 2019.

[121] Jan-Michael Mewes. Modeling tadf in organic emitters requires a careful consideration of the environment and going beyond the franck–condon approximation. *Physical Chemistry Chemical Physics*, 20(18):12454–12469, 2018.

[122] Igor Lyskov and Christel M Marian. Climbing up the ladder: intermediate triplet states promote the reverse intersystem crossing in the efficient tadf emitter acrsa. *The Journal of Physical Chemistry C*, 121(39):21145–21153, 2017.

[123] Angela Rodriguez-Serrano, Fabian Dinkelbach, and Christel M Marian. Intersystem crossing processes in the 2czpn emitter: a dft/mrci study including vibrational spin–orbit interactions. *Physical Chemistry Chemical Physics*, 23(5):3668–3678, 2021.

[124] Carsten A Ullrich. *Time-dependent density-functional theory: concepts and applications*. OUP Oxford, 2011.

[125] Shuping Huang, Qisheng Zhang, Yoshihito Shiota, Tetsuya Nakagawa, Kazuhiro Kuwabara, Kazunari Yoshizawa, and Chihaya Adachi. Computational prediction for singlet-and triplet-transition energies of charge-transfer compounds. *Journal of chemical theory and computation*, 9(9):3872–3877, 2013.

[126] Andreas Dreuw and Martin Head-Gordon. Single-reference ab initio methods for the calculation of excited states of large molecules. *Chemical reviews*, 105(11):4009–4037, 2005.

[127] Yan Zhao and Donald G Truhlar. The m06 suite of density functionals for main group thermochemistry, thermochemical kinetics, noncovalent interactions, excited states, and transition elements: two new functionals and systematic testing of four m06-class functionals and 12 other functionals. *Theoretical chemistry accounts*, 120(1):215–241, 2008.

[128] Takeshi Yanai, David P Tew, and Nicholas C Handy. A new hybrid exchange–correlation functional using the coulomb-attenuating method (cam-b3lyp). *Chemical physics letters*, 393(1-3):51–57, 2004.

[129] Zhou Lin Van Voorhis and Troy. Triplet Tuning: A Novel Family of Non-Empirical Exchange Correlation Functionals. pages 1–16, February 2019.

[130] Paloma L dos Santos, Jonathan S Ward, Daniel G Congrave, Andrei S Batsanov, Julien Eng, Jessica E Stacey, Thomas J Penfold, Andrew P Monkman, and Martin R Bryce. Triazatruxene: A Rigid Central Donor Unit for a D–A3 Thermally Activated Delayed Fluorescence Material Exhibiting Sub-Microsecond Reverse Intersystem Crossing and Unity Quantum Yield via Multiple Singlet–Triplet State Pairs. *Advanced Science*, 5(6):1700989, June 2018.

[131] Thomas J Penfold. On Predicting the Excited-State Properties of Thermally Activated Delayed Fluorescence Emitters. *The Journal of Physical Chemistry C*, 119(24):13535–13544, June 2015.

[132] Sophie Feuillastre, Mathilde Pauton, Longhui Gao, Alaric Desmarchelier, Adrian J Riives, Damien Prim, Denis Tondelier, Bernard Geffroy, Gilles Muller, Gilles Clavier, and Grégory Pieters. Design and Synthesis of New Circularly Polarized Thermally Activated Delayed Fluorescence Emitters. *Journal Of The American Chemical Society*, 138(12):3990–3993, March 2016.

[133] Andreas Dreuw and Martin Head-Gordon. *Single-Reference ab Initio Methods for the Calculation of Excited States of Large Molecules*, volume 105. American Chemical Society, October 2005.

[134] Axel D Becke. Density-functional thermochemistry. III. The role of exact exchange. *The Journal of Chemical Physics*, 98(7):5648, August 1998.

[135] Philip J Stephens, Frank J Devlin, Cary F Chabalowski, and Michael J Frisch. Ab initio calculation of vibrational absorption and circular dichroism spectra using density functional force fields. *The Journal of physical chemistry*, 98(45):11623–11627, 1994.

[136] T Koopmans. Über die Zuordnung von Wellenfunktionen und Eigenwerten zu den Einzelnen Elektronen Eines Atoms. *Physica*, 1(1-6):104–113, January 1934.

[137] Zhou Lin Van Voorhis and Troy. Triplet Tuning: A Novel Family of Non-Empirical Exchange Correlation Functionals. pages 1–16, February 2019.

[138] Andreas Görling. Symmetry in density-functional theory. *Physical Review A*, 47(4):2783, 1993.

[139] Zhou Lin and Troy Van Voorhis. Triplet Tuning: A Novel Family of Non-Empirical Exchange-Correlation Functionals. *Journal Of Chemical Theory And Computation*, 15(2):1226–1241, February 2019.

[140] Mary A Rohrdanz, Katie M Martins, and John M Herbert. A long-range-corrected density functional that performs well for both ground-state properties and time-dependent density functional theory excitation energies, including charge-transfer excited states. *The Journal of Chemical Physics*, 130(5):054112, February 2009.

[141] R Ditchfield, W J Hehre, and J A Pople. Self-Consistent Molecular-Orbital Methods. IX. An Extended Gaussian-Type Basis for Molecular-Orbital Studies of Organic Molecules. *The Journal of Chemical Physics*, 54(2):724, September 2003.

[142] P C Hariharan and J A Pople. Accuracy of AH n equilibrium geometries by single determinant molecular orbital theory. *Molecular Physics*, 27(1):209–214, August 2006.

[143] Frank Neese. Software update: the ORCA program system, version 4.0. *Wiley Interdisciplinary Reviews: Computational Molecular Science*, 8(1):73–78, 2017.

[144] Jamie Gibson, Andrew P Monkman, and Thomas J Penfold. The Importance of Vibronic Coupling for Efficient Reverse Intersystem Crossing in Thermally Activated Delayed Fluorescence Molecules. *Chemphyschem*, 17(19):2956–2961, July 2016.

[145] Roberto S Nobuyasu, Zhongjie Ren, Gareth C Griffiths, Andrei S Batsanov, Przemyslaw Data, Shouke Yan, Andrew P Monkman, Martin R Bryce, and Fernando B Dias. Rational design of tadf polymers using a donor–acceptor monomer with enhanced tadf efficiency induced by the energy alignment of charge transfer and local triplet excited states. *Advanced Optical Materials*, 4(4):597–607, 2016.

[146] Lucas Frédéric, Alaric Desmarchelier, Romain Plais, Leonid Lavnevich, Gilles Muller, Cassie Villafuerte, Gilles Clavier, Etienne Quesnel, Benoit Racine, Sylvia Meunier-Della-Gatta, et al. Maximizing chiral perturbation on thermally activated delayed fluorescence emitters and elaboration of the first top-emission circularly polarized oled. *Advanced Functional Materials*, 30(43):2004838, 2020.

[147] Kikuya Hayashi, Arimasa Matsumoto, and Shuzo Hirata. Chiral approach to investigate mechanism of highly efficient thermally activated delayed fluorescence. *Chemical Communications*, 57(14):1738–1741, 2021.

[148] Roi Baer and Daniel Neuhauser. Density functional theory with correct long-range asymptotic behavior. *Physical Review Letters*, 94(4):043002, February 2005.

[149] Ying Yang, Rosenildo Correa da Costa, Detlef-M Smilgies, Alasdair J Campbell, and Matthew J Fuchter. Induction of circularly polarized electroluminescence from an achiral light-emitting polymer via a chiral small-molecule dopant. *Advanced Materials*, 25(18):2624–2628, 2013.

[150] Da-Wei Zhang, Meng Li, and Chuan-Feng Chen. Recent advances in circularly polarized electroluminescence based on organic light-emitting diodes. *Chemical Society Reviews*, 49(5):1331–1343, 2020.

[151] Zhi-Ping Yan, Xu-Feng Luo, Wei-Qiang Liu, Zheng-Guang Wu, Xiao Liang, Kang Liao, Yi Wang, You-Xuan Zheng, Liang Zhou, Jing-Lin Zuo, Yi Pan, and Hongjie Zhang. Configurationally Stable Platinahelicene Enantiomers for Efficient Circularly Polarized Phosphorescent Organic Light-Emitting Diodes. *Chemistry – A European Journal*, 25(22):5672–5676, April 2019.

[152] Li Wan, Jessica Wade, Xingyuan Shi, Shengda Xu, Matthew J Fuchter, and Alasdair J Campbell. Highly Efficient Inverted Circularly Polarized Organic Light-Emitting Diodes. *ACS Applied Materials & Interfaces*, 12(35):39471–39478, September 2020.

[153] Dong-Myung Lee, Jin-Wook Song, Yu-Jin Lee, Chang-Jae Yu, and Jae-Hoon Kim. Control of circularly polarized electroluminescence in induced twist structure of conjugate polymer. *Advanced Materials*, 29(29):1700907, 2017.

[154] Yanhou Geng, Anita Trajkovska, Dimitris Katsis, Jane J Ou, Sean W Culligan, and Shaw H Chen. Synthesis, characterization, and optical properties of monodisperse chiral oligofluorenes. *Journal Of The American Chemical Society*, 124(28):8337–8347, July 2002.

[155] Yanhou Geng, Anita Trajkovska, Sean W Culligan, Jane J Ou, H M Philip Chen, Dimitris Katsis, and Shaw H Chen. Origin of Strong Chiroptical Activities in Films of Nonafluorenes with a Varying Extent of Pendant Chirality. *Journal Of The American Chemical Society*, 125, November 2003.

[156] Jessica Wade, James N Hilfiker, Jochen R Brandt, Letizia Liirò-Peluso, Li Wan, Xingyuan Shi, Francesco Salerno, Seán T J Ryan, Stefan Schöche, Oriol Arteaga, Tamás Jávorfi, Giuliano Siligardi, Cheng Wang, David B Amabilino, Peter H Beton, Alasdair J Campbell, and Matthew J Fuchter. Natural optical activity as the origin of the large chiroptical properties in π-conjugated polymer thin films. *Nature Communications*, 11(1):6137–11, December 2020.

[157] Li Wan, Xingyuan Shi, Jessica Wade, Alasdair J Campbell, and Matthew J Fuchter. Strongly Circularly Polarized Crystalline and β-Phase Emission from Poly(9,9-dioctylfluorene)-Based Deep-Blue Light-Emitting Diodes. *Advanced Optical Materials*, page 2100066.

[158] Frank Neese. The ORCA program system. *Wiley Interdisciplinary Reviews: Computational Molecular Science*, 2(1):73–78, January 2012.

[159] Lasse Kragh Sørensen, Meiyuan Guo, Roland Lindh, and Marcus Lundberg. Applications to metal K pre-edges of transition metal dimers illustrate the approximate origin independence for the intensities in the length representation. *Molecular Physics*, September 2016.

[160] Jamie L Lunkley, Dai Shirotani, Kazuaki Yamanari, Sumio Kaizaki, and Gilles Muller. Extraordinary Circularly Polarized Luminescence Activity Exhibited by Cesium Tetrakis(3-heptafluoro-butylryl-(+)-camphorato) Eu(III) Complexes in EtOH and CHCl3 Solutions. September 2008.

[161] Jessica Wade, James N Hilfiker, Jochen R Brandt, Letizia Liirò-Peluso, Li Wan, Xingyuan Shi, Francesco Salerno, Seán T J Ryan, Stefan Schöche, Oriol Arteaga, Tamás Jávorfi, Giuliano Siligardi, Cheng Wang, David B Amabilino, Peter H Beton, Alasdair J Campbell, and Matthew J Fuchter. Natural optical activity as the origin of the large chiroptical properties in π-conjugated polymer thin films. *Nature Communications*, 11:6111–6137, December 2020.

[162] Xingyuan Shi, Vojtech Nádaždy, Aleksandr Perevedentsev, Jarvist M Frost, Xuhua Wang, Elizabeth von Hauff, Roderick CI MacKenzie, Jenny Nelson, et al. Relating chain conformation to the density of states and charge transport in conjugated polymers: The role of the β-phase in poly (9, 9-dioctylfluorene). *Physical Review X*, 9(2):021038, 2019.

[163] Jake L Greenfield, Emrys W Evans, Daniele Di Nuzzo, Marco Di Antonio, Richard H Friend, and Jonathan R Nitschke. Unraveling Mechanisms of Chiral Induction in Double-Helical Metallopolymers. *Journal Of The American Chemical Society*, 140(32):10344–10353, August 2018.

[164] Mark A Stevens, Carlos Silva, David M Russell, and Richard H Friend. Exciton dissociation mechanisms in the polymeric semiconductors poly(9,9-dioctylfluorene) and poly(9,9-dioctylfluorene-co-benzothiadiazole). *Phys. Rev. B*, 63(16):165213, April 2001.

[165] N Harada, SML Chen, K Nakanishi Journal of the American, and 1975. Quantitative definition of exciton chirality and the distant effect in the exciton chirality method. *ACS Publications*.

[166] Torsten Bruhn, Gennaro Pescitelli, Sandro Jurinovich, Anu Schaumlöffel, Franziska Witterauf, Johannes Ahrens, Martin Bröring, and Gerhard Bringmann. Axially Chiral BODIPY DYEmers: An Apparent Exception to the Exciton Chirality Rule. *Angewandte Chemie International Edition*, 53(52):14592–14595, December 2014.

[167] On the origin of optical activity in polythiophenes. *Journal of Molecular Structure*, 521(1-3):285–301, March 2000.

[168] Gianluigi Albano, Gennaro Pescitelli, and Lorenzo Di Bari. Chiroptical Properties in Thin Films of π-Conjugated Systems. *Chemical Reviews*, September 2020.

[169] William Barford and Max Marcus. Perspective: Optical spectroscopy in π-conjugated polymers and how it can be used to determine multiscale polymer structures. *The Journal of Chemical Physics*, 146(13):130902, April 2017.